SAPIENZA
UNIVERSITÀ DI ROMA

FACOLTÀ DI INGEGNERIA CIVILE E INDUSTRIALE
Dottorato in Ingegneria Ambientale e Idraulica – Ciclo XXIX

Two-dimensional and Three-dimensional Non Hydrostatic Models for Fully Non-linear and Dispersive Hydrodynamic Processes

Supervisor:
Prof. Ing. Francesco Gallerano

Ph.D. Candidate:
Ing. Francesco Lasaponara

Two-dimensional and Three-dimensional Non Hydrostatic Models for Fully Non-linear and Dispersive Hydrodynamic Processes

Ph.D. Candidate Ing. Francesco Lasaponara

October 11, 2016

Contents

1. A new Fully Non-linear Boussinesq Model for simulation Hydrodynamics phenomena in complex coastal regions 10

1.1. Introduction on 2D Boussinesq Model 10

1.2. List of Symbols 16

1.3. A new contravariant form of FNBE 17

1.3.1. The Christoffel Symbols in the momentum equation 22

1.3.2. The integral form of FNBE 24

1.4. Numerical Scheme 27

1.4.1. Genuinely 2D reconstructions 31

1.4.2. Wetting drying scheme 34

1.5. Metric Identities 36

1.6. Results 41

1.6.1. The dam-break problem on a dry bed 41

1.6.2. Solitary wave run-up on a conical island 43

1.6.3. Longshore current simulation 47

1.6.4. Nearshore currents induced by submerged breakwaters 52

1.6.5. C-Property Test 57

1.6.6. Conservation wave form on a flat bed 62

1.6.7. Wave train propagation on a varying depth 66

1.6.8. Simulation of wave train propagation on a highly distorted grid 70

2. A new 3D FV Non-hydrostatic Shock Capturing model for free surface flow 74

2.1. Introduction on 3D model 74

2.2. List of Symbols 77

2.3. An integral form of 3D sigma-coordinate equations 78

2.4. Numerical Scheme 84

2.5. Results 87

2.5.1. Wave deformation over a submerged bar 87

2.5.2. Wave deformation by an elliptic shoal. 89

2.5.3. Solitary wave on a slope beach (Synolakis 1987). 92

2.5.4. Vortices formation dues to wave-structure interaction. 94

2.5.5. Three-dimensional simulation of flow-structure interaction. 100

3. Conclusions 103

4. References 104

Executive Summary

The following thesis collects the work done by the candidate Francesco Lasaponara during the Phd course of Civil and Environmental Engineering at "La Sapienza" University of Rome. The main goal of these studies is the implementation of the mathematical models in order to simulate hydrodynamic phenomena in coastal regions and other specific environmental situations.

During the last decades, interest has aroused on issues concerning environmental hydraulics, respectively coastal and river hydraulics, due to the impact they have on environment and societies. Coasts are crucial for a community's environmental, economic and landscaping patrimony, unfortunately recently they are interested by the shoreline recession, silting of maritime infrastructures or the protection shoreline infrastructures' malfunctioning phenomena.

Most of these problems are due to current existing infrastructures' or defenses coastal structures' erroneous design. In particular, the calculus models used for environmental impact and structures-environmental interactions assessment were obsolete or even inexistent. These mathematical models used in the past do not take into account some dynamic processes that in long term might become not negligible nor devastating. Only in the recent years, when the computational power increased and a common sensibility to these problems increased, the above mentioned calculus models have given way to more accurate and advanced modeling. For these reasons, the main goal of this work is to propose original mathematical models able to simulate most of hydrodynamic phenomena that occur in coastal regions. These models may be considered an useful tool in the hydraulic and environmental designing fields.

The thesis is divided in two main parts. In the first part is presented a model based on a numerical integration of a new conservative form of the Fully Non-linear Boussinesq Equations (FNBE) in a contravariant formulation. As known coastal regions are characterized by a very complex morphology: presence of anthropic structures, river mouth or shoreline with articulated geometry. The use of orthogonal grid, as Cartesian coordinate, requests a huge number of calculus points that may be prohibitive. To solve this issue, a well known strategy is to integrate the motion equations on generalized curvilinear boundary conforming grid.

In order to apply this strategy is necessary to write governing equations in contravariant formulation. The Boussinesq models are part of the so-called group "depth averaged models", these models are particularly effective for large-scale wave motions, longshore currents and hydrodynamic simulations. These models are a good compromise (in terms of computational costs

and accuracy of solution) between traditional methods and more advanced three-dimensional models. The depth averaged models are able to simulate most of the wave transformation phenomena (refraction, diffraction, shoaling and breaking), and longshore currents. Nevertheless these models are not able to take into account the depth distribution of hydrodynamic quantities.

In the second part it is presented an original fully non-hydrostatic three-dimensional model based on the numerical integration of Navier-Stokes Equations in time dependent coordinate system. The use of time dependent coordinate system allows to assign, without any approximations, bottom and free surface kinematic conditions and zero pressure condition at the upper boundary of the domain. Unlike the depth averaged model, this model is able to simulate the three-dimensionality of hydrodynamic phenomena related to the wave motion of unsteady flows.

The proposed model belongs to the group of the so-called “free surface fully non-hydrostatic three-dimensional models”. These models are often used to analyze local phenomena, to evaluate flow-structure interaction, for sediment transport analysis and to study turbulences phenomena related with them. In general the free surface fully non-hydrostatic three-dimensional models are used for all engineering problems for which is necessary to know the vertical distribution of hydrodynamic quantities.

Most of the arguments presented in this thesis have been published in the following paper: “A new numerical model for simulations of wave transformation breaking and longshore currents in complex coastal regions” on “International Journal for numerical methods in fluids” (Gallerano, Cannata and Lasaponara - 2016).

The work is organized as it follows:

1) In chapter one there is an Overview to explain the subject and the main objectives of the thesis.
2) In chapter two there is an introduction of a new contravariant integral form of the Fully Non-Linear Boussinesq Equations. It also describes the numerical algorithm to solve governing equations and calibration tests.
3) In Chapter three an introduction of a new model based on the numerical integration of the Navier-Stokes Equations on time dependent coordinate system is presented. It follows, as in the previous chapter, the explanation of the numerical procedure to solve governing equations and calibration tests.
4) In the last chapter are exposed the conclusion of the work.

1. A new Fully Non-linear Boussinesq Model for simulation Hydrodynamics phenomena in complex coastal regions

In this chapter is described a model based on a new contravariant integral form of the Fully Non-linear Boussinesq Equations (FNBE) in order to simulate wave transformation phenomena, wave breaking and nearshore currents in computational domains representing the complex morphology of real coastal regions. The above-mentioned contravariant integral form, in which Christoffel symbols are absent, is characterized by the fact that the continuity equation does not include any dispersive term. A procedure developed in order to correct errors related to the difficulties of numerically satisfying the metric identities in the numerical integration of FNBE on generalized boundary-conforming grids is presented. The Boussinesq equation system is numerically solved by a hybrid finite volume-finite difference scheme. The proposed high-order upwind Weighted Essentially Non Oscillatory (WENO) finite volume scheme involves an exact Riemann solver and is based on a genuinely two dimensional reconstruction procedure which uses a convex combination of biquadratic polynomials. The wave breaking is represented by discontinuities of the weak solution of the integral form of the Non-linear Shallow Water Equations (NSWE). On the basis of the shock-capturing high order WENO scheme a new procedure, for the computation of the structure of the solution of a Riemann problem associated with a wet/dry front, is proposed in order to simulate the run up hydrodynamics in swash zone. The results obtained are compared with experimental measures, analytical solutions or alternative numerical solutions.

1.1. Introduction on 2D Boussinesq Model

The modeling of surface wave transformation, wave breaking and nearshore currents is of fundamental importance for the simulation of hydrodynamic phenomena which occur in coastal regions. Most of these phenomena can be represented by two dimensional Boussinesq equations.
Classic forms of the Boussinesq equations (Peregrine [1967]) include the lowest order of both frequency dispersion and non-linearities and are able to adequately represent wave phenomena only in a range of values of the water depth, h_0, to deep water wavelength, L_0, ratio up to 0.2. In order to overcome such restriction different formulations of Boussinesq equations have been proposed: Madsen and Sørensen [1992] improved the dispersion properties of the Standard Boussinesq equations in the deep water zone by introducing an additional third order term, which can be considered as a slight modification of the Padé approximant of the full dispersive relation, in the

depth integrated momentum equation.

Nwogu [1993] derived an alternative form of the extended Boussinesq equations, in which the dependent variable was the velocities at an arbitrary distance from the still water level, and improved the linear dispersion properties of the standard Boussinesq equation retaining terms of order $O(\varepsilon,\mu^2)$, where $\varepsilon=a_0/h_0$ and $\mu=h_0/L_0$ are non-dimensional parameters related to the order of magnitude of non-linearities and frequency dispersion and a_0 is the deep water wave amplitude.

Wei et al. [1995] followed the Nwogu [1993] approach and derived a fully non-linear extension of the Boussinesq equations by retaining terms of order $O(\mu^2,\varepsilon^3\mu^2)$ and consequently improved the accuracy of the model just seaward of the surf zone where the wave height to water depth ratio is essentially equal to 1.

Chen [2003] used a model based on the fully non-linear extended Boussinesq equations proposed by Wei et al. [1995] and improved the representation of wave induced nearshore circulations by retaining second order terms related to the vertical vorticity in the Boussinesq equations.

The simulation of wave propagation from deep water regions up to the coastline, including the surf zone, has three main difficulties.

The first one is about the contradiction between the high order terms in the Boussinesq equations and the low order of the numerical schemes. The second difficulty is related to the way in which the wave breaking is simulated. The third difficulty is related to the form of the equations and, in particular, to the presence of the dispersive term in the continuity equation and to the scheme by which this term is discretized.

As mentioned above, the first difficulty that arises in the integration of the FNBE is that the truncation errors of low order numerical schemes significantly affect the accuracy of the solution. As highlighted by Erduran [2005], this is because the truncation errors of the low order numerical approximations are of the same form and of the same order of magnitude as the dispersive terms in the Boussinesq equations.

Hence these errors lead to the prediction of non-physical dispersion. In other words the truncation errors related to low order schemes, applied to Boussinesq equations, prevent dispersive terms in the same equations to guarantee wave form conservation in deep water and wave form evolution on non-uniform bottoms just seaward of the surf zone. In order to overcome these problems and obtain accurate solutions, a careful treatment of truncation errors is necessary. Consequently the simulation of wave propagation from deep water regions just seaward the surf zone needs a high order numerical scheme for the integration of the above mentioned equation.

As already said the second difficulty is related to the way in which the wave breaking is simulated. Boussinesq Equations cannot represent the wave breaking phenomenon in shallow water. As

explained by Roeber et al [2012] the parabolic non-hydrostatic part of the Boussinesq equations may become unstable under discontinuous flow conditions. In order to take into account the energy dissipation produced by the wave breaking in the surf zone, many authors treat Boussinesq equations with different techniques. One of these techniques is based on the introduction of a dissipative term, like an eddy viscosity type term, in the momentum equation (Karambas and Koutitas [1992], Kennedy et al. [2000]); different methods are based on the "surface roller" concept introduced by Svendsen [1996].

As highlighted by Tonelli and Petti [2012], the wave breaking models based on the above mentioned techniques require the estimation of empirical parameters that should be calibrated. Moreover Shi et al [2012] underline that the introduction of an eddy viscosity model for surf zone can be a source of spurious oscillations in the numerical solutions. An alternative procedure for the wave breaking simulation starts from the consideration that the wave breaking can be represented by the discontinuity of the weak solution of the integral form of the NSWE. In the surf zone the integral forms of the Boussinesq equations reduce themselves to the integral form of the NSWE by dynamically switching off dispersive terms.

The integral form of the NSWE, expressed in terms of conserved variables, guarantees that high order shock capturing numerical schemes converge to correct weak solutions and then is able to directly simulate wave breaking and the energy dissipation associated with it (Toro [2001]). In fact, in recent literature, integral forms (Gallerano et al [2014]) or differential conservative forms of the Boussinesq equations expressed in terms of conserved variables (Erduran [2005], Tonelli & Petti [2009], Roeber et al [2010], Roeber and Cheung [2012], Shi et al [2012]) are proposed.

In this way it is possible to apply the same shock capturing numerical scheme for the numerical integration of the NSWE even for the integration of the FNBE and then it is possible to simulate wave propagation from deep water regions up to the coastline, including the surf zone by using a single numerical scheme.

As mentioned above the third difficulty that arises in the integration of the Boussinesq equations is related to the form of the equations and, in particular, to the presence of the dispersive term in the continuity equation and to the modality of the discretization of this term consistently with finite difference schemes used in the hybrid scheme (finite volume-finite difference).

The presence of a dispersive term in the continuity equation is due to the way in which Nwogu [1993], Wei et al [1995], Chen et al [2003] and Chen [2006] formulated extended versions of Boussinesq equations. In these models, the improvement of the dispersive properties of the standard forms of the equations is due to the adoption of velocity at an arbitrary distance from the still water level, as dependent variable, instead of the depth averaged velocity. Nevertheless, this choice

entailed the appearance of the dispersive term in the continuity equation.

Also in the differential conservative form proposed by Roeber et al [2010] and Roeber and Cheung [2012], as well as in the contravariant integral form proposed by Gallerano et al [2014], there is a dispersive term in the continuity equation.

In these works the dispersive term that appears in the continuity equations is discretized with a second order cell-centered finite difference scheme consistently with the finite difference scheme of the hybrid scheme. The discretization of this dispersive term by a second order cell-centered finite difference scheme introduces truncation errors into the solution that can reduce the global accuracy of the numerical scheme and induce oscillations in the numerical solution.

From the above mentioned consideration it can be deduced that the difficulty in the simulation of wave propagation from deep water regions up to the coastline (without the need to include in the equations any term designed to represent wave breaking energy dissipation) can be overcome by the integration of the FNBE (which in the surf zone reduce themselves to the NSWE by switching off dispersive terms) that does not contain any dispersive term in the continuity equation, by a high order shock capturing scheme.

In general, coastal engineering issues are related to nearshore currents occurring in real situations which can be morphologically complex. Consequently the simulation of wave propagation in coastal areas, where slightly sloping and regular sea beds alternate with steep irregular bottoms and the coastlines can be characterized by articulated shapes and be interrupted by the presence of anthropogenic structures and/or river mouths is worthy of engineering interest.

In order to simulate hydrodynamic phenomena over computational domains characterized by a complex boundary it is possible integrate the motion equations on a generalized curvilinear boundary conforming grid. By using curvilinear boundary conforming grids motion equations can be written in contravariant formulation (Luo and Bewley [2004], Rossmanith et al. [2004], Wesseling et al. [1999], Zijlema et al. [1995], Segal et al. [1992] and Gallerano et al [2012]).

The numerical integration of integral forms or differential conservative forms of Boussinesq equations, on generalized curvilinear grids, can produce a new class of numerical errors: these errors can corrupt the ability of the numerical solutions of the Boussinesq equations to represent the wave form evolution.

The first cause of numerical errors is due to the presence of the Christoffel symbols in the contravariant form of Boussinesq equations. The Christoffel symbols are extra source terms which do not allow the writing of convective terms in divergence form and local total depth terms in a gradient form, i.e. in conservative form.

In the case of a numerical integration of FNBE on high distorted grids, the errors linked to the

discretization of the Christoffel symbols can be of the same order of magnitude as the dispersive terms and can prevent the conservation of the wave form from propagating in deep water and on flat bottoms. Furthermore, in wave breaking case, errors produced by discretization of the Christoffel symbols can prevent the numerical scheme from converging to the weak solution.

A second cause of numerical errors, in numerical integration of Boussinesq equations in contravariant formulation, is related to the difficulty of numerically fulfilling the metric identities. A well-known geometric identity (Vinokur [1989]) is given by the condition that a cell is closed. In a curvilinear system of reference the aforementioned condition becomes the metric identity. In general, if numerical approximations of the metric coefficients do not exactly satisfy the above mentioned identity, in the numerical integration of motion equations, numerical approximations of derivatives of uniform physical quantities do not vanish, free stream conditions are not preserved and spurious oscillations can appear in the solution which can drastically reduce the accuracy of high order schemes (Visbal and Gaitonde [2002], Yang et al [1994]). In the numerical integration of Boussinesq equations in contravariant formulation, the errors linked to the difficulty of numerically fulfilling the metric identities can be of the same order of magnitude as the dispersive terms and can consequently compromise the numerical scheme capacity to preserve the wave form which propagates on a flat bottom.

The third cause of numerical errors is related to the numerical technique for the reconstruction of dependent variables of the system at the interface of computational cells. Jiang and Shu [1996] consider that high order WENO schemes are fairly suitable for the numerical simulation of problems with complex, non-trivial behavior of solutions in smooth regions. In most of such WENO schemes presented in literature, the reconstruction of dependent variables at the interface of computational cells is performed through two consecutive one-dimensional procedures, each relative to one coordinate direction (dimension-by-dimension reconstruction).

In the first step of this reconstruction procedure, which is performed along the general coordinate direction ξ^1, a first level of deconvolution is accomplished, which consists in passing from averaged values on calculation cells to averaged values over direction ξ^2. In such a step approximation errors of n+1 order are introduced (in which n-1 is the order of the polynomial used). The values obtained from the first step are used as starting values in a second one-dimensional reconstruction procedure, which is accomplished along the ξ^2direction. With this second reconstruction (where by variable point values at the cell interface are obtained) additional truncation errors are introduced in the numerical solution, that can be amplified by the presence of errors introduced in the first reconstruction step.

Furthermore, in the numerical integration of Boussinesq equations on generalized curvilinear

boundary conforming grids, the amplification of truncation errors produced by the use of two consecutive one-dimensional reconstructions can further decrease the accuracy of the numerical scheme and can compromise the dispersive properties of the Boussinesq equations.

In this thesis a model based on a new integral form of the Fully Non-linear Boussinesq Equations in contravariant formulation, in which terms of order $O(\mu^2,\varepsilon^3\mu^2)$ and second order vertical vorticity terms are included, is presented. The proposed Boussinesq equations are cast in a contravariant integral form in which Christoffel symbols are absent.

The Boussinesq equation system is numerically solved by a hybrid finite volume-finite difference scheme: the convective terms and the terms related to the gradient of the square of the total local water depth are discretized by an original high-order upwind WENO shock-capturing finite volume scheme, based on an exact Riemann solver; the dispersive terms and the terms related to the approximation to the second order of the vertical vorticity are discretized by a cell-centered finite difference scheme. The integral form of the continuity equation described in this thesis does not contain dispersive terms and is entirely discretized by the above-mentioned shock capturing finite volume scheme. In this way the errors due to the low order discretization of such dispersive term are not introduced into the solution.

A procedure is developed in order to correct errors related to the difficulties of numerically satisfying the metric identities in the numerical integration of the FNBE on generalized boundary-conforming grids. The proposed high-order upwind WENO finite volume scheme is based on a genuinely two dimensional reconstruction procedure which uses a convex combination of biquadratic polynomials in (ξ^1, ξ^2) (i.e. a convex combination of quadratic polynomial functions of the two variables ξ^1 and ξ^2). The wave breaking is represented by discontinuities of the weak solution of the integral form of the NSWE. As a consequence no additional term to take into account the wave breaking energy is added in the equations. Furthermore an original procedure for the treatment of the wet/dry front is presented.

1.2. List of Symbols

$\vec{b}$: generic vector

b^l :contravariant component of the vector $\vec{b}$

b_l : covariant component of the vector $\vec{b}$

$b^l{}_{,m}$: covariant derivative of b^l

Γ^l_{mk} : Christoffel symbol

$T^{lm}_{,m}$: covariant derivative of generic tensor T^{lm}

σ : arbitrary distance from the still water level

∇ : two-dimensional differential operator

$\vec{u}$: horizontal velocity at σ

η : local surface displacement

h : local still water depth

g^{lm} : metric tensor

$\vec{V}$ and $\vec{T}$: dispersive terms

$\vec{W}$: second order vertical vorticity

V^l, T^l and W^l : Contravariant component of $\vec{V}$, $\vec{T}$ and $\vec{W}$

1.3. A new contravariant form of FNBE

Let H=h+η be the total local water depth, where h is the local still water depth and η is the local surface displacement. Using a Taylor expansion of the velocity about an arbitrary distance from the still water surface, σ, and assuming zero horizontal vorticity, as proposed by Nwogu [1993], Wei et al. [1995], Chen et al. [2003], Chen [2006], the vertical distribution of the horizontal velocity $\vec{U}(z)$ can be written as

$$\vec{U}(z) = \vec{u} + \vec{v}(z) \tag{1}$$

Where $\vec{u}$ is the horizontal velocity at an arbitrary distance from the still water level z = σ, and $\vec{v}(z)$ is

$$\vec{v}(z) = (\sigma - z)\nabla(\nabla \cdot (h\vec{u})) + (\frac{\sigma\hat{}2}{2} - \frac{z\hat{}2}{2})\nabla(\nabla \cdot (\vec{u})) \tag{2}$$

(the "^" symbol indicates the operation of power raising) that represents the second order term in power series expansion of the velocity vector about σ, in which ∇ is the two-dimensional differential operator defined as $\nabla = \left(\frac{\partial}{\partial x}, \frac{\partial}{\partial y}\right)$ in a Cartesian reference system. Let $\vec{\bar{v}}$ be the depth averaged value of $\vec{v}(z)$, obtained by retaining terms of order $O(\mu^2, \varepsilon^2\mu^2)$,which is

$$\vec{\bar{v}} = \frac{1}{H}\int_{-h}^{\eta} \vec{v}(z)\, dz = \left(\frac{\sigma\hat{}2}{2} - \frac{1}{6}(h\hat{}2 - h\eta + \eta\hat{}2)\right)\nabla(\nabla \cdot (\vec{u})) + (\sigma + \frac{1}{2}(h - \eta))\nabla(\nabla \cdot (h\vec{u})) \tag{3}$$

Let $x^l = x^l(\xi^1, \xi^2)$ (with *l=1,2)* be the transformation from the Cartesian coordinate system $\vec{x}$ to the curvilinear coordinate system $\vec{\xi}$ (henceforth the superscript indicate components and not powers). Let $\vec{g}_{(l)} = \partial\,\vec{x}/\partial\,\xi^l$ be the covariant base vector and $\vec{g}^{(l)} = \partial\,\xi^l/\partial\,\vec{x}$ be the contravariant base vector. The metric tensor and its inverse are given respectively by $g_{lm} = \vec{g}_{(l)} \cdot \vec{g}_{(m)}$ and $g^{lm} = \vec{g}^{(l)} \cdot \vec{g}^{(m)}$. The Jacobian of the transformation is $\sqrt{g} = \sqrt{det(g_{lm})}$.

Let the transformation relations of the generic vector $\vec{b}$ from the Cartesian coordinate system to its covariant and contravariant components (b_l, b^l) in the curvilinear coordinate system:

$$b^l = \vec{g}^{(l)} \cdot \vec{b}\,; \quad b_l = \vec{g}_{(l)} \cdot \vec{b}\,; \quad \vec{b} = b^l \vec{g}_{(l)}\,; \quad \vec{b} = b_l \vec{g}^{(l)} \tag{4}$$

the covariant derivate and Christoffel symbols are given by:

$$b^l{}_{,m} = \partial\, b^l / \partial\, \xi^m + \Gamma^l_{mk} b^k \tag{5}$$

$$\Gamma^l_{mk} = \vec{g}^{(l)} \cdot \partial\, \vec{g}_{(k)} / \partial\, \xi^m \tag{6}$$

and the covariant derivative of second order tensor T^{lm} :

$$T^{lm}_{,m} = \frac{1}{\sqrt{g}} \frac{\partial T^{lm} \sqrt{g}}{\partial \xi^m} + T^{nm} \Gamma^l_{nm} \tag{7}$$

Hereinafter the comma followed by a subscript position index indicates the derivative covariant operation.

In the curvilinear coordinate system, the Boussinesq equations expressed in contravariant formulation can be written as

$$\frac{\partial \eta}{\partial t} + (H u^l)_{,l} = -(H \bar{v}^l)_{,l} \tag{8}$$

$$\frac{\partial u^l}{\partial t} + u^l_{,m} u^m = -G g^{lm} \eta_{,m} - V^l - T^l - W^l - R^l \tag{9}$$

in which u^l and $\bar{v}^l$ are the contravariant components of the vectors $\vec{u}$ and $\vec{\bar{v}}$, G is acceleration due to gravity, R^l, V^l, T^l, W^l are, respectively, the contravariant components of the vectors $\vec{R}$, $\vec{V}$, $\vec{T}$, and $\vec{W}$. $\vec{R}$ represents the bottom resistance term, $\vec{V}$ and $\vec{T}$ represent the dispersive terms obtained by retaining terms of order $O(\mu^2, \varepsilon^3 \mu^2)$ (Wei et al. [1995]) and $\vec{W}$ represents the term related to the second order approximation of the vertical vorticity, according to Chen [2003]. The expressions of these vectors and their contravariant components are given by:

$$\vec{V} = \frac{1}{2} \sigma^{\wedge 2} \nabla \left[\nabla \cdot \frac{\partial \vec{u}}{\partial t} \right] + \sigma \nabla \left\{ \nabla \cdot \left[h \frac{\partial \vec{u}}{\partial t} \right] \right\} - \nabla \left\{ \frac{1}{2} \eta^{\wedge 2} \nabla \cdot \left(\frac{\partial \vec{u}}{\partial t} \right) + \eta \nabla \cdot \left[h \frac{\partial \vec{u}}{\partial t} \right] \right\} \tag{10}$$

$$\vec{T} = \nabla \left\{ (\sigma - \eta)(\vec{u} \cdot \nabla)[\nabla \cdot (h\vec{u})] + \frac{1}{2} (\sigma^{\wedge 2} - \eta^{\wedge 2})(\vec{u} \cdot \nabla)[\nabla \cdot \vec{u}] \right\} + \frac{1}{2} \nabla \{ [\nabla \cdot (h\vec{u}) + \eta \nabla \cdot \vec{u}]^{\wedge 2} \} \tag{11}$$

$$\overrightarrow{W} = \hat{\imath}\left\{-\bar{v}_y\left[\frac{\partial u_y}{\partial x} - \frac{\partial u_x}{\partial y}\right] + u_y\left[\frac{\partial \bar{v}_x}{\partial x} - \frac{\partial \bar{v}_y}{\partial y}\right]\right\} + \hat{\jmath}\left\{\bar{v}_x\left[\frac{\partial u_y}{\partial x} - \frac{\partial u_x}{\partial y}\right] - u_x\left[\frac{\partial \bar{v}_x}{\partial x} - \frac{\partial \bar{v}_y}{\partial y}\right]\right\} \quad (12)$$

$$V^l = \frac{\sigma\hat{}2}{2} g^{lm}\left[\left(\frac{\partial u^k}{\partial t}\right)_{,k}\right]_{,m} + \sigma g^{lm}\left[\left(h\frac{\partial u^k}{\partial t}\right)_{,k}\right]_{,m} - g^{lm}\left[\frac{1}{2}\eta\hat{}2\left(\frac{\partial u^k}{\partial t}\right)_{,k} + \eta\left(h\frac{\partial u^k}{\partial t}\right)_{,k}\right]_{,m} \quad (13)$$

$$T^l = g^{lm}\left\{(\sigma-\eta)u^i\left([hu^k]_{,k}\right)_{,i} + \frac{1}{2}(\sigma\hat{}2 - \eta\hat{}2)u^i\left(u^k_{,k}\right)_{,i}\right\}_{,m} + \frac{1}{2}g^{lm}\left\{\left[(hu^k)_{,k} + \eta u^k_{,k}\right]\hat{}2\right\}_{,m} \quad (14)$$

$$W^l = \left(\varepsilon^{mi} g_{ip} u^p_{,m}\right)\varepsilon^{jl}\bar{v}_j + \left(\varepsilon^{mi} g_{ip}\bar{v}^p_{,m}\right)\varepsilon^{jl}u_j \quad (15)$$

In which:

$$\varepsilon^{mi} = \begin{cases} \frac{1}{\sqrt{g}} if(m,i)\ is\ a\ even\ permutation\ of\ (1,2) \\ -\frac{1}{\sqrt{g}}\ if\ (m,i)\ is\ a\ odd\ permutation\ of\ (1,2) \\ 0\ if\ the\ indexes\ are\ equal \end{cases}$$

In order to apply a shock capturing scheme to the Boussinesq type equations, the convective terms must be expressed in conservative form, i.e. in divergence form. In Gallerano et al [2014] the system evolution variables were the conserved variables H e Hu^l. The choice of these conserved variables implied the presence of a source term in the mass conservation equation (right hand side of Equation (11) in Gallerano et al. [2014]). The source term present in this equation was discretized with a second order accurate centred finite difference scheme. In this work we choose, as conserved variables, the total local depth H and the contravariant quantity

$$M^l = H(u^l + \bar{v}^l) \quad (16)$$

in which$(u^l + \bar{v}^l)$ represents the depth averaged horizontal velocity. With this choice, considering that the bottom depth does not vary over time, continuity Equation (16) can be written as

$$\frac{\partial \mathrm{H}}{\partial t} + M^l_{,l} = 0 \quad (17)$$

As follows from Equation (17), the choice of the conserved variable M^l expressed by Equation (16) makes it possible to write the continuity equation without any source term, but only with a flux term, expressed by M^l. This result implies that the continuity equation can be solved entirely by a high order shock capturing finite volume scheme.

In the momentum balance equation, local acceleration and convective terms $\frac{\partial u^l}{\partial t} + u^l_{,m}u^m$ (with m=1,2) are expressed in conservative form through the relation

$$\frac{\partial M^l}{\partial t} + \left(\frac{M^l M^m}{H}\right)_{,m} = H\frac{\partial(u^l+\bar{v}^{\mathrm{l}})}{\partial t} + \left(u^l + \bar{v}^{\mathrm{l}}\right)\frac{\partial \mathrm{H}}{\partial t} + \left[H\left(u^l + \bar{v}^{\mathrm{l}}\right)\left(u^m + \bar{v}^{\mathrm{m}}\right)\right]_{,m} \tag{18}$$

Using the following vector identity (Warsi [1992]) for the third term on the right hand side of Equation (18)

$$\left(a^l b^m\right)_{,m} = a^l_{,m}b^m + a^l b^m_{,m} \tag{19}$$

in which $a^l = \left(u^l + \bar{v}^{\mathrm{l}}\right)$ and $b^l = H\left(u^l + \bar{v}^{\mathrm{l}}\right)$, Equation (18) can be rewritten as

$$\begin{aligned}&\frac{\partial M^l}{\partial t} + \left(\frac{M^l M^m}{H}\right)_{,m}\\ &= \left(u^l + \bar{v}^l\right)\left\{\frac{\partial H}{\partial t} + \left[H\left(u^m + \bar{v}^m\right)\right]_{,m}\right\} + H\left\{\frac{\partial u^l}{\partial t} + u^l_{,m}u^m\right\}\\ &+ H\left(\frac{\partial \bar{v}^l}{\partial t} + \bar{v}^l_{,m}u^m + u^l_{,m}\bar{v}^m + \bar{v}^l_{,m}\bar{v}^m\right)\end{aligned} \tag{20}$$

The first term on the right hand side of Equation (20) is null for the continuity Equation (17), while the terms in the second curly brackets can be replaced by the right hand side of Equation (9). In this way the momentum balance equation can be written in the form

$$\begin{aligned}&\frac{\partial M^l}{\partial t} + \left(\frac{M^l M^m}{H}\right)_{,\mathrm{m}}\\ &= -GHg^{lm}\eta_{,m} - H\left(V^l + T^l + W^l + R^l\right) + H\left(\frac{\partial \bar{v}^l}{\partial t} + \bar{v}^l_{,m}u^m + u^l_{,m}\bar{v}^m + \bar{v}^l_{,m}\bar{v}^m\right)\end{aligned} \tag{21}$$

Motion equations admit stationary solutions in which the source terms are perfectly balanced by the flux terms. A numerical scheme is said to be well-balanced and satisfies the C-Property if it preserves the steady state solutions exactly. The surface gradient term could be split into a source term that is related to the bed slope and a term related to the gradient of the square of the local total depth, in order to include this term into the flux term and to perform a shock capturing upwind scheme.

In particular, in the absence of motion, the numerical discretization of the source term relative to the bottom slope should perfectly balance the numerical discretization of the term related to the gradient of the square of the total local depth. Shi et al [2012] point out that the above decomposition induces a numerical imbalance problem and does not allow the numerical scheme to satisfy the C-Property for non-uniform bed.

In order to obtain a "well-balanced" numerical scheme, the surface gradient term is decomposed as

$$Gg^{lm}H\eta_{,m} = \left(Gg^{lm}\frac{H\hat{}2}{2}\right)_{,m} - \left[G(\eta-\eta_c)(g^{lm}h)_{,m} + G\eta_c(g^{lm}h)_{,m} + G\left(g^{lm}\frac{h\hat{}2}{2}\right)_{,m}\right] \quad (22)$$

where η_c is an arbitrary constant value. The term V^l, present on the right hand side of Equation (21) can be decomposed as

$$V^l = \frac{\partial V'^l}{\partial t} + V''^l \quad (23)$$

in which V'^l and V''^l are:

$$V'^l = \frac{1}{2}\sigma\hat{}2\,g^{lm}\left[(u^k)_{,k}\right]_{,m} + \sigma g^{lm}\left[(hu^k)_{,k}\right]_{,m} - g^{lm}\left[\frac{1}{2}\eta\hat{}2(u^k)_{,k} + \eta(hu^k)_{,k}\right]_{,m} \quad (24)$$

$$V''^l = g^{lm}\left[\frac{\partial}{\partial t}\left(\frac{\eta\hat{}2}{2}\right)(u^k)_{,k}\right]_{,m} + g^{lm}\left[\frac{\partial\eta}{\partial t}(hu^k)_{,k}\right]_{,m} \quad (25)$$

the term (25) can be written in the form:

$$V''^l = g^{lm}\left[\eta\frac{\partial\eta}{\partial t}\right]_{,m}(u^k)_{,k} + g^{lm}\eta\frac{\partial\eta}{\partial t}\left[(u^k)_{,k}\right]_{,m} + g^{lm}\left[\frac{\partial\eta}{\partial t}\right]_{,m}(hu^k)_{,k} + g^{lm}\frac{\partial\eta}{\partial t}\left[(hu^k)_{,k}\right]_{,m} \quad (26)$$

Substituting Equations (22) and (23) into Equation (21), a new form of the FNBE expressed in contravariant formulation is obtained

$$\frac{\partial D^l}{\partial t} + \left(\frac{M^l M^m}{H} + G g^{lm} \frac{H^{\wedge 2}}{2}\right)_{,\mathrm{m}} - \left[G(\eta - \eta_c)(g^{lm}h)_{,m} + G\eta_c (g^{lm}h)_{,m} + G\left(g^{lm}\frac{h^{\wedge 2}}{2}\right)_{,\mathrm{m}}\right]$$
$$= \frac{\partial H}{\partial t}\left(V'^{l} - \bar{v}^l\right) - H\left(V'^{,l} + T^l + W^l + R^l\right) + H\left(\bar{v}^l_{,m} u^m + u^l_{,m}\bar{v}^m + \bar{v}^l_{,m}\bar{v}^m\right) \tag{27}$$

Where D^l represents an auxiliary variable defined by

$$D^l = H(u^l + V'^l) \tag{28}$$

The term $\frac{\partial \mathrm{H}}{\partial \mathrm{t}}$,on the right hand side of Equation (27), and the term $\frac{\partial \eta}{\partial \mathrm{t}}$,on the right hand side of Equation (26), can be explicitly calculated using the continuity Equation (17), as proposed in Roebber et al [2010].

Equations (17) and (27) represent a new system of FNBE in contravariant formulation in which H and D^l are the dependent variables. The first parentheses is on the left hand side of Equation (27) represents the sum of the convective term and the term relative to the square of the total local depth; the terms in square brackets on the left hand side of Equation (27) are related to the bottom slope; the first and second parentheses on the right hand side of Equation (27) represent dispersive terms, the term linked to the approximation to the second order of the vertical vorticity and the bottom resistance, while the third parentheses is on the right hand side of Equation (27) represents the source terms related to the gradient of the vectors whose contravariant components are u^l and $\bar{v}^l$.

The covariant derivatives in the momentum balance Equation (27) determine the onset of the Christoffel symbols, as expressed by the relations (5-6-7). These symbols represent additional source terms that do not allow the writing of the convective term sin divergence form and the term related to the square of the total local depth in a gradient form, i.e. in conservative form.

1.3.1. The Christoffel Symbols in the momentum equation

The integration of Equations (17) and (27) over a generic surface element of area ΔA is given by the following expression

$$\iint_{\Delta A} \frac{\partial \mathrm{H}}{\partial t} dA + \iint_{\Delta A} M^{l}_{,l} dA = 0$$

(29)

$$\iint_{\Delta A} \frac{\partial \mathrm{D^l}}{\partial t} dA + \iint_{\Delta A} \left(\frac{M^l M^m}{H} + G g^{lm} \frac{H\hat{}2}{2} \right)_{,\mathrm{m}} dA$$

$$= \iint_{\Delta A} G(\eta - \eta_c)(g^{lm} h)_{,m} dA + \iint_{\Delta A} G\eta_c (g^{lm} h)_{,m} dA + \iint_{\Delta A} G \left(g^{lm} \frac{h\hat{}2}{2} \right)_{,\mathrm{m}} dA$$

$$+ \iint_{\Delta A} \frac{\partial H}{\partial t} (V'^{l} - \bar{v}^{l}) dA + \iint_{\Delta A} H \bar{v}^{l}_{,m} u^{m} dA + \iint_{\Delta A} H u^{l}_{,m} \bar{v}^{m} dA + \iint_{\Delta A} H \bar{v}^{l}_{,m} \bar{v}^{m} dA$$

$$- \iint_{\Delta A} H \left(V''^{l} + T^{l} + W^{l} + R^{l} \right) dA$$

(30)

in which η_c is the value of the free surface elevation averaged over ΔA. By developing the covariant derivatives in Equation (30) and given that $dA = \sqrt{g} d\xi^1 d\xi^2$, Equation (30) becomes

$$\iint_{\Delta A} \frac{\partial \mathrm{D}^{\mathrm{l}}}{\partial t}\sqrt{g}d\xi^1 d\xi^2 + \iint_{\Delta A} \frac{\partial}{\partial \xi^m}\left[\sqrt{\mathrm{g}}\left(\frac{M^l M^m}{H} + G g^{lm}\frac{H^{\wedge 2}}{2}\right)\right] d\xi^1 d\xi^2$$

$$= -\iint_{\Delta A} \Gamma^l_{mk}\left(\frac{M^m M^k}{H} + G g^{mk}\frac{H^{\wedge 2}}{2}\right)\sqrt{g}d\xi^1 d\xi^2$$

$$+ G\iint_{\Delta A}(\eta - \eta_c)\frac{\partial\left(g^{lm}h\sqrt{g}\right)}{\partial \xi^m}d\xi^1 d\xi^2 + \iint_{\Delta A} G\eta_c \frac{\partial\left(g^{lm}h\sqrt{g}\right)}{\partial \xi^m}d\xi^1 d\xi^2$$

$$+ \frac{\mathrm{G}}{2}\iint_{\Delta A}\frac{\partial\left(g^{lm}h^{\wedge 2}\sqrt{g}\right)}{\partial \xi^m}d\xi^1 d\xi^2$$

$$+ \iint_{\Delta A}\left[\Gamma^l_{mk} G g^{mk}\left((\eta - \eta_c)h + \eta_c h - \frac{h^{\wedge 2}}{2}\right)\right]\sqrt{g}d\xi^1 d\xi^2$$

$$+ \iint_{\Delta A}\frac{\partial H}{\partial t}\left(V^{\prime l} - \bar{v}^l\right)\sqrt{g}d\xi^1 d\xi^2 + \iint_{\Delta A} H\frac{\partial \bar{v}^l}{\partial \xi^m}u^m\sqrt{g}d\xi^1 d\xi^2$$

$$+ \iint_{\Delta A} H\frac{\partial u^l}{\partial \xi^m}\bar{v}^m\sqrt{g}d\xi^1 d\xi^2 + \iint_{\Delta A} H\frac{\partial \bar{v}^l}{\partial \xi^m}\bar{v}^m\sqrt{g}d\xi^1 d\xi^2$$

$$+ \iint_{\Delta A}\left[H\Gamma^l_{mk}(\bar{v}^k u^m + u^k\bar{v}^m + \bar{v}^k\bar{v}^m)\right]\sqrt{g}d\xi^1 d\xi^2$$

$$- \iint_{\Delta A} H\left(V^{\prime\prime l} + T^l + W^l + R^l\right)\sqrt{g}d\xi^1 d\xi^2 \tag{31}$$

On the right hand side of Equation (31), the first double integral contains the Christoffel symbols related to the convective terms and the square of the total local depth, the fifth double integral contains the Christoffel symbols related to the bottom slope, while the tenth double integral contains the Christoffel symbols related to the gradients of the vectors whose contravariant components are u^l e $\bar{v}^l$. It is evident that the presence of the first double integral on the right hand side of Equation (31) does not make it possible to convert the convective terms and the term related to the gradient of the square of the total local depth of Equation (27) into a conservative form, i.e. does not make it possible to convert these terms into fluxes across the cell interfaces.

1.3.2. The integral form of FNBE

In order to obtain the new contravariant integral form of the FNBE devoid of Christoffel symbols, the strategy defined by Gallerano et al. [2011] is followed. We consider a constant parallel vector field and equate the rate of change of momentum of a material volume to the net force in the

direction defined by this vector field. We select, as the parallel vector field, the one which is parallel to $\vec{g}^{(l)}(\xi_0^1, \xi_0^2)$, which represents the contravariant base vector defined in point $P_0(\xi_0^1, \xi_0^2) \in \Delta A$ and which is normal to the coordinate line where ξ^l is constant. We indicate with $\lambda_k(\xi^1 \xi^2)$ the generic covariant vector component of $\vec{g}^{(l)}(\xi_0^1, \xi_0^2)$, given by

$$\lambda_k(\xi^1, \xi^2) = \vec{g}^{(l)}(\xi_0^1, \xi_0^2) \cdot \vec{g}_{(k)}(\xi^1, \xi^2) \tag{32}$$

hereinafter, we denote $\vec{g}^{(l)}(\xi_0^1, \xi_0^2)$ by $\vec{\tilde{g}}^{(l)}$ and $\vec{g}_{(k)}(\xi^1, \xi^2)$ by $\vec{g}_{(k)}$. By integrating Equation (27) over the generic surface element of area ΔA, by projecting this equation along the direction λ_k, by considering that $\lambda_{k,m} = 0$, by applying Green's theorem, by using Equation (32), and by recalling that $\vec{g}^{(l)} \cdot \vec{g}_{(k)} = \delta_{lk}$ (where δ_{lk} is the Kronecker symbol), we obtain

$$\begin{aligned}
&\iint_{\Delta A} \vec{\tilde{g}}^{(l)} \cdot \vec{g}_{(k)} \frac{\partial \mathrm{D}^k}{\partial t} dA + \int_L \left(\vec{\tilde{g}}^{(l)} \cdot \vec{g}_{(k)} \frac{M^k M^m}{H} + G \vec{\tilde{g}}^{(l)} \cdot \vec{\mathrm{g}}^{(\mathrm{m})} \frac{H\hat{}2}{2} \right) n_m dL \\
&= \iint_{\Delta A} G(\eta - \eta_c) \vec{\tilde{g}}^{(l)} \cdot \vec{\mathrm{g}}^{(\mathrm{m})} h_{,m} dA + \int_L G \eta_c \vec{\tilde{g}}^{(l)} \cdot \vec{\mathrm{g}}^{(\mathrm{m})} h n_m dL \\
&+ \int_L G \vec{\tilde{g}}^{(l)} \cdot \vec{\mathrm{g}}^{(\mathrm{m})} \frac{h\hat{}2}{2} n_m dL + \iint_{\Delta A} \vec{\tilde{g}}^{(l)} \cdot \vec{g}_{(k)} \frac{\partial H}{\partial t} (V'^k - \bar{v}^k) dA \\
&+ \iint_{\Delta A} H \left(\vec{\tilde{g}}^{(l)} \cdot \vec{g}_{(k)} \bar{v}^k \right)_{,\mathrm{m}} u^m dA + \iint_{\Delta A} H \left(\vec{\tilde{g}}^{(l)} \cdot \vec{g}_{(k)} u^k \right)_{,\mathrm{m}} \bar{v}^m dA \\
&+ \iint_{\Delta A} H \left(\vec{\tilde{g}}^{(l)} \cdot \vec{g}_{(k)} \bar{v}^k \right)_{,\mathrm{m}} \bar{v}^m dA - \iint_{\Delta A} H \vec{\tilde{g}}^{(l)} \cdot \vec{g}_{(k)} \left(V''^{\mathrm{k}} + T^{\mathrm{k}} + \mathrm{W}^{\mathrm{k}} + \mathrm{R}^{\mathrm{K}} \right) dA
\end{aligned} \tag{33}$$

Applying Green's theorem to the second term on the left hand side of Equation (29), the continuity equation becomes

$$\iint_{\Delta A} \frac{\partial \mathrm{H}}{\partial t} dA + \int_L M^m n_m dL = 0 \tag{34}$$

where L is the contour line of the surface element of area ΔA and n_m is the m-th component of the covariant outward normal.

Equations (33) and (34) represent a new integral form of the FNBE expressed in a contravariant formulation in which Christoffel symbols are absent. These equations are accurate to $O(\mu^2, \varepsilon^3\mu^2)$ in dispersive terms (Wei at al [1995]) and conserve vertical vorticity with a leading-order error of $O(\mu^4)$, in accordance with the formulation proposed by Chen et al [2006].

In the above mentioned equations the conserved variables are H and M^l, consequently the momentum balance equation differs from the one presented by Gallerano et al [2014] for the different expression of the convective terms. Furthermore, unlike the Gallerano et al [2014] model, in the continuity equation no dispersive term is present. This result make it possible to solve the continuity equation entirely by a high order shock capturing finite volume scheme. In this way in the numerical solution the errors due to the discretization of the dispersive term in the continuity equation are not introduced. The surface gradient term has been split in agreement with the line presented by Xing and Shu [2006], in order to solve this term by a finite volume technique and to obtain a "well balanced" numerical scheme.

1.4. Numerical Scheme

The discretization of the computational domain is based on a grid defined by the coordinate lines ξ^1 and ξ^2 and by the points of coordinates $\xi^1 = i\Delta\xi^1$ and $\xi^2 = j\Delta\xi^2$, which represent the centre of the calculation cells; t^n is the time level of the known variables, while t^{n+1} is the time level of the unknown variables. A restrictive condition on the surface element of area ΔA is introduced: we consider the surface element bounded by four curves lying on the coordinate lines. Since $dA = \sqrt{g}d\xi^1 d\xi^2$, we indicate with $\widetilde{\mathrm{H}}$ the average value of H over the surface element of area ΔA

$$\widetilde{H} = \frac{1}{\Delta A}\iint_{\Delta A} \mathrm{H}\sqrt{g}d\xi^1 d\xi^2 \tag{35}$$

By dividing Equation (34) by ΔA and by using Equation (35), Equation (34) can be rewritten as

$$\frac{\partial \widetilde{H}}{\partial t} = -\frac{1}{\Delta A}\sum_{\mu=1}^{2}\left[\int_{\Delta\xi^{\mu+}} M^{\mu}\sqrt{g}d\xi^{\nu} - \int_{\Delta\xi^{\mu-}} M^{\mu}\sqrt{g}d\xi^{\nu}\right] \tag{36}$$

Where $\Delta\xi^{\mu+}$ and $\Delta\xi^{\mu-}$represents the segments of the contour line on which ξ^{μ} is constant, and which are located at the largest and smallest value of ξ^{μ}, respectively.

We indicate by $\widetilde{D}^l$ the averaged value of D^lover the surface element of area ΔA, defined as

$$\widetilde{D}^l = \frac{1}{\Delta A}\iint_{\Delta A} \mathrm{D}^{\mathrm{l}}\sqrt{g}d\xi^1 d\xi^2 \tag{37}$$

By dividing Equation (33) by ΔA and by using Equation (37), Equation (33) can be rewritten as

$$\frac{\partial \widetilde{D}^l}{\partial t} = \frac{1}{\Delta A}\Bigg\{ - \sum_{\mu=1}^{2} \Bigg[\int_{\Delta\xi^{\mu+}} \left(\vec{\tilde{g}}^{(l)} \cdot \vec{g}_{(k)} \frac{M^k M^\mu}{H} + \vec{\tilde{g}}^{(l)} \cdot \vec{g}^{(\mu)} G \frac{H\hat{}2}{2} \right) \sqrt{g} d\xi^\nu$$

$$- \int_{\Delta\xi^{\mu-}} \left(\vec{\tilde{g}}^{(l)} \cdot \vec{g}_{(k)} \frac{M^k M^\mu}{H} + \vec{\tilde{g}}^{(l)} \cdot \vec{g}^{(\mu)} G \frac{H\hat{}2}{2} \right) \sqrt{g} d\xi^\nu \Bigg]$$

$$+ \iint_{\Delta A} G(\eta - \eta_c) \vec{\tilde{g}}^{(l)} \cdot \vec{g}_{(k)} g^{km} h_{,m} \sqrt{g} d\xi^1 d\xi^2$$

$$+ G\eta_c \sum_{\mu=1}^{2} \left[\int_{\Delta\xi^{\mu+}} \vec{\tilde{g}}^{(l)} \cdot \vec{g}^{(\mu)} h \sqrt{g} d\xi^\nu - \int_{\Delta\xi^{\mu-}} \vec{\tilde{g}}^{(l)} \cdot \vec{g}^{(\mu)} h \sqrt{g} d\xi^\nu \right]$$

$$+ \frac{G}{2} \sum_{\mu=1}^{2} \left[\int_{\Delta\xi^{\mu+}} \vec{\tilde{g}}^{(l)} \cdot \vec{g}^{(\mu)} h\hat{}2 \sqrt{g} d\xi^\nu - \int_{\Delta\xi^{\mu-}} \vec{\tilde{g}}^{(l)} \cdot \vec{g}^{(\mu)} h\hat{}2 \sqrt{g} d\xi^\nu \right]$$

$$- \iint_{\Delta A} H \vec{\tilde{g}}^{(l)} \cdot \vec{g}_{(k)} V''^k dA - \iint_{\Delta A} H \vec{\tilde{g}}^{(l)} \cdot \vec{g}_{(k)} T^k dA - \iint_{\Delta A} H \vec{\tilde{g}}^{(l)} \cdot \vec{g}_{(k)} W^k dA$$

$$- \iint_{\Delta A} H \vec{\tilde{g}}^{(l)} \cdot \vec{g}_{(k)} R^k dA + \iint_{\Delta A} \vec{\tilde{g}}^{(l)} \cdot \vec{g}_{(k)} \frac{\partial H}{\partial t} (V'^k - \bar{v}^k) dA$$

$$+ \iint_{\Delta A} H \left(\vec{\tilde{g}}^{(l)} \cdot \vec{g}_{(k)} \bar{v}^k \right)_{,\mathrm{m}} u^m dA + \iint_{\Delta A} H \left(\vec{\tilde{g}}^{(l)} \cdot \vec{g}_{(k)} u^k \right)_{,\mathrm{m}} \bar{v}^m dA$$

$$+ \iint_{\Delta A} H \left(\vec{\tilde{g}}^{(l)} \cdot \vec{g}_{(k)} \bar{v}^k \right)_{,\mathrm{m}} \bar{v}^m dA \Bigg\} \tag{38}$$

The numerical integration of Equations (36) and (38) is carried out by a high order Upwind-WENO scheme that uses a genuinely two-dimensional reconstruction procedure. We indicate by $\boldsymbol{L}(M^1, M^2)$ the right hand side of Equation (36). We denote by $\boldsymbol{D}(H, M^1, M^2)$ the sum of the convective terms, the terms related to the gradient of the square of the total local depth and the source terms related to the bottom slope on the right hand side of Equation (38), while we indicate by $\boldsymbol{D_B}(H, M^1, M^2)$ the sum of the dispersive terms, the terms related to the approximation to the second order of the vertical vorticity and the terms related to the gradient of the vectors whose contravariant components are u^l and $\bar{v}^l$.

By integrating Equations (36) and (38) over the time interval $[t^n, t^{n+1}]$, we get

$$\widetilde{H}_{i;j}^{(n+1)} = \widetilde{H}_{i;j}^{(n)} - \frac{1}{\Delta A}\int_{t^n}^{t^{n+1}} \boldsymbol{L}(M^1, M^2)dt \tag{39}$$

$$\widetilde{D}_{i;j}^{l(n+1)} = \widetilde{D}_{i;j}^{l(n)} - \frac{1}{\Delta A}\int_{t^n}^{t^{n+1}} [\boldsymbol{D}(H, M^1, M^2) + \boldsymbol{D_B}(H, M^1, M^2)]dt \tag{40}$$

Equations (39) and (40) represent the advancing from t^n to t^{n+1} of the variables $\widetilde{H}_{i;j}$ and $\widetilde{D}_{i;j}^{l}$. The state of the system is known at the centre of the calculation cells, and it is defined by the cell averaged values $\widetilde{H}_{i;j}$ and $\widetilde{D}_{i;j}^{l}$. The time integration of Equations (39) and (40) is carried out by a third order accurate Strong Stability Preserving Runge-Kutta (SSPRK) method (Spiteri and Ruuth [2002]). The SSPRK method can be written in compact form as

$$\widetilde{H}_{i;j}^{(0)} = \widetilde{H}_{i;j}^{(n)} \;\; ; \;\; \widetilde{D}_{i;j}^{l(0)} = \widetilde{D}_{i;j}^{l(n)} \tag{41}$$

$$\widetilde{H}_{i;j}^{(p)} = \sum_{q=0}^{p-1}\left\{\Omega_{pq}H_{i,j}^{(q)} + \Delta t\varphi_{pq}\left[\boldsymbol{L}\left(M^{1(q)}, M^{2(q)}\right)\right]\right\} \tag{42}$$

$$\widetilde{D}_{i;j}^{l(p)} = \sum_{q=0}^{p-1}\left\{\Omega_{pq}D_{i,j}^{l(p)} + \Delta t\varphi_{pq}\left[\boldsymbol{D}\left(H^{(q)}, M^{1(q)}, M^{2(q)}\right) + \boldsymbol{D_B}(H^{(p)}, M^{1(p)}, M^{2(p)})\right]\right\} \tag{43}$$

$$\widetilde{H}_{i;j}^{(n+1)} = \widetilde{H}_{i;j}^{(3)} \;\; ; \;\; \widetilde{D}_{i;j}^{l(n+1)} = \widetilde{D}_{i;j}^{l(3)} \tag{44}$$

where p = 1,2,3. See Spiteri and Ruuth [2002] for the value of the coefficients Ω_{pq} and φ_{pq}. The calculation of $\boldsymbol{L}(M^1, M^2)$, $\boldsymbol{D}(H, M^1, M^2)$ and $\boldsymbol{D_B}(H, M^1, M^2)$ terms requires a numerical approximation of the spatial integrals on the right hand side of Equations (36) and (38). This approximation is achieved by a hybrid finite volume-finite difference scheme, in agreement with the strategy proposed by Erduran et al. [2005] and used by Tonelli and Petti [2012] and Shi et al. [2012].

By applying this method, once the auxiliary variable $\widetilde{D}^l$ value is known, we calculate the value of the original variable $\tilde{u}^l$ at every Runge-Kutta step by solving the equation

$$\widetilde{D}^l = \widetilde{H}(\tilde{u}^l + \tilde{V}'^l) \tag{45}$$

where $\tilde{V}'^{l}$ includes second derivatives of $\tilde{u}^{l}$ with respect to ξ^1 and $\xi^2$and cross derivatives (see Equation (24)). The numerical approximation of the derivatives in the $\tilde{V}'^{l}$ term is carried out via a second order centred finite difference scheme. The velocity at elevation σ, averaged over the generic computational cell $I_{i,j}$, and indicated with $\tilde{u}^{l}_{i;j}$, can be calculated by solving the system of Equation (45), in which the coefficient matrix is tridiagonal. Once the values of the $\tilde{u}^{l}_{i;j}$ are known, the $\boldsymbol{D_B}(H, M^1, M^2)$ term on the right hand side of Equation (38) is discretized by using a second order centred finite difference scheme at the cell centroids, as in Wei and Kirby [1995], Shi et al [2012]. Since $\boldsymbol{D_B}(H, M^1, M^2)$ needs to be updated using $H, u^1, u^2, \bar{v}^1, \bar{v}^2$ at the corresponding time step, an iteration is needed to achieve convergence, as suggested by Shi et al. [2012].
The right hand side of the continuity Equation (36), represented by the $\boldsymbol{L}(M^1, M^2)$ term, and the sum of the convective terms, of the terms related to the gradient of the square of the total local depth and the source term related to the bottom slope of the momentum balance Equation (38), represented by the $\boldsymbol{D}(H, M^1, M^2)$ term, are discretized by a high order finite volume Upwind-WENO scheme. Consequently, the entire continuity equation and the conservative part of the momentum balance equation are solved by a high order Shock-Capturing scheme. This numerical scheme is based on the following steps:

- Starting from the averaged cell values, the point values of the unknown variables at the centre of the contour segments which define the cell faces are calculated by a genuinely two-dimensional UPWIND-WENO reconstruction procedure based on biquadratic polynomials.

- The point values of the variables at the centre of the contour segments, are updated in time by the so-called exact solution of a local Riemann problem, with the initial data given by the pair of point values computed by two 2D-WENO reconstructions defined on the two adjacent cells. In accordance with the procedure proposed by Rossmanith et al. [2004], all Riemann problems are solved in a local orthonormal basis system. This orthonormalization makes it possible to solve the Riemann problems in a local Cartesian coordinate system, in which no geometric terms are present.

- The spatial integrals that define the $\boldsymbol{L}(M^1, M^2)$ and $\boldsymbol{D}(H, M^1, M^2)$ terms are numerically approximated by a high order quadrature rule, starting from the point values of the dependent variables computed at the previous step.

1.4.1. Genuinely 2D reconstructions

The high-order finite volume Shock-Capturing scheme described in this thesis requires the calculation of the point values of the conserved variables H and M^l at cell faces.

The reconstruction of the point values of H at the interface of computational cells is achieved by a surface gradient method proposed by Zhou et al [2001] and used by many authors in the context of high order shock capturing schemes (Shi et al [2012], Roeber et al [2012]).

According to Zhou et al. [2001], reconstruction of the surface elevation η instead of the flow depth H reduces spurious oscillations over irregular bathymetry. This ensures satisfaction of the so-called C-property for a well-balanced finite volume scheme that can maintain quiescent conditions for a water body at rest (Vázquez-Cendón, [1999]).

The choice of reconstructing the components of the conserved variable $\vec{M}$, instead of the component of the velocity (u^1,u^2), is consistent with the line implemented in literature in the context of the resolution of the depth averaged equations by a shock capturing scheme (Caleffi et al [2006], Caleffi and Valiani [2009], Xing and Shu [2011]). In fact as demonstrated by the above mentioned authors, the choice of using the surface gradient method and reconstructing the components of the conserved variable $\vec{M}$, makes it possible to carry out shock capturing numerical schemes with good steady state conservation properties.

In this work a new genuinely two-dimensional WENO reconstruction procedure for the conserved variables H and M^l on the cells faces is described.

By following the line defined by Levy et al. [2002] in the context of 2D Central WENO schemes, the proposed procedure takes simultaneously into account all the computing cells included in the two-dimensional stencil in order to obtain a genuinely 2D interpolating function, defined by a convex combination of biquadratic polynomials.

The WENO reconstructions of the point values of the contravariant components of the vector $\vec{M}$ may be affected by the spatial variability of the metric terms. As results from the third relation in (4), the contravariant components b^l of the generic vector $\vec{b}$, represent the vector components with respect to the basis defined by the covariant base vectors $\vec{g}_{(l)}$, which vary in direction and magnitude over space; therefore the contravariant components M^l and their WENO reconstructions depend on the variability over space of the base vectors. In order to eliminate the dependence of the WENO reconstructions of the components of the vector $\vec{M}$ on the variability over space of the base vectors, we apply the WENO reconstruction procedure to components of the vector $\vec{M}$ with respect

to a basis defined by a pair of constant unit vectors. Such pair of base vectors is defined by the unit vectors which are parallel to the covariant base vectors in the generic point P_0 with coordinates (ξ_0^1, ξ_0^2). The above-mentioned unit base vectors are given by $\vec{\tilde{g}}_{(l)}\sqrt{g_{ll}}$ (no sum on the repeated index l).

In point P_0, the components of the vector $\vec{M}$ with respect to these unit base vectors are given by $N^l(\xi_0^1, \xi_0^2) = M^l\sqrt{g_{ll}}$ (no sum on the repeated index l) and are named 'physical contravariant components' (Aris [1989]). The cell averaged physical contravariant components $\widetilde{N}^l(\xi^1, \xi^2)$, defined in the generic point P with coordinates (ξ^1, ξ^2) different from P_0, which are involved in the WENO reconstructions of $N^l(\xi_0^1, \xi_0^2)$ are given by

$$\widetilde{N}^l(\xi^1, \xi^2) = \sqrt{g_{ll}}\vec{\tilde{g}}^{(l)} \cdot \vec{\tilde{g}}_{(k)}\widetilde{M}^k \tag{46}$$

(no sum on the repeated index l). From the cell averaged values $\widetilde{H}_{i;j}$ and $\widetilde{N}^l_{i;j}$, defined on the cell $I_{i;j}$, the point values (at the centre of the segments defining the contours of the cell $I_{i;j}$) $H_{i+p;j+q}$ and $N^l_{i+p;j+q}$ (with $p = -\frac{1}{2}, \frac{1}{2}$ and $q = -\frac{1}{2}, \frac{1}{2}$) are reconstructed. In the following, only the reconstruction of the point values N^l is shown. The reconstruction of the point values $N^l_{i-\frac{1}{2};j}$ and $N^l_{i+\frac{1}{2};j}$ is performed starting from the cell averages $\widetilde{N}^l_{i;j}$.

Such reconstruction is carried out in each cell $I_{i;j}$ by constructing a biquadratic polynomial $R_{i;j}(\xi^1, \xi^2)$, which is a convex combination of nine biquadratic polynomials $P_{i+p;j+q}(\xi^1, \xi^2)$ (with $p = -1,0,1$ e $q = -1,0,1$) centered in cells adjacent to $I_{i;j}$

$$R_{i;j}(\xi^1, \xi^2) = \sum_{l,k=-1}^{1} \omega^{l,k}_{i,j} P_{i+l;j+k}(\xi^1, \xi^2) \tag{47}$$

The nine biquadratic polynomials $P_{i+p;j+q}(\xi^1, \xi^2)$ are given by

$$\begin{aligned} P_{i+p,j+q}(\xi^1\xi^2) \\ &= b_0 + b_1(\xi^1 - \xi_i^1) + b_2(\xi^2 - \xi_i^2) + b_3(\xi^1 - \xi_i^1)(\xi^2 - \xi_i^2) + b_4(\xi^1 - \xi_i^1)\hat{}2 \\ &+ b_5(\xi^2 - \xi_i^2)\hat{}2 + b_6(\xi^1 - \xi_i^1)\hat{}2(\xi^2 - \xi_i^2) + b_7(\xi^1 - \xi_i^1)(\xi^2 - \xi_i^2)\hat{}2 \\ &+ b_8(\xi^1 - \xi_i^1)\hat{}2(\xi^2 - \xi_i^2)\hat{}2 \end{aligned} \tag{48}$$

where, the indexes of coefficients b_m (m = 0, .., 8) are omitted.

The weights $\omega_{i,j}^{l,k}$ used in Equation (47) are calculated by using a non-linear algorithm that satisfy the stability requirement $\omega_{i,j}^{l,k} \geq 0$, and the conservation requirement $\sum_{l,k=-1}^{1} \omega_{i,j}^{l,k} = 1$; with *l*,*k*=-1,0,1, in which *l* is associated to the ξ^1 coordinate, while *k* is associated to the ξ^2 coordinate. The $\omega_{i,j}^{l,k}$ values are a function of linear weights and indexes of smoothness.

The indexes of smoothness are calculated by using a suitable function of the norms of polynomial derivatives on the cell $I_{i;j}$; the linear weights are chosen in order to maximize the accuracy in regions where the solution is smooth, as suggested by Levy et al [2002].

In curvilinear coordinates, the weights calculated in the WENO reconstruction procedure may be affected by the Jacobian term spatial variation. Consequently, as suggested by Nonomura et al. [2010], in order to not include these terms in the WENO reconstruction, the cell averaged value of the variable $N_{i;j}^{m}$ is approximated by

$$\widetilde{N}_{i+p+l;j+q+k}^{m} = \frac{1}{\Delta\xi^1\Delta\xi^2}\int_{\xi_i^1-\frac{\Delta\xi^1}{2}+(l+p)\Delta\xi^1}^{\xi_i^1+\frac{\Delta\xi^1}{2}+(l+p)\Delta\xi^1} \int_{\xi_i^2-\frac{\Delta\xi^2}{2}+(k+q)\Delta\xi^2}^{\xi_i^2+\frac{\Delta\xi^2}{2}+(k+q)\Delta\xi^2} N_{i+p+l;j+q+k}^{m}\left(\xi^1,\xi^2\right)\mathrm{d}\xi^1\mathrm{d}\xi^2 \tag{49}$$

By imposing the following relationship

$$\begin{aligned}&\frac{1}{\Delta\xi^1\Delta\xi^2}\int_{\xi_i^1-\frac{\Delta\xi^1}{2}+(l+p)\Delta\xi^1}^{\xi_i^1+\frac{\Delta\xi^1}{2}+(l+p)\Delta\xi^1} \int_{\xi_i^2-\frac{\Delta\xi^2}{2}+(k+q)\Delta\xi^2}^{\xi_i^2+\frac{\Delta\xi^2}{2}+(k+q)\Delta\xi^2} N_{i+p+l;j+q+k}^{m}\left(\xi^1,\xi^2\right)\mathrm{d}\xi^1\mathrm{d}\xi^2\\ &= \frac{1}{\Delta\xi^1\Delta\xi^2}\int_{\xi_i^1-\frac{\Delta\xi^1}{2}+(l+p)\Delta\xi^1}^{\xi_i^1+\frac{\Delta\xi^1}{2}+(l+p)\Delta\xi^1} \int_{\xi_i^2-\frac{\Delta\xi^2}{2}+(k+q)\Delta\xi^2}^{\xi_i^2+\frac{\Delta\xi^2}{2}+(k+q)\Delta\xi^2} P_{i+p+l;j+q+k}\left(\xi^1,\xi^2\right)\mathrm{d}\xi^1\mathrm{d}\xi^2\end{aligned} \tag{50}$$

Equation (49) becomes

$$\widetilde{N}_{i+p+l;j+q+k}^{m} = \frac{1}{\Delta\xi^1\Delta\xi^2}\int_{\xi_i^1-\frac{\Delta\xi^1}{2}+(l+p)\Delta\xi^1}^{\xi_i^1+\frac{\Delta\xi^1}{2}+(l+p)\Delta\xi^1} \int_{\xi_i^2-\frac{\Delta\xi^2}{2}+(k+q)\Delta\xi^2}^{\xi_i^2+\frac{\Delta\xi^2}{2}+(k+q)\Delta\xi^2} P_{i+p+l;j+q+k}\left(\xi^1,\xi^2\right)d\xi^1 d\xi^2 \tag{51}$$

By introducing the analytical solution of the integral into Equation (51), 9 independent systems are

obtained ($p = -1,0,1$ and $q = -1,0,1$), each of which is formed by nine linear equations ($l = -1,0,1$ and $k = -1,0,1$) which make it possible to compute the nine b_m coefficients of each polynomial. Once these coefficients and the indexes of smoothness are computed, $R_{i;j}(\xi^1, \xi^2)$ is calculated, from which the N^l values in the centre of each cell face are obtained

$$N^l_{i-\frac{1}{2};j} = R_{\mathrm{i;j}}\left(\xi^1_{i-\frac{1}{2}}, \xi^2_{\mathrm{j}}\right) \quad ; \quad N^l_{i;j-\frac{1}{2}} = R_{\mathrm{i;j}}\left(\xi^1_{i}, \xi^2_{\mathrm{j}-\frac{1}{2}}\right) \tag{52}$$

$$N^l_{i+\frac{1}{2};j} = R_{i;j}\left(\xi^1_{i+\frac{1}{2}}, \xi^2_{\mathrm{j}}\right) \quad ; \quad N^l_{i;j+\frac{1}{2}} = R_{i;j}\left(\xi^1_{i}, \xi^2_{\mathrm{j}+\frac{1}{2}}\right) \tag{53}$$

1.4.2. Wetting drying scheme

In numerical integration of NSWE a particular treatment of the wet and dry front in the swash zone, to model a moving shoreline, is required (Shi et al [2012]). In order to simulate the up rush and the backwash dynamics of the wet and dry front in the swash zone, the following original procedure is proposed.

Subsequently the procedure of the up rush and the backwash dynamics of the wet and dry front is exposed referenced to a shoreline which is parallel to the curvilinear coordinate line ξ^2. At the centre of the segments which separate the dry cell $I_{i;j}$ from the wet cell $I_{i-1;j}$, point values of the unknown variables are reconstructed, by means of an asymmetric WENO reconstruction defined on the wet cell. For example, at the centre of the segment which is the interface between dry cell $I_{i;j}$ and wet cell $I_{i-1;j}$, WENO reconstructions defined on the $I_{i-1;j}$ cells lead to the evaluation of the variables $H^{(n)-}_{i-\frac{1}{2};j}$, $M^{l(n)-}_{i-\frac{1}{2};j}$. The advancing in time of the aforementioned variables is carried out by means of the exact solution of an apposite Riemann problem, with initial data given by the pair of point-values computed by the WENO reconstruction. It must be noted that the point values of the unknown variables $H^{(n)+}_{i-\frac{1}{2};j}$ and $M^{l(n)+}_{i-\frac{1}{2};j}$ are equal to zero because they belong to the dry cell $I_{i;j}$.

Generally speaking, the Riemann problem in a curvilinear coordinate system is more difficult to solve than the Riemann problem for the same set of hyperbolic equations in an orthonormal frame. We solve all Riemann problems in a locally valid orthonormal basis.

Now we define the normal and tangential to the coordinate line ξ^2 depth-averaged velocity components as $\rho^{1(n)}$ and $\tau^{l(n)}$, respectively. As $\vec{g}^{(1)}/\sqrt{g^{11}}$ and $\vec{g}_{(2)}/\sqrt{g_{22}}$ are the unit vectors

which are normal and tangential, respectively, to the coordinate line ξ^2 and recalling relation (4), the following transformation relations are obtained

$$\rho^{1(n)} = \frac{M^{1(n)}}{H\sqrt{g^{11}}} \tag{54}$$

$$\tau^{1(n)} = \frac{M^{1(n)}}{H}\frac{g_{12}}{\sqrt{g_{22}}} + \frac{M^{2(n)}}{H}\sqrt{g_{22}} \tag{55}$$

For example, in the point of coordinates $(\xi^1_{i-\frac{1}{2}}; \xi^2_j)$ belonging to the segment that lies on coordinate line ξ^2, which is the interface of cells $I_{i-1;j}$ and $I_{i;j}$, the WENO reconstructions lead to the definition of the point values of dependent variables $H^{(n)-}_{i-\frac{1}{2};j}$, $\rho^{1(n)-}_{i-\frac{1}{2};j}$ and $\tau^{1(n)-}_{i-\frac{1}{2};j}$. Let $S^{(n+1)*}_{i-\frac{1}{2};j}$ be the propagation velocity of the wet and dry front at the advanced time level t^{n+1}. Let $H^{(n+1)*}_{i-\frac{1}{2};j}$, $\rho^{(n+1)*}_{i-\frac{1}{2};j}$, and $\tau^{(n+1)*}_{i-\frac{1}{2};j}$ be the solution of the wet and dry Riemann problem defined by the hyperbolic homogenous system of the Shallow Water Equations, written in the locally valid orthonormal basis. The exact solution of this Riemann problem on the interface common to the wet cell $I_{i-1;j}$ and to the dry cell $I_{i;j}$, gives

$$H^{(n+1)*}_{i-\frac{1}{2};j} = \frac{1}{G}\left(\frac{1}{3}\left(\rho^{1(n)-}_{i-\frac{1}{2};j} + 2\left(GH^{(n)-}_{i-\frac{1}{2};j}\right)^{1/2}\right)\right)^{1/2} \tag{56}$$

$$\rho^{(n+1)*}_{i-\frac{1}{2};j} = \frac{1}{3}\left(\rho^{1(n)-}_{i-\frac{1}{2};j} + 2\left(GH^{(n)-}_{i-\frac{1}{2};j}\right)^{1/2}\right) \tag{57}$$

$$\tau^{(n+1)*}_{i-\frac{1}{2};j} = \tau^{1(n)-}_{i-\frac{1}{2};j} \tag{58}$$

$$S^{(n+1)*}_{i-\frac{1}{2};j} = \rho^{1(n)-}_{i-\frac{1}{2};j} + 2\left(GH^{(n)-}_{i-\frac{1}{2};j}\right)^{1/2} \tag{59}$$

Let $dbx^{(n+1)}_{i-\frac{1}{2};j}$ be the distance of the wet and dry front from the interface common to the wet cell $I_{i-1;j}$ and to the dry cell $I_{i;j}$. Such distance is given by

$$dbx_{i-\frac{1}{2};j}^{(n+1)} = dbx_{i-\frac{1}{2};j}^{(n)} + \left(\rho_{i-\frac{1}{2};j}^{1(n)-} + 2\left(GH_{i-\frac{1}{2};j}^{(n)-}\right)^{1/2}\right) \cdot \Delta n \tag{60}$$

Where Δn is the time step. Subsequently, by operating an inverse transformation of the reference system, the solution of the Riemann problem in contravariant components is evaluated.

1.5. Metric Identities

In the numerical integration of FNBE in contravariant formulation, errors related to the difficulty of numerically satisfying metric identities on generalized curvilinear grids may produce spurious oscillations in the numerical solution and errors that can be of the same order of magnitude of dispersive terms of the motion equations and which can compromise the capacity of the numerical scheme to preserve the shape of a wave that propagates on a flat bottom. Moreover, the failure to numerically satisfy the metric identities affects the ability of the numerical scheme to preserve a still water state on a non-uniform bed.

The metric identities express, either in integral or differential form, the geometric requirement according to which each cell of the computational domain must be closed (Vinokur [1989]). This geometric requirement is expressed by the following relationship

$$\oint_L \vec{n}\, dL = 0 \tag{61}$$

where L is the contour line of the calculation cell, and $\vec{n}$ the vector which is normal to the contour line. In a generalized curvilinear coordinate system Equation (61) results in the following metric identity in integral form as

$$\sum_{\mu=1}^{2} \left[\int_{\Delta\xi^{\mu+}} \vec{g}^{(\mu)}\sqrt{g}\, d\xi^{\nu} - \int_{\Delta\xi^{\mu-}} \vec{g}^{(\mu)}\sqrt{g}\, d\xi^{\nu}\right] = 0 \tag{62}$$

In which (μ,ν) are cyclic.

By dividing Equation (62) by the area of the calculation cell, $\Delta A = \iint \sqrt{g} d\xi^1 d\xi^2$, and by applying the limit as ΔA tends to zero, the metric identity in differential form is obtained

$$\frac{\partial \vec{g}^{(\mu)}\sqrt{g}}{\partial \xi^{\mu}} = 0 \tag{63}$$

It is possible to demonstrate that the left hand side of the metric identity (63) is implicitly contained in the sum of the integrals on the right hand side of the continuity Equation (36) and in each of the sums of the simple integrals on the right hand side of the balance momentum Equation (38). In fact the sum of the integrals on the right hand side of Equation (36), can be expressed in the following form

$$\frac{1}{\Delta A}\sum_{\mu=1}^{2}\left[\int_{\Delta\xi^{\mu+}} M^{\mu}\sqrt{g}d\xi^{\nu} - \int_{\Delta\xi^{\mu-}} M^{\mu}\sqrt{g}d\xi^{\nu}\right] = \frac{1}{\Delta A}\iint_{\Delta A}\frac{\partial}{\partial\xi^{\mu}}\left[\mathrm{M}^{\mu}\sqrt{g}\right]d\xi^{1}d\xi^{2} \tag{64}$$

Using $M^{\mu} = \vec{M}\cdot\vec{\mathrm{g}}^{(\mu)}$, the second member of Equation (64), can be written as

$$\frac{1}{\Delta A}\iint_{\Delta A}\frac{\partial}{\partial\xi^{\mu}}\left[\mathrm{M}^{\mu}\sqrt{g}\right]d\xi^{1}d\xi^{2} = \frac{1}{\Delta A}\iint_{\Delta A}\sqrt{g}\vec{\mathrm{g}}^{(\mu)}\cdot\frac{\partial\vec{M}}{\partial\xi^{\mu}}d\xi^{1}d\xi^{2} + \frac{1}{\Delta A}\iint_{\Delta A}\vec{M}\cdot\frac{\partial\vec{\mathrm{g}}^{(\mu)}\sqrt{g}}{\partial\xi^{\mu}}d\xi^{1}d\xi^{2} \tag{65}$$

The second integral on the right hand side of Equation (65) is equal to zero, because of the metric identity (63). Equations (64) and (65) show how the metric identity is implicitly involved in the continuity Equation (36). Consequently, the errors due to the numerical approximation of the metric terms in the discretization of the left hand side of Equation (64) prevent the satisfaction of the metric identity (63).

By using an analogous procedure it is possible to show that the left hand side of the metric identity (63) is implicitly contained in each of the sums of the simple integrals on the right hand side of the balance momentum Equation (38). In fact, the sum of the convective terms and the terms related to the gradient of the square of the total local depth on the right hand side of Equation (38) can be expressed in the form

$$\frac{1}{\Delta A}\sum_{\mu=1}^{2}\left[\int_{\Delta\xi^{\mu+}}\left(\vec{\tilde{g}}^{(l)}\cdot\vec{g}_{(k)}\frac{M^{k}M^{\mu}}{H}+\vec{\tilde{g}}^{(l)}\cdot\vec{g}^{(\mu)}G\frac{H^{\wedge 2}}{2}\right)\sqrt{g}d\xi^{\nu}\right.$$

$$\left.-\int_{\Delta\xi^{\mu-}}\left(\vec{\tilde{g}}^{(l)}\cdot\vec{g}_{(k)}\frac{M^{k}M^{\mu}}{H}+\vec{\tilde{g}}^{(l)}\cdot\vec{g}^{(\mu)}G\frac{H^{\wedge 2}}{2}\right)\sqrt{g}d\xi^{\nu}\right]$$

$$=\frac{1}{\Delta A}\iint_{\Delta A}\frac{\partial}{\partial\xi^{\mu}}\left[\left(\vec{\tilde{g}}^{(l)}\cdot\vec{g}_{(k)}\frac{M^{k}M^{\mu}}{H}+\vec{\tilde{g}}^{(l)}\cdot\vec{g}^{(\mu)}G\frac{H^{\wedge 2}}{2}\right)\sqrt{g}\right]d\xi^{1}d\xi^{2}$$

(66)

Recalling the expression $M^{\mu}=\vec{M}\cdot\vec{\mathrm{g}}^{(\mu)}$, the right hand side of Equation (66) can be rewritten as

$$\frac{1}{\Delta A}\iint_{\Delta A}\frac{\partial}{\partial\xi^{\mu}}\left[\left(\vec{\tilde{g}}^{(l)}\cdot\vec{g}_{(k)}\frac{M^{k}M^{\mu}}{H}+\vec{\tilde{g}}^{(l)}\cdot\vec{g}^{(\mu)}G\frac{H^{\wedge 2}}{2}\right)\sqrt{g}\right]d\xi^{1}d\xi^{2}$$

$$=\frac{1}{\Delta A}\iint_{\Delta A}\sqrt{g}\vec{\mathrm{g}}^{(\mu)}\cdot\frac{\partial}{\partial\xi^{\mu}}\left[\left(\vec{\tilde{g}}^{(l)}\cdot\vec{g}_{(k)}\frac{\vec{\mathrm{M}}M^{k}}{H}+\vec{\tilde{g}}^{(l)}G\frac{H^{\wedge 2}}{2}\right)\right]d\xi^{1}d\xi^{2}$$

$$+\frac{1}{\Delta A}\iint_{\Delta A}\left[\left(\vec{\tilde{g}}^{(l)}\cdot\vec{g}_{(k)}\frac{\vec{\mathrm{M}}M^{k}}{H}+\vec{\tilde{g}}^{(l)}G\frac{H^{\wedge 2}}{2}\right)\right]\cdot\frac{\partial\vec{\mathrm{g}}^{(\mu)}\sqrt{g}}{\partial\xi^{\mu}}d\xi^{1}d\xi^{2}$$

(67)

By repeating the same procedure for the source term of Equation (38) relative to the bottom slope, this term can be rewritten as

$$G\eta_{c}\frac{1}{\Delta A}\sum_{\mu=1}^{2}\left[\int_{\Delta\xi^{\mu+}}\vec{\tilde{g}}^{(l)}\cdot\vec{g}^{(\mu)}h\sqrt{g}d\xi^{\nu}-\int_{\Delta\xi^{\mu-}}\vec{\tilde{g}}^{(l)}\cdot\vec{g}^{(\mu)}h\sqrt{g}d\xi^{\nu}\right]$$

$$+\frac{\mathrm{G}}{2}\frac{1}{\Delta A}\sum_{\mu=1}^{2}\left[\int_{\Delta\xi^{\mu+}}\vec{\tilde{g}}^{(l)}\cdot\vec{g}^{(\mu)}h^{\wedge 2}\sqrt{g}d\xi^{\nu}-\int_{\Delta\xi^{\mu-}}\vec{\tilde{g}}^{(l)}\cdot\vec{g}^{(\mu)}h^{\wedge 2}\sqrt{g}d\xi^{\nu}\right]$$

$$=\frac{1}{\Delta A}\iint_{\Delta A}\frac{\partial}{\partial\xi^{\mu}}\left[\left(G\eta_{c}\vec{\tilde{g}}^{(l)}\cdot\vec{g}^{(\mu)}h+\frac{\mathrm{G}}{2}\vec{\tilde{g}}^{(l)}\cdot\vec{g}^{(\mu)}h^{\wedge 2}\right)\sqrt{g}\right]d\xi^{1}d\xi^{2}$$

(68)

in which the right hand side of Equation (68) can be written as

$$\frac{1}{\Delta A}\iint_{\Delta A}\frac{\partial}{\partial\xi^{\mu}}\left[\left(G\eta_c\vec{\tilde{g}}^{(l)}\cdot\vec{g}^{(\mu)}h+\frac{G}{2}\vec{\tilde{g}}^{(l)}\cdot\vec{g}^{(\mu)}h^{\wedge 2}\right)\sqrt{g}\right]d\xi^1d\xi^2$$
$$=\frac{1}{\Delta A}\iint_{\Delta A}\sqrt{g}\vec{\mathrm{g}}^{(\mu)}\cdot\frac{\partial}{\partial\xi^{\mu}}\left(G\eta_c\vec{\tilde{g}}^{(l)}h+\frac{G}{2}\vec{\tilde{g}}^{(l)}h^{\wedge 2}\right)d\xi^1d\xi^2$$
$$+\frac{1}{\Delta A}\iint_{\Delta A}\left[G\eta_c\vec{\tilde{g}}^{(l)}h+\frac{G}{2}\vec{\tilde{g}}^{(l)}h^{\wedge 2}\right]\cdot\frac{\partial\vec{\mathrm{g}}^{(\mu)}\sqrt{g}}{\partial\xi^{\mu}}d\xi^1d\xi^2 \tag{69}$$

The second integral of the right hand side of Equation (69) and the second integral placed on the right hand side of Equation (67) are equal to zero, because of the metric identity (63).

Thus, Equations (67) and (69) show how the metric identity (63) is implicitly involved in the momentum balance Equation (38). The errors due to the numerical approximation of the metric terms in the discretization of the left hand side of Equations (67) and (69) prevent the satisfaction of the metric identity (63).

In the case of the numerical simulation of still water on a non-uniform bottom, the errors due to the failure to numerically satisfy the metric identities is evident: in these conditions, the free surface elevation with respect to the still water level is constant over the calculation cell ($\eta=\eta_c$) and the sum of the terms on the right hand side of Equations (67) and (69) becomes

$$\frac{1}{\Delta A}\iint_{\Delta A}\vec{\tilde{g}}^{(l)}\cdot\vec{\mathrm{g}}^{(\mu)}\sqrt{g}\frac{\partial}{\partial\xi^{\mu}}\left[\left(-\vec{g}_{(k)}\cdot\frac{\vec{\mathrm{M}}M^k}{H}-G\frac{H^{\wedge 2}}{2}+G\eta h+G\frac{h^{\wedge 2}}{2}\right)\right]d\xi^1d\xi^2$$
$$+\frac{1}{\Delta A}\iint_{\Delta A}\left[\left(-\vec{g}_{(k)}\cdot\frac{\vec{\mathrm{M}}M^k}{H}-G\frac{H^{\wedge 2}}{2}+G\eta h+G\frac{h^{\wedge 2}}{2}\right)\right]\vec{\tilde{g}}^{(l)}\cdot\frac{\partial\vec{\mathrm{g}}^{(\mu)}\sqrt{g}}{\partial\xi^{\mu}}d\xi^1d\xi^2$$
$$=\frac{1}{\Delta A}\iint_{\Delta A}\left[\left(-\frac{\eta^{\wedge 2}}{2}\right)\right]\mathrm{G}\vec{\tilde{g}}^{(l)}\cdot\frac{\partial\vec{\mathrm{g}}^{(\mu)}\sqrt{g}}{\partial\xi^{\mu}}d\xi^1d\xi^2$$
$$+\frac{1}{\Delta A}\iint_{\Delta A}\mathrm{G}\vec{\tilde{g}}^{(l)}\cdot\vec{\mathrm{g}}^{(\mu)}\sqrt{g}\frac{\partial}{\partial\xi^{\mu}}\left(-\frac{\eta^{\wedge 2}}{2}\right)d\xi^1d\xi^2 \tag{70}$$

where the second integral on the right hand side of Equation (70) is equal to zero, because $\eta^{\wedge 2}$ is constant, while the first integral on the right hand side of Equation (70) is not equal to zero and represents a spurious source term in the momentum balance Equation (38). As a consequence the still water condition is not preserved.

In this thesis, in order to correct the effects produced by the spurious source terms due to the difficulty of numerically satisfying the metric identities, the approximation of the terms

$$\frac{\vec{\widetilde{M}}}{\Delta A}\cdot\sum_{\mu=1}^{2}\left[\int_{\Delta\xi^{\mu+}}\vec{g}^{(\mu)}\sqrt{g}d\xi^{\nu}-\int_{\Delta\xi^{\mu-}}\vec{g}^{(\mu)}\sqrt{g}d\xi^{\nu}\right] \tag{71}$$

$$\frac{\vec{g}^{(l)}\cdot\left(\frac{\vec{\widetilde{M}}\otimes\vec{\widetilde{M}}}{\widetilde{H}}+G\frac{\widetilde{H}^{\wedge}2}{2}\right)}{\Delta A}\cdot\sum_{\mu=1}^{2}\left[\int_{\Delta\xi^{\mu+}}\vec{g}^{(\mu)}\sqrt{g}d\xi^{\nu}-\int_{\Delta\xi^{\mu-}}\vec{g}^{(\mu)}\sqrt{g}d\xi^{\nu}\right] \tag{72}$$

$$\frac{\left[G\eta_c\widetilde{h}+\frac{G}{2}\widetilde{h}^{\wedge}2\right]}{\Delta A}\vec{\tilde{g}}^{(l)}\cdot\sum_{\mu=1}^{2}\left[\int_{\Delta\xi^{\mu+}}\vec{g}^{(\mu)}\sqrt{g}d\xi^{\nu}-\int_{\Delta\xi^{\mu-}}\vec{g}^{(\mu)}\sqrt{g}d\xi^{\nu}\right] \tag{73}$$

(where in $\vec{\widetilde{M}}$, $\tilde{h}$ and $\widetilde{H}$ are averaged values over the cell of area ΔA of the quantities $\vec{M}$, h and H respectively) is introduced into the motion equations. In particular, term (71) is subtracted from the right hand side of Equation (36), while terms (72) and (73) are subtracted from the right hand side of Equation (38). The numerical approximation of these terms is carried out by using the same weights as used in the WENO reconstruction of the terms on the left hand side of Equations (36) and (38), respectively. In this way we eliminate the errors produced by the difficulty of exactly satisfying the metric identities.

1.6. Results

1.6.1. The dam-break problem on a dry bed

In the typical dam-break problem a septum divides two regions: at the left of the septum still water of initial depth h_0 is present, while at the right of the septum the region is dry (Stoker [1957]). The evolution of this initial condition upon removal of the septum, and so the suddenly release of the mound of water, is represented.

In this section the dam-break test is used to validate the adherence to the analytical solution of the solution obtained with the use of the model for the simulation of the wet and dry problem. In the case in which a septum divides the wet and dry conditions and is suddenly removed at the time t=0, we have the typical Ritter solution (Stoker [1957]) here shown in dimensionless form:

$$d^* = \frac{1}{9}\left(2 - \frac{x^*}{t^*}\right)^2 \tag{74}$$

$$u^* = \frac{2}{3}\left(\frac{x^*}{t^*} + 1\right) \tag{75}$$

Where $x^* = x/x_b$ and $t^* = t/t_b$, in which x is the coordinate, x_b is the basin length, t is the time and t_b is the duration of the simulation. The analytical solution for $h_0 = 1$ is represented by solid line in Figure 1 at different dimensionless time t^*=0.006; 0.07; 0.12; 0.2: Figure 1a shows the water depth and Figure 1b shows the velocity.

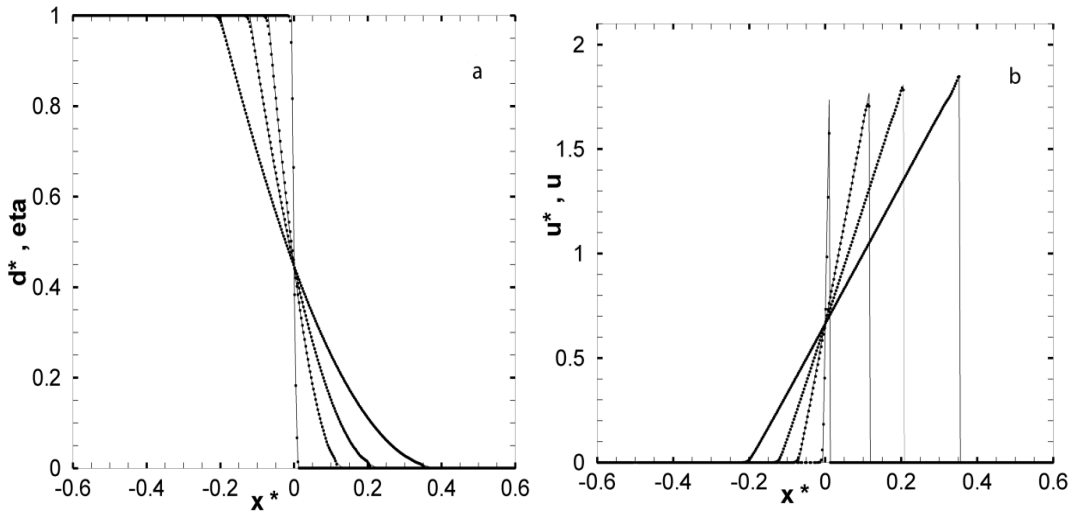

Figure 1 - The dam break problem on a dry bed. a) Water depth. b) Velocity at different dimensionless time t*=0.006,0.07,0.12,0.2. Comparison between numerical results (points)

obtained by the proposed Boussinesq model and analytical solution (solid line).

In the same Figure 1, the points indicate the numerical results obtained by using the proposed wet and dry model. It is possible to see how the numerical results are in very good agreement with the analytical solution.

1.6.2. Solitary wave run-up on a conical island

In this section we simulate the run-up of a solitary wave onto a conical Island. To this aim we numerically reproduce a laboratory test of Liu et al [1995]. A definition sketch for the computational domain used for the simulation is shown in Figure 2. The outer circle shows the base of the island, which is centred at (x,y)=(13, 15) m and has a radius R=3.6 m; the middle dashed circle represents the initial still water shoreline (radius R=2.32 m); the inner circle represents the island top (radius R=1.1 m); the island height is 0.625 m.

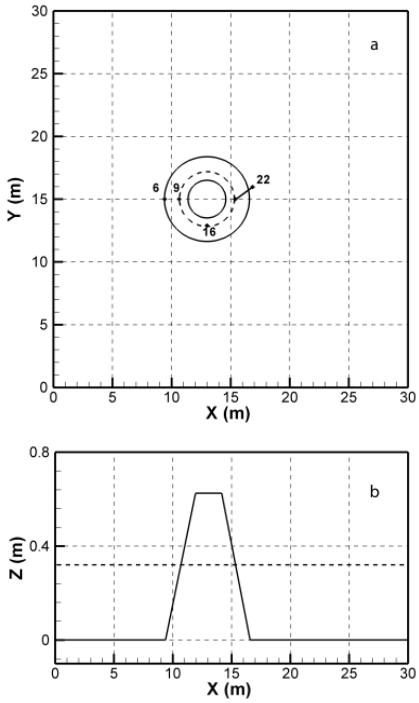

Figure 2 - Run-up of a solitary wave on a conical island. Schematic plot of the computational domain. a) Plane view. Outer circle: base of the island. Middle dashed circle: initial still water shoreline. Inner circle: island top. The dots represent measurement locations at 6: (x,y)=(9.4,15) m; 9: (10.4,15) m; 16: (13,12.42) m; 22: (15.6, 15) m. b) Cross section of the computational domain along the centreline (y=15 m). Dotted line: initial still water level.

As initial condition a rightward propagating solitary wave is imposed to the left boundary of the domain, on an otherwise calm free surface. The following expressions (Nikolos and Delis [2009]) are used for the free surface elevation η and the depth averaged velocity component u in the x direction:

$$\eta(t) = A\,sech^2\left[\sqrt{\frac{3A}{4h^3}}C(t-T)\right] \tag{76}$$

$$u(t) = \frac{C\eta(t)}{h+\eta(t)} \tag{77}$$

in which h is the still water depth, A is the amplitude of the incident wave, T is the time at which the wave crest enters the domain and $C = \sqrt{g(h + A)}$ is the wave celerity. In this paragraph the test case C of Liu et al (1995) is reproduced: h=0.32 m, A=0.064 m and T=2.45 s. The spatial discretization step is Δx=Δy=0.01 m, the time discretization step is Δt=0.005 s.

In Figure 3 the comparison between the maximum computed run-up around the island and that measured by Liu et al (1995) is shown. The computed values of the maximum run-up around the island are in good agreement with the experimental data. It can be noted that the run-up on the back side of the island, caused by the collision of edge waves circling the island from both sides, is well simulated by the present model.

In Figure 4 snapshots of the computed free surface elevation at four different instants of the simulation are shown. Figure 4.a shows how the wave front hits the forepart of the island. From Figure 4.a-b it is possible to observe the reflection and the diffraction phenomena around the island; Figure 4.d shows the runup on the backside of the island.

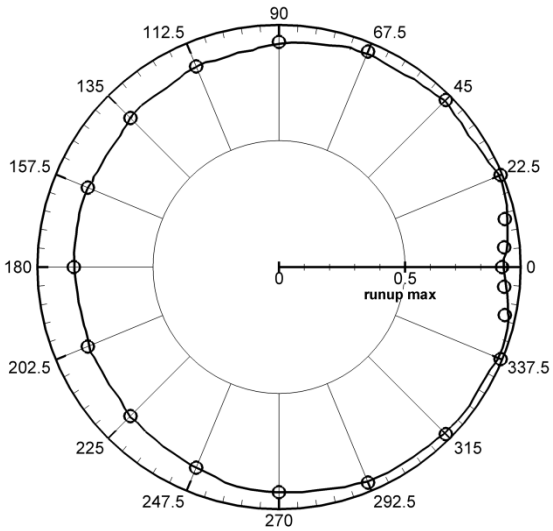

Figure 3 - Run-up of a solitary wave on a conical island. Maximum run-up around the conical island. Circles: measured data. Line: computed values.

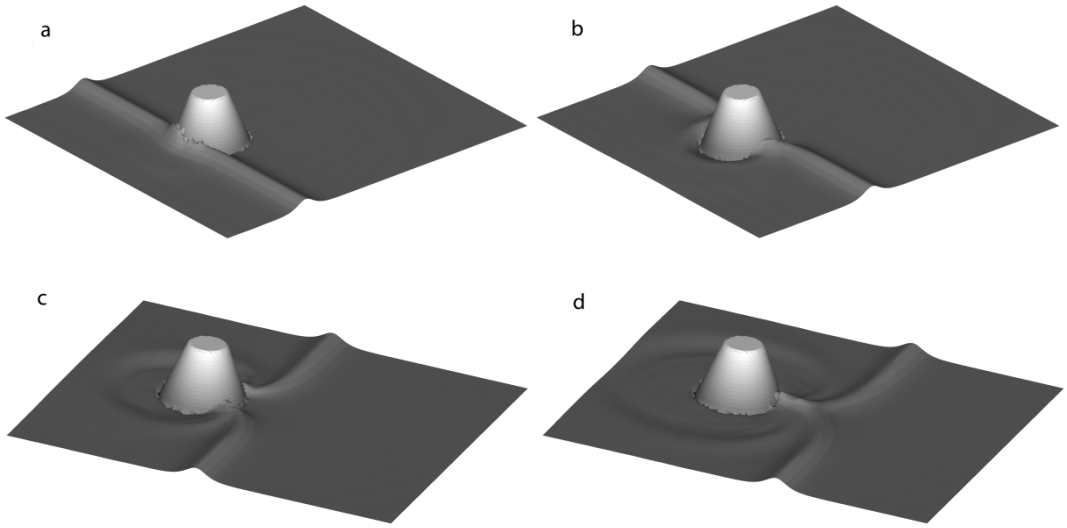

Figure 4 - Run-up of a solitary wave on a conical island. Snapshots of the computed free surface elevation at time t = 7.2 s (a), t = 9.7 s (b), t = 11.0 s (c), t = 12.2 s (d).

In Figure 5 the computed and measured time series from the measurement locations depicted in Figure 2 are shown. These four measurement locations have been chosen in order to represent the free surface elevation to the front, side, and rear of the island. From the comparison between the computed and measured values it can be seen that the proposed model is able to simulate the run-up at each measurement location around the island. Some secondary oscillation of the free surface elevation that has been observed during the laboratory experiments are slightly underestimated in the numerical simulation.

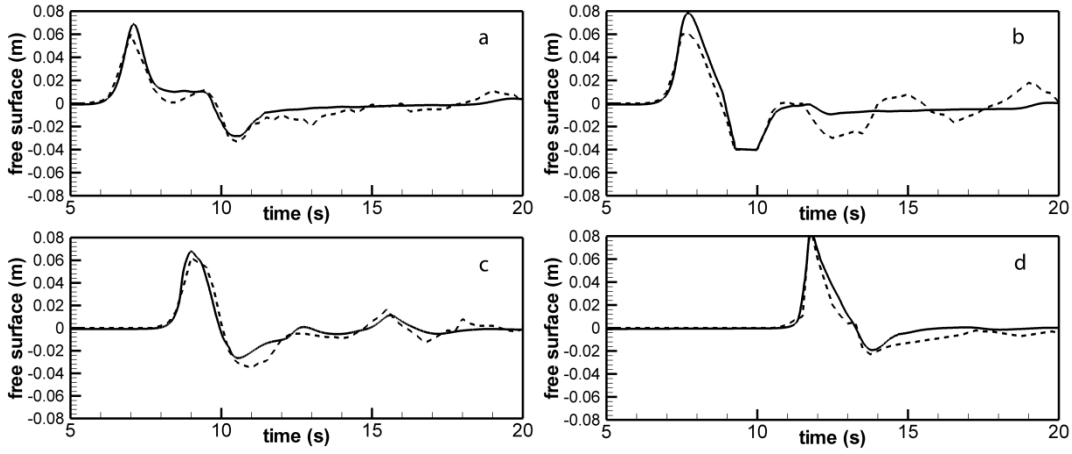

Figure 5 - Run-up of a solitary wave on a conical island. Time series from the measurement locations depicted in Figure 8: (a) 6, (b) 9, (c) 16, (d) 22. Full line: computed values. Dashed line: experimental data.

In Figure 6 a sequences of images that represent the evolution of a solitary wave on a conical island is shown. Figure 6.A shows the simulation of the wave run-up on the forepart of the island. In the further frames (Figure 6.B-C) is possible to observe the perfect reproduction of the diffraction phenomena and, as a consequence, the wave run-up on the lateral beaches. The last frame (Figure 6.D) shows that in the back side of the island the surface elevation caused by the collision of the two waves front is maximum.

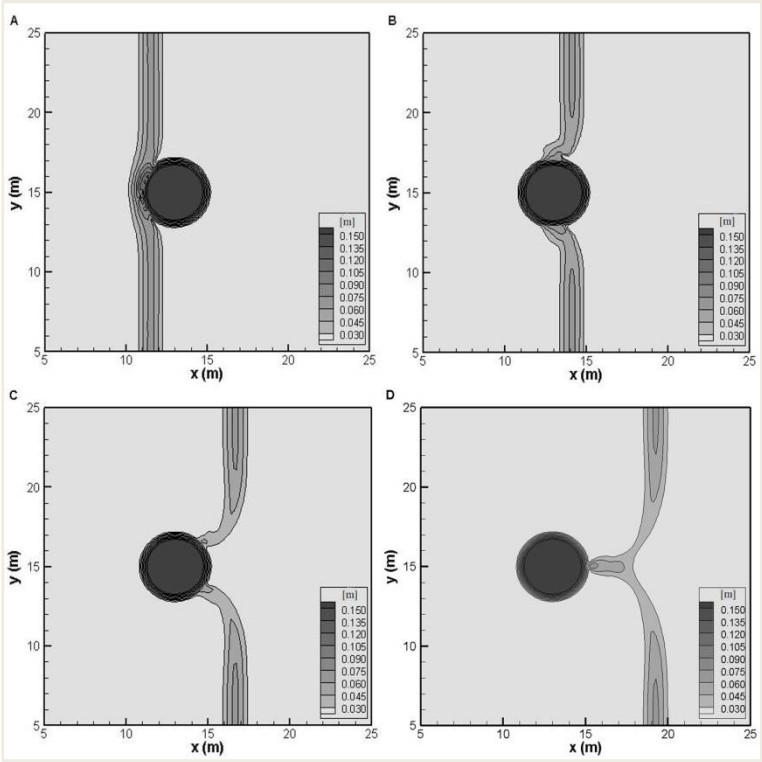

Figure 6 : Run-up of a solitary wave on a conical island. Surface elevation contour levels at time (A) t = 7.2 s, (B) t = 9.7 s, (C) t = 11.0 s, (D) t = 12.2 s.

The good agreement between the computed and observed values of the free surface elevation shows the ability of the proposed model to adequately simulate the large run-up heights produced by a tsunami wave on the lee side of small islands.

1.6.3. Longshore current simulation

In order to evaluate the ability of the proposed model to adequately represent the propagation of a wave train, wave breaking and wave induced longshore currents, we chose the case 4 in Visser's [1991] experiments. In the chosen case the physical model consists of a reservoir measuring 34 m x 16.6m. The slope of the smooth concrete beach is 1:20, which starts from an offshore water depth of 35 cm. The obliquely incident wave train has an amplitude of 7.8 cm, a period of T=1.02 s (μ=0.26 and ε=0.11) and an angle of incident of 15.4 ° in the offshore depth.

Visser's [1991] test case has the purpose of approximating a longshore current flow generated by a uniform wave field on a straight infinitely long and uniform beach. The above mentioned wave field has periodicity conditions in the coastline parallel direction: at each time step it is possible to notice that the same hydrodynamic conditions (free surface elevation and the value of the velocity component) are present at a certain distance. This distance is a function of the wave length and the angle of incidence between the wave front and the coastline parallel direction. In order to impose the above mentioned periodicity conditions, a computational domain with proper dimensions is chosen in the numerical simulation of this test case. To impose the periodic conditions on the southern and northern side, the width L_d of the computational domain (Figure 7a) is given by:

$$L_d = L_w / sin(\theta) = 5.6m \tag{78}$$

Where L_w represents the deep water wave length (about 1.34m) and θ is the angle of incidence between the line of the wave front and the coastline parallel direction and θ is equal to 15.4°.The length of the domain is equal to 12 m. The discretization of the computational domain is based on a grid defined by the coordinate Cartesian lines x and y and by the points of coordinates $x = i\Delta x$ and $y = j\Delta y$ (with i=1,..,N and j=1,...,M, in which N is the number of the calculation cells in the I direction, M is the number of the cells in the j direction) which represent the centre of the calculation cells. The computational grid resolution is Δx=0.03m, Δy=0.06m and with a discretization time step Δt=0.0034 s. The computational domain is divided into 3 zones (Figure7.a): 1) a generation zone ($i_a \leq i \leq i_b$) in which wave motion is internally generated following the Wei et al [1999] procedure (a wave train headed to the coastline and a wave train headed in the opposite direction); 2) a sponge zone ($1 \leq i < i_a$), placed on the western side of the computational domain, to absorb the wave motion energy directed towards the open sea and to avoid possible reflections on the western side of the computational domain; 3) a propagation zone ($i_b < i \leq N$), placed on the

eastern side of the generation zone, in which wave motion grows and propagates itself towards the coastline. In Figure 7.b the section (x-z) of the computational domain is shown.

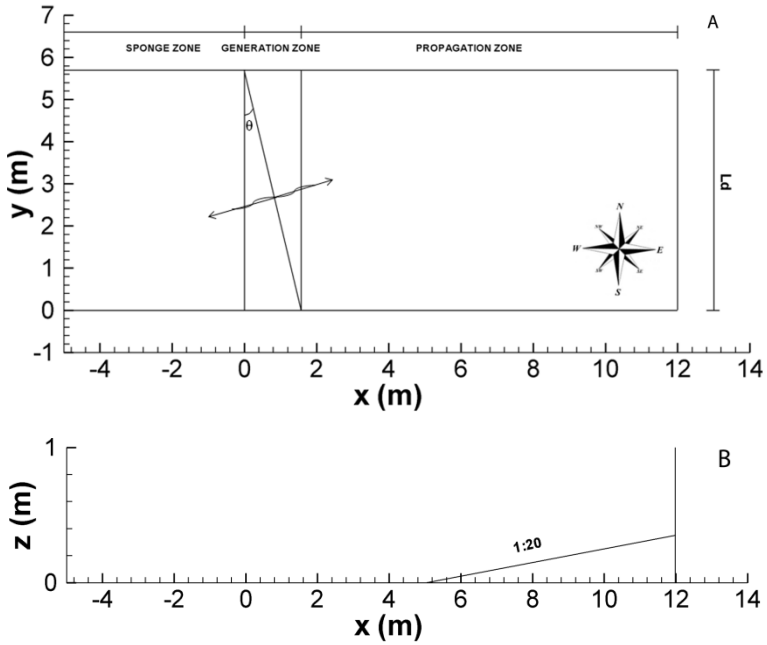

Figure 7 - Longshore current simulation test. Plan view (a) and section (b) of computational domain.

On the northern and the southern side of the propagation zone and the sponge zone, periodic conditions are realized: at each time step the same hydrodynamic conditions (free surface elevation and the value of the velocity component) are achieved. In fact the outgoing wave from the northern side has the same hydrodynamic characteristics as the incoming wave from the southern side. That makes it possible to assign the periodic boundary conditions. In order to do that two ghost points are used for each lateral side of the computational domain. Two ghost cells are defined adjacent to the southern boundary (j=0 and j=-1) and adjacent to the northern boundary (j=M+1 and j=M+2). Let $u_l(i,j)$, $H(i,j)$ be the value of the horizontal velocity in the two coordinate directions (with l=x,y) and the free surface elevation into the cell $I_{i;j}$. The periodic boundary conditions on the southern and northern side of the sponge zone and the propagation zone are given by:

$$u_l(i,0) = u_l(i,M); \quad u_l(i,-1) = u_l(i,M-1); \tag{79}$$

$$u_l(i,M+1) = u_l(i,1); \; u_l(i,M+2) = u_l(i,2); \tag{80}$$

$$H(i,0) = H(i,M); \quad H(i,-1) = H(i,M-1); \tag{81}$$

$$H(i,M+1) = H(i,1); \quad H(i,M+2) = H(i,2); \tag{82}$$

The application of the above mentioned conditions on the southern and northern side of the generation zone is incompatible with the internal generation. In fact the outgoing wave from the northern side of the generation zone does not have the same hydrodynamic characteristics as the outgoing wave from the southern side of the generation zone. In this zone there is an antisymmetric condition with respect to the two axes of symmetry (axis x' and axis y' in Figure 8): the outgoing wave from a southern boundary cell (marked by the letters A-B-C in Figure 8) has velocity values that are equal in module but opposite in direction with respect to the values of the outgoing wave from a northern boundary cell (marked by the same letters A'-B'-C' in Figure 8) placed in a symmetric position with respect to axis x' and axis y'). For this reason a particular boundary condition in the generation zone that uses the antisymmetry of the wave motion is applied. In fact in the point P'(i_b-i*,j) (where $0 \leq i^* \leq i_b - i_a$) the velocity values are equal in module but opposite in direction with respect to the velocity values of the point P(i_a+i*,M-j+1), while the values of the free surface elevation are the same. The antisymmetric boundary condition is implemented on the northern and southern side of the generation zone by using the following expressions:

$$u_l(i_s, 0) = -u_l(i, M-1); \quad u_l(i_s, -1) = -u_l(i, M); \tag{83}$$

$$u_l(i_s', M+1) = -u_l(i, 2); \quad u_l(i_s', M+2) = -u_l(i, 1); \tag{84}$$

$$H(i_s, 0) = H(i, M-1); \quad H(i_s, -1) = H(i, M); \tag{85}$$

$$H(i_s', M+1) = H(i, 2); \quad H(i_s', M+2) = H(i, 1); \tag{86}$$

where $i_s = i_b - i^* + 1$ and $i_s' = i_b - i^* - 1$.

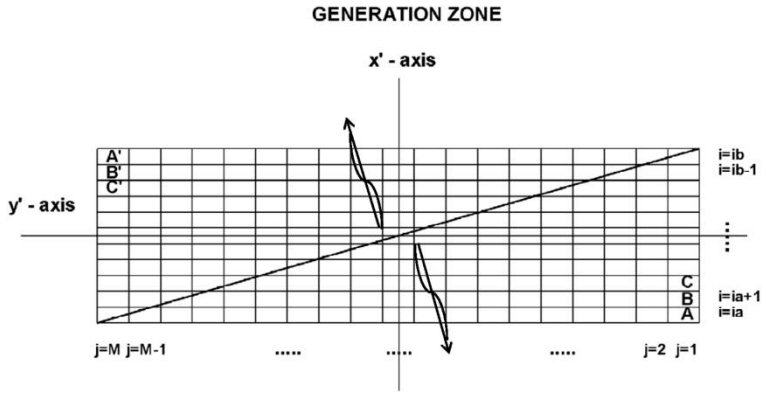

Figure 8 - Longshore current simulation test. Generation zone of computational domain.

The above mentioned boundary conditions in the generation zone avoid the outgoing wave from the southern side entering toward the northern side and overlaying itself on the wave motion directed to the propagation zone and vice versa. Using periodic boundary conditions in the propagation zone and the sponge zone and using the antisymmetric condition in the generation zone allows the simulation of the wave motion without any reflections from the northern and the southern side and allows the correct simulation of the longshore current.

Figure 9 shows the instantaneous wave field. It is possible to notice how the above mentioned boundary conditions does not produce spurious oscillations or nonphysical reflections.

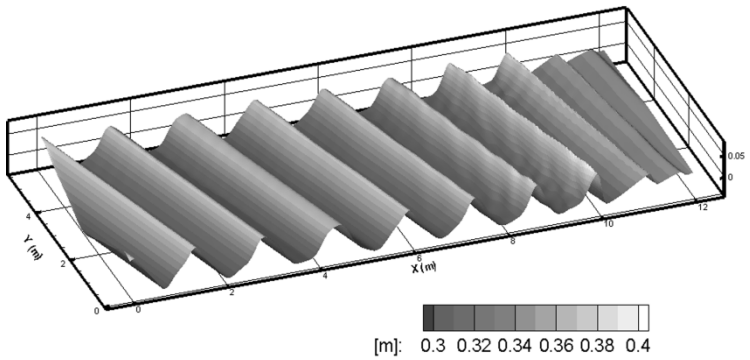

Figure 9 – Longshore current simulation test. A snapshot of the free surface elevation.

In Figures 10-11.a the results obtained by the proposed model are compared with the experimental data. In these figures the average values over time of the wave height, the longshore current and the free surface elevation are shown.

From the comparison between the experimental data and the simulation results, it is possible to see that the proposed model gives an adequate representation of wave transformation, shoaling and wave breaking. In Figures 10-11.a it is shown that the wave height, the wave setup and the longshore current obtained by the numerical simulation are in good agreement with the experimental data. Figure 11.b shows the nearshore currents induced by breaking, the incident angle of the wave front produces an uniform longshore currents and the nonzero value of setup cause a low value of cross-shore currents.

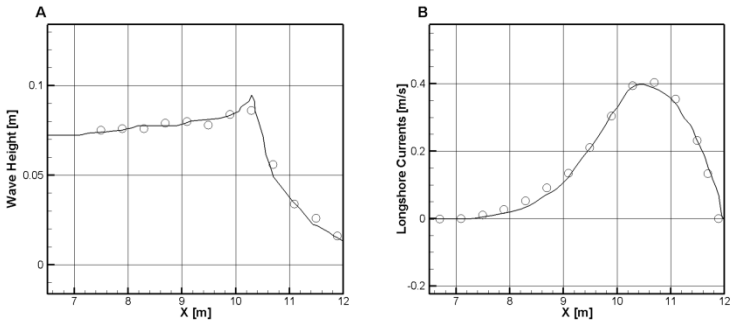

Figure 10 – Longshore current simulation test. A) wave height. B)longshore currents. Circles: experimental data. Continuous line: numerical results.

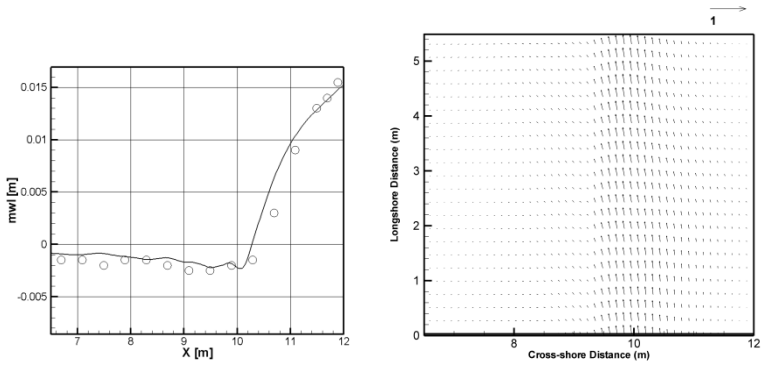

Figure 11 – Longshore current simulation test. A) Wave setup Circles: experimental data. Continuous line: numerical results. B) Nearshore currents induced by breaking.

1.6.4. Nearshore currents induced by submerged breakwaters

In this section, the ability of the proposed model is verified to represent the production of longshore and rip currents induced by the breaking of waves on a set of submerged bars and the interaction of these currents with the wave motion. The numerical results obtained with the proposed model are compared with measurements taken by Haller et al. [2002] who carried out laboratory experiments in a wave basin in order to study the coastal circulations induced by the propagation of monochromatic waves on a sloping planar beach on which a set of shore parallel submerged bars was located.

The size of the basin was 17.2m x 18.2m. The bottom geometry consisted of a planar beach with a 1:30 slope on which three submerged barriers with an approximately parabolic shape and spaced at 1.82m were located. Figure 12 shows a plan view and a cross section of the wave basin.

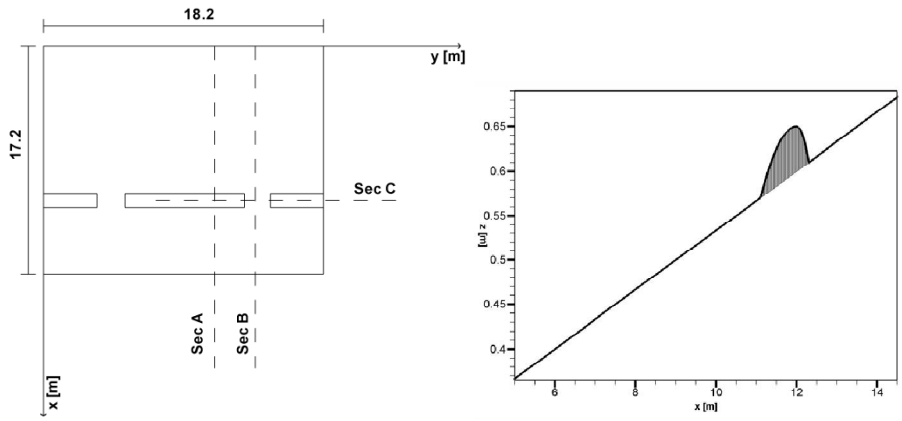

Figure 12 – Nearshore currents induced by submerged breakwaters.
Plan view and section of wave basin used by Haller et al. [2002].

The test concerns the simulation of the propagation of a monochromatic wave of amplitude a=5.12cm and period T=1s (μ=0.45 and ε=0.073). In the numerical simulations the waves are internally generated and a wide absorbing layer is set behind the generation zone. Reflective conditions are set for the lateral boundaries. The simulation has been realized with the proposed model, in which the computational grid resolution is Δx=0.025 m and Δy=0.05 m. The time step is 0.005 s.

The presence of the submerged bars results in the breaking of waves over them because of the reduced water depth; the gradients in the mean water elevation related to the breaking of the waves drive longshore currents into the area between the bars and the coastline and rip currents flowing offshore ward through the gaps.

Figure 13 shows a detailed view of the instantaneous free surface elevation at one of the gaps between the submerged bars. It can be noted that, at the gap location, the waves increase their height as a result of the interaction between the rip current flowing offshore ward and the waves propagating in the opposite direction. In the area between the bars and the coastline the wave motion is attenuated because of the wave energy dissipation related to the breaking of waves over the bars.

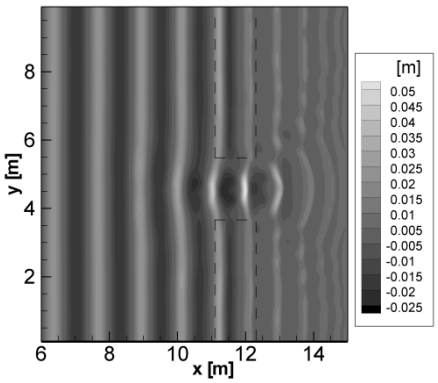

Figure 13 – Nearshore currents induced by submerged breakwaters.
Instantaneous elevation of free water level related to still water level.

The time-average velocity field is shown in Figure 14: only one vector out of four is shown in the figure. The breaking of waves over the submerged bars and close to the shoreline results in a local increase of the mean water level. Different values of the breaking induced wave set-up cause gradients in mean water level elevation which produce two opposite vortexes in the area between the bars and the coastline. At the gaps between the bars, rip currents flowing offshore ward occur for continuity.

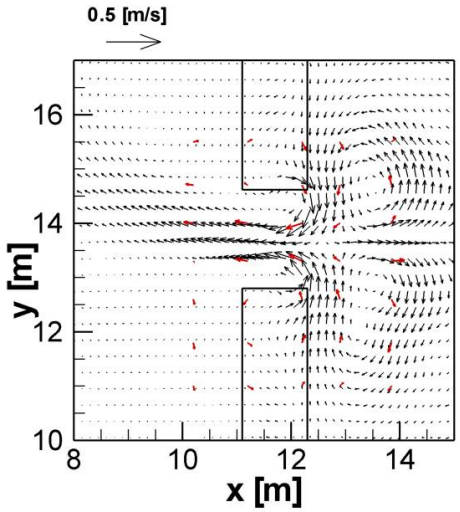

Figure 14 – Nearshore currents induced by submerged breakwaters. Time averaged velocity fields.

Black vector: computed values. Red vector: experimental data. A vector out of four is represented.

Figure 15 shows the comparison between the calculated and measured averaged wave heights along two cross-sections: one crossing the central bar at y=11.23 m (Sec. A in Figure 12) and one crossing the gap between the bars at y=13.68m (Sec. B in Figure 12).

Referring to Figure 15a it can be seen that the presence of the bars, located between x=11.1m and x=12.3 m, induces the breaking of the waves on top of them. The numerical results are in good agreement with the experimental data both in the shoaling region previous to the breaking and in the area between the bars and the coastline. In this area the wave breaking ceases just shoreward of the bars as a result of the increased water depth; the waves, attenuated because of the energy dissipation related to the breaking of waves over the bars, continue their propagation toward the shore in the proximity of which they break again.

Figure 15b shows the comparison between the time averaged wave heights calculated by the present model along the section crossing the gap between the bars (Sec. B in Figure 12). Along this section the breaking of the waves occurs as a result of the combined action of the reduced water depth and the rip current that, opposing the wave propagation, makes the waves steeper. The good agreement between the calculated and measured values shows the actual ability of the model to adequately represent the wave-current interaction phenomena.

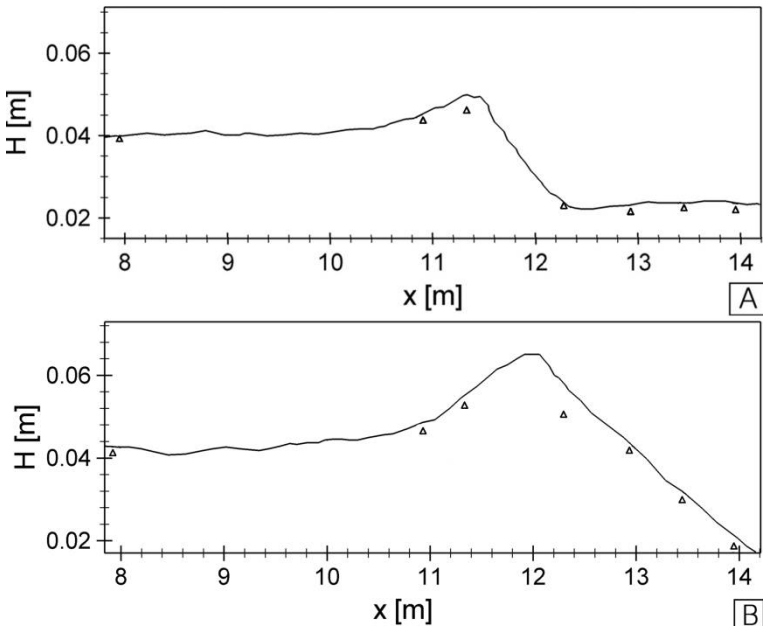

Figure 15 – Nearshore currents induced by submerged breakwaters.
Wave heights along two transversal sections: A) y=11.23 m section; B) y=13.68 m section.

Comparison between numerical results (continuous line) and experimental results (circles).

Figure 16 shows the comparison between the calculated and measured values of the mean water level along two cross-sections: section A and B shown in Figure12.

Looking at Figure 16a, relative to section A, it can be noted that in the area between the bars and the coastline, x>12.3m, the mean water level remains approximately constant because of the action of containment carried out by the set of bars.

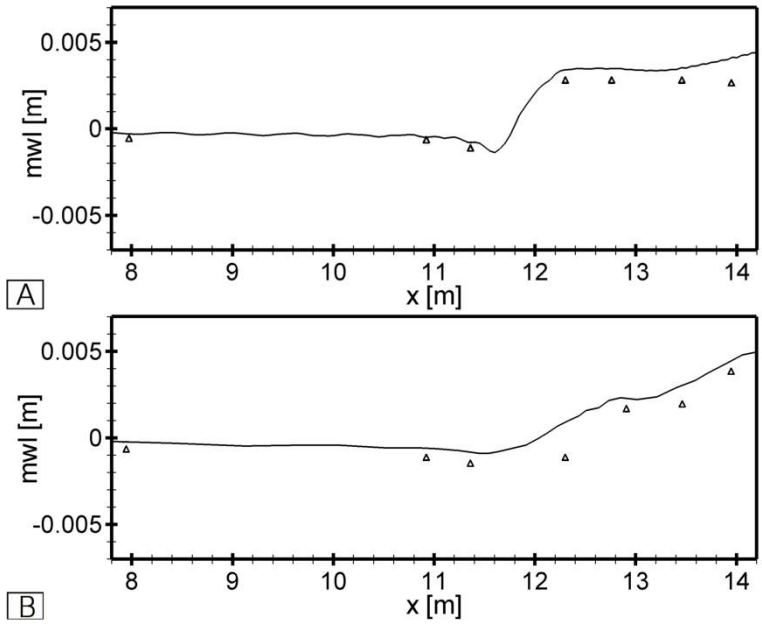

Figure 16 – Nearshore currents induced by submerged breakwaters.

Free average surface elevation compared to still water level: A) y=11.23 m section; B) y=13.68 m section. Comparison between numerical results (continuous line) and experimental results (circles).

Figure 17 shows the variation of the cross-shore volume flux along a longshore transect located at x=12.08 m (Section C in Figure 12). The breaking induced circulation patterns in the area are characterised by a shoreward directed flow occurring over the bars and an offshore oriented current occurring at the gaps between the bars. In Figure 17 it can be seen how this behaviour is well represented by the proposed model.

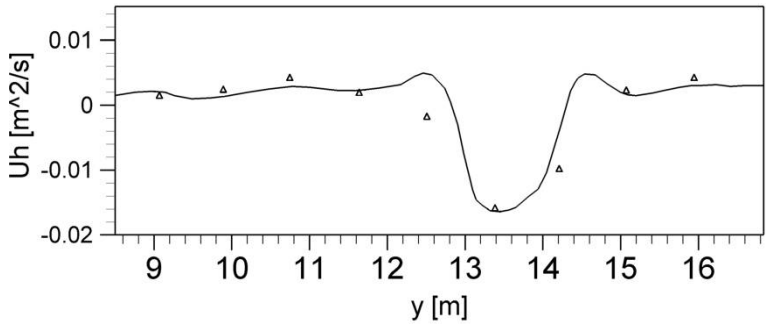

Figure 17 – Nearshore currents induced by submerged breakwaters.

Volumetric cross flow (UH). Section x=12.08m

1.6.5. C-Property Test

Motion laws admit stationary solutions in which the source terms are perfectly balanced by flux terms. A numerical scheme is said to be well-balanced and to satisfy the C-Property if it exactly preserves these steady state solutions.

In the momentum balance Equation (27) the surface gradient term is decomposed according to Equation (22). In the case of the numerical integration of Equation (27) on Cartesian grids, the above decomposition allows the balancing between the numerical discretization of the term related to the gradient of the square of the total local depth and the numerical source term discretization related to the bed slope (that allows the numerical scheme to satisfy the C-property). However the above decomposition introduces, in the contravariant form of the momentum balance Equation (31), new terms in which covariant derivatives are present; these covariant derivatives determine the onset of Christoffel symbols.

The numerical discretization of these symbols and the failure to numerically satisfy the metric identities, in the numerical integration of the motion equation, on highly distorted grids, produces errors that do not allow the numerical scheme to satisfy the C-Property.

In order to verify the C-Property of the numerical scheme, a test is run to numerically simulate a still water state on non-uniform beds, on a highly distorted curvilinear grid. The aforementioned test (Xing and Shu [2006]) consists in the simulation of the still water state in a square domain measuring 1 m x 1 m, whose bottom consists of a hump, shown in Figure 18a that is mathematically represented by

$$b(x,y) = 0.8\exp(-50((x-0.5)^2 + (y-0.5)^2)) \qquad x,y\in[0,1] \tag{87}$$

The initial water level is H(x,y,t0)=1-b(x,y), that is, a still water state. A highly distorted curvilinear grid is used, shown in Figure 18b, made up of 100x100 computational cells. In this test closed and reflective boundary conditions are implemented.

Let BEFCH be the model obtained by applying the numerical scheme presented in section 3 to Equations (29) and (31) in which Christoffel symbols are present and terms (71-72-73) (section 2.5) are introduced, in order to numerically satisfy the metric identities. Let BENF be the model obtained by applying the scheme proposed in section 3 to Equations (36) and (38) in which Christoffel symbols are absent and terms (71-72-73) are not introduced. Le BEF be indicates the model obtained by applying the scheme proposed in section 3 to Equations (36) and (38) in which Christoffel symbols are absent and terms (71-72-73) are introduced , in order to numerically satisfy

the metric identities. The comparison of the results is carried out by using the Root Mean Square (RMS), calculated as

$$\sigma = \sqrt{\frac{\sum_{i,j=1}^{N,M}(A_{i,j}^{n} - \tilde{A}_{i,j}^{n})^2}{NM}} \tag{88}$$

in which, n is the time instant, N is the number of the calculation cells in the *i* direction, *M* is the number of the cells in the *j* direction, $A_{i,j}^{n}$ is the value of the generic quantity obtained by the numerical simulation, while $\tilde{A}_{i,j}^{n}$ is the value of the same quantity calculated by experimenting results or analytical solutions.

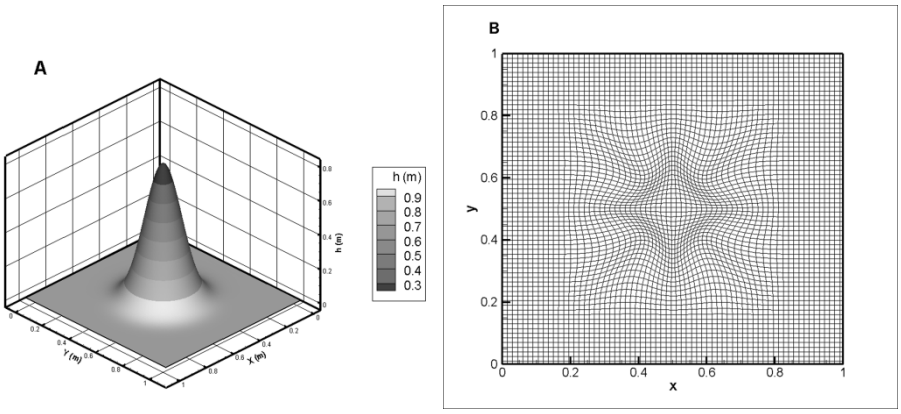

Figure 18 – C-Property test. A) Bottom. B) Computational grid.

In Figure 19a-b are represented the free surface elevation and the velocity field calculated by the BEFCH model. Figure 13a-b shows that the free surface does not remain flat and that the velocity is not equal to zero.

The Root Mean Square σ_1, calculated by using Equation (88), of the difference between the values obtained by the BEFCH model and the null values of the quantities η, HU_x and HU_y of the still water state, are used as the indicators of the numerical error produced by the simulations and are shown in Table 1.

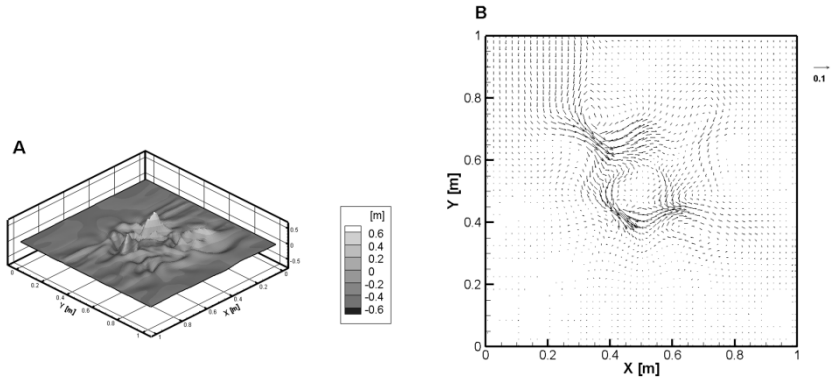

Figure 19 – C-Property test. A) A snapshot of the free surface elevation.
B) Snap shot of the velocity field. A vector out of four is represented. Results obtained by the BEFCH Model.

	η	HU_x	HU_y
σ^1	2.36 E-004	2.13 E-004	2.72 E-004

Table 1 – C-Property test. Root mean square σ^1 of η, HU_x, HU_y obtained by the BEFCH Model.

Figure 20a-b shows the free surface elevation and the velocity field calculated by the BENF model. It can be seen from Figure 20a-b that the free surface elevation presents oscillations especially in the maximum distortion area and that velocity is not null.

Table 2 shows the Root Mean Square $\sigma_1$values of the differences between the values obtained by the BENF model and the null values of the quantities η, HU_x and HU_y of the still water state. In this table it can be seen how the Root Mean Square σ_1 are some order of magnitude lower than in the previous case, but still not negligible.

Figure 19a-b and 20a-b prove that the errors produced by the numerical discretization of the Christoffel symbols, which arise from the decomposition of the surface gradient term present in Equation (22), and the errors produced by the failure to numerically satisfy the metric identities, do not allow the balance between the numerical discretization of the terms related to the gradient of the square of the total local depth and the numerical discretization of the source term related to the bed slope (i.e.do not allow the numerical scheme to satisfy the C-property).

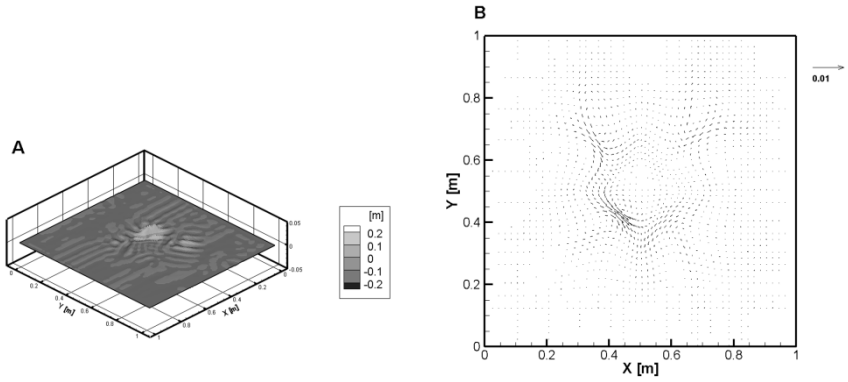

Figure 20 – C-Property test. A) A snap shot of the free surface elevation; B) A snap shot of the velocity field. A vector out of four is represented. Results obtained by the BENF Model.

	η	HU_x	HU_y
σ^1	3.44 E-006	3.63 E-006	4.44 E-006

Table 2. C-Property test. Root mean square σ^1 of η, HU_x, HU_yobtained by the BENF Model.

Figure 21a-b shows the free surface elevation and the velocity field calculated by the BEF model. From the figure it can be seen that the free surface remains flat and velocities are practical equal to zero.

Table 3 shows the Root Mean Squares σ_1 of the difference between the values obtained by the BEF model and the null values of the quantities η, HU_x and HU_y of the still water state. In this table it is seen that the Root Mean Squares σ_1 are of the same order of magnitude as the computer truncation order in double precision.

Figure 21a-b shows that the integral form of the contravariant Fully Non linear Boussinesq Equations (Equations (36) and (38)) in which Christoffel symbols are absent, resolved with the scheme presented in Section 3, and with the addition of terms (71-72-73) in section 2.5, which can numerically satisfy the metric identities (BEF model), is "well balanced", i.e. it satisfies the C-Property even on highly distorted grids.

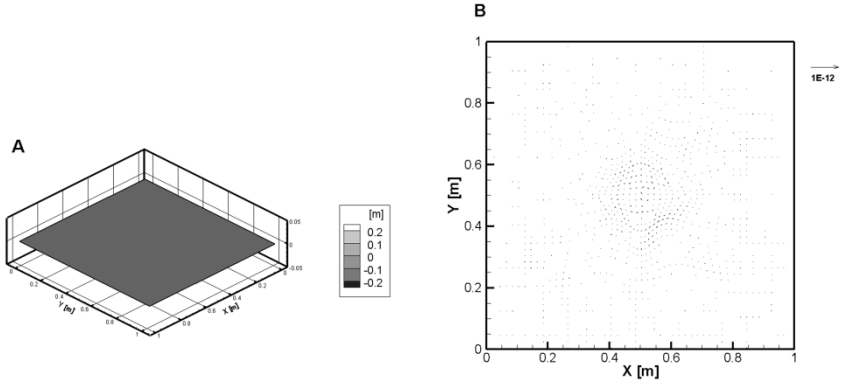

Figure 21 – C-Property test. A) A snap shot of the free surface elevation; B) A snap shot of the velocity field. A vector out of four is represented. Results obtained by the BEF Model.

	η	HU_x	HU_y
σ^1	1.24 E-017	1.12 E-016	1.46 E-016

Table 3 – C-Property test. Root mean square σ^1 of η, HU_x, HU_yobtained by the BEF Model.

1.6.6. Conservation wave form on a flat bed

This section demonstrated the ability of the proposed BEF model to simulate the propagation of a sinusoidal wave train on a flat bed on a highly distorted computational grid. The test case presented in this section consists in the propagation of a wave train, whose amplitude and period are, respectively, 6 cm and 1.25s (μ=0.35 and ε=0.07), on a 30m long and 15m wide channel, with a flat bottom and a 50cm initial depth. The time discretization is 0.004s; the spatial discretization is Δx=0.1m, Δy=0.15m in the Cartesian zone; at the centre of the computational domain a region with highly distorted computational cells is inserted, as shown in Figure 22. In this test periodic boundary condition on the computational domain lateral sides, are implemented a sponge layer has been added upstream and downstream. The wave is internally generated at the x=0 m and the simulated time interval is equal to 100s.

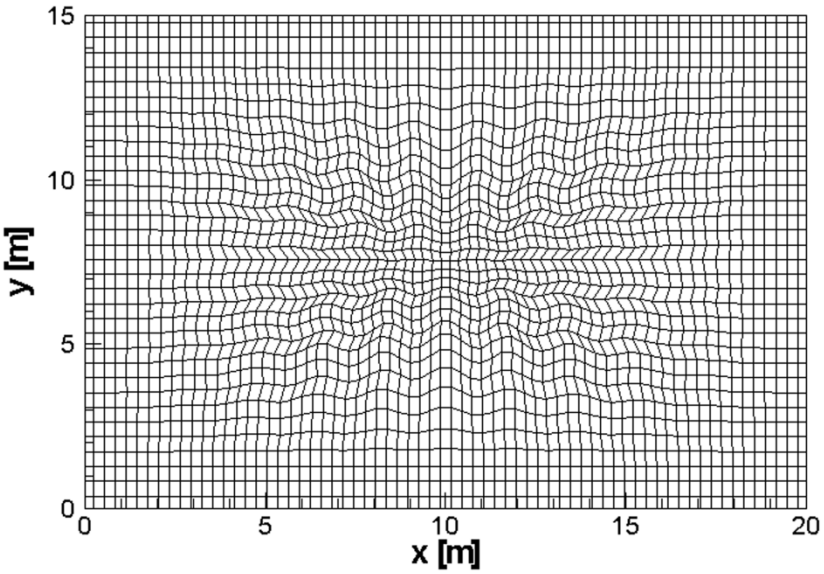

Figure 22 – Conservation wave form test on a flat bottom. Grid distortion. A coordinate line out of two is represented.

The above mentioned test is done by applying the proposed model (BEF), the BEFCH model and the BENF model. As already described, the BEFCH model differs from the proposed one just because of the presence of the Christoffel symbols in the governing equations; the BENF model differs from the proposed one just because of the absence of terms designed to numerically satisfy metric identity.

Figure 23 shows the instantaneous free surface elevation obtained by the BEFCH model. From this figure it can be seen that the wave form is not preserved, owing to the fact that the discretization of

the Christoffel symbols in Equation (31) produces errors that are of the same order of magnitude as the dispersive terms: therefore this model does not allow the preservation of the wave form on a flat bottom on a highly distorted grid.

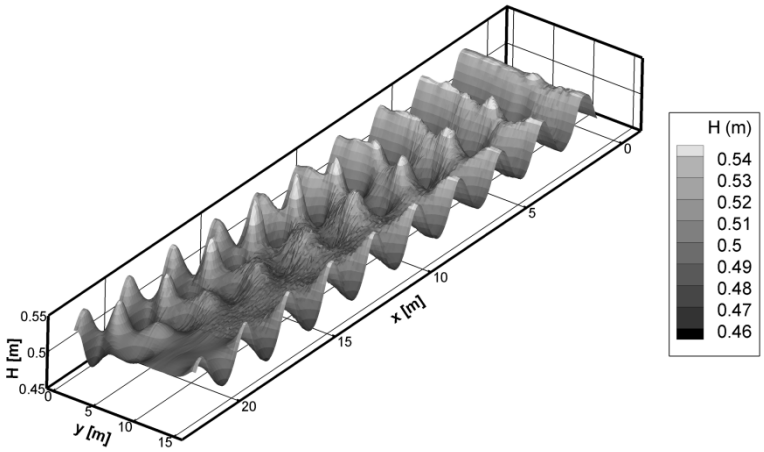

Figure 23 – Conservation wave form test on a flat bottom. Wave field. Results obtained by the BEFCH Model.

Figure 24 shows the instantaneous free surface elevation obtained by using the BENF model. The effects produced by the failure to numerically satisfy the metric identities are evident in the solution, in the region of maximum distortion of the grid.

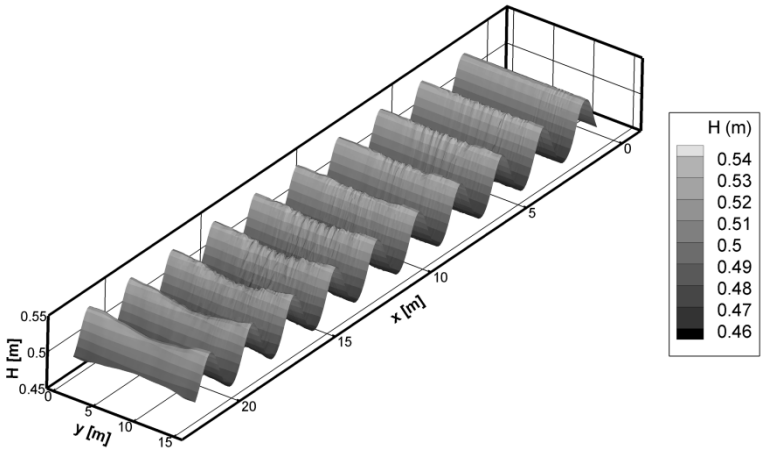

Figure 24 – Conservation wave form test on a flat bottom. Wave field. Results obtained by the BENF Model.

Figure 25 shows the instantaneous free surface elevation obtained by the BEF model. From this figure it can be seen that the wave form is preserved and is not affected by alterations that could

disturb the wave profile; no significant spurious oscillations are present in the region of maximum distortion of the grid.

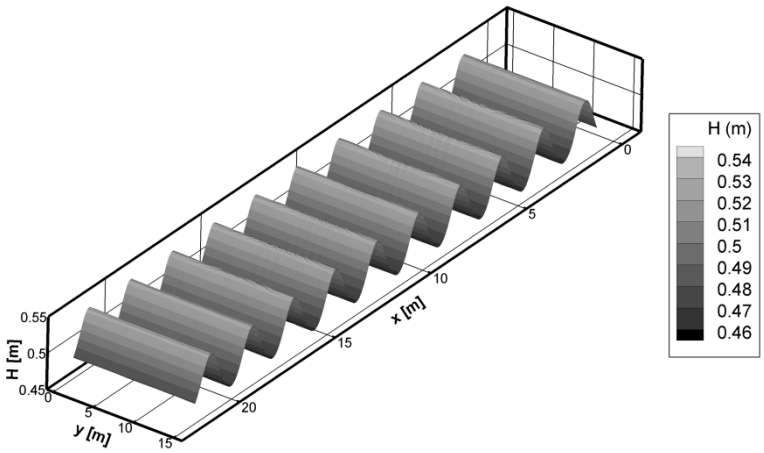

Figure 25 – Conservation wave form test on a flat bottom. Wave field. Results obtained by the BEF Model.

Since the wave propagation takes place in the direction parallel to the x axis, the numerical values of U_y, which should be null, represent a measure of the error produced in the numerical simulations of this test case. Table 4 shows the Root Mean Square σ_2 of the errors in the velocity component U_y obtained by the BEF, BEFCH and BENF models. The table shows that the numerical satisfaction of the metric identities and the elimination of the Christoffel symbols from the motion equations greatly reduces the numerical errors.

Figure 26 shows the instantaneous free surface elevations along a stream wise section located at the centre of the channel obtained by the BEF, BEFCH and BENF models, which are compared with the wave profile obtained by the analytical solution. From this figure it is possible to see that the solution obtained by the proposed BEF model is in very good agreement with the analytical solution, even in the maximum grid distortion region. The position of the wave peaks and troughs obtained by the model in which there are no terms designed to numerically satisfy metric identities (BENF model) agree reasonably well with the analytical ones, but the solution obtained by this model is affected by the distortion of the grid: from x=12m the wave profile obtained by the BENF model begins to change and the wave amplitude is not maintained. The solution obtained by the model in which are discretized the equations containing Christoffel Symbols (BEFCH model) is soon affected by the grid distortion; the wave form changes significantly and the position of the wave peaks and troughs are wrong, compared with the analytical solutions.

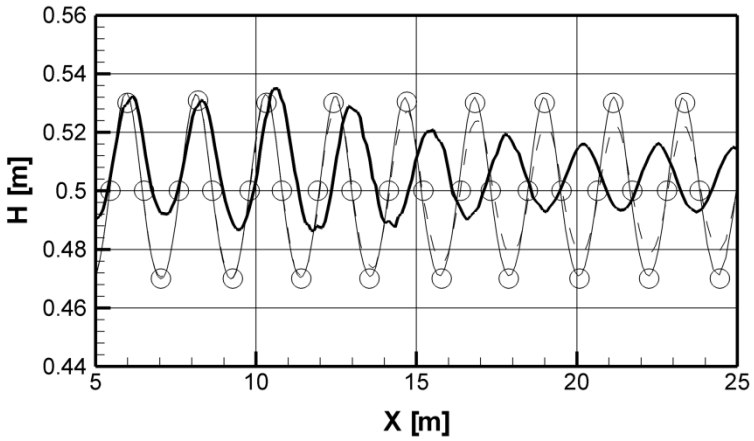

Figure 26 – Conservation wave form test on a flat bottom. Wave profile.
Circles: analytical solution. Fine continuous line: BEF model. Dotted line: BENF model. Thick line: BEFCH model.

The comparison of the results shown in this section demonstrates that the proposed BEF model is able to simulate the wave form conservation on a flat bottom on highly distorted grids. The errors due to the discretization of the Christoffel symbols and the errors due to the failure to numerically satisfy the metric identities are of the same order of magnitude as the dispersive terms in the Fully Non Linear Boussinesq Equations and compromise the ability of the numerical scheme to simulate the wave propagation on a flat bottom.

Table 4 – Conservation wave form test on a flat bottom. Root mean square σ^1 of theU_y velocity.

	BEF	BEFCH	BENF
σ^2	1.32 E-005	3.23 E-03	5.25 E-004

1.6.7. Wave train propagation on a varying depth

In this section the ability of the proposed model to represent the shoaling and the wave breaking is tested. The results of the numerical simulations obtained by the model presented in this paragraph are compared with experimental data from laboratory tests performed by Stive [1980] for breaking waves on a sloping beach.

The experiments were conducted in a 55m long wave flume. The waves were generated at one end of the wave flume at a constant depth of 0.85 m and they propagated over a planar beach with a slope of 1:40 located at 16 m from the wave generator.

The amplitude and the period of the reproduced wave are respectively, 0.156 m and 1.79 s,(μ=0.26 and ε=0.18). consistently with Stive [1980]. The spatial discretization step is Δx=0.01 m, whereas the time discretization step is Δt=0.0015 s. In this test closed and reflective boundary conditions, on the computational domain lateral sides, are implemented.

The bottom of the flume is shown in Figure 27a. The computational curvilinear highly distorted grid used to numerically reproduce this test case is shown in Figure 27b.

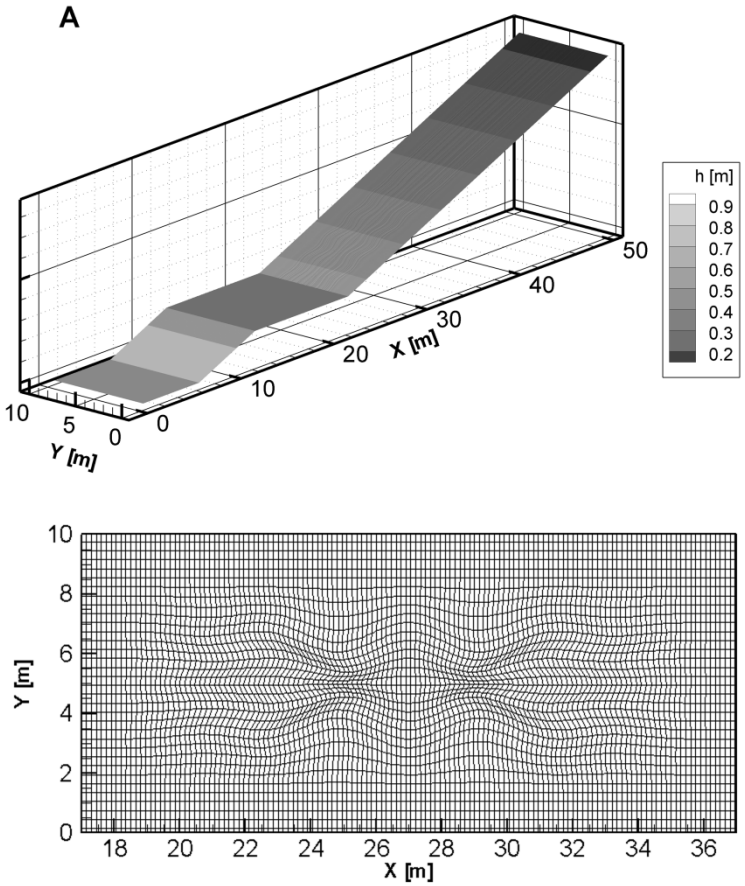

Figure 27 – Wave train propagation on varying depths. A) Seabed bottom. B) Grid distortion.

Let OBEF be the model obtained by applying the shock-capturing scheme proposed in Gallerano et al. [2014], in which a "dimension by dimension" WENO reconstruction procedure is used, to the integral form of the contravariant FNBE proposed in Gallerano et al. [2014], in which the continuity equation presents a dispersive term and the momentum balance equation does not include the Christoffel symbols. Let BEFW1D be the model obtained by applying the shock-capturing scheme proposed in Gallerano et al. [2014], in which a "dimension by dimension" WENO reconstruction procedure is used, to Equations (36) and (38) of the present work, in which the continuity equation does not present any dispersive term. In both the BEW1D and OBEF models the terms (71-72-73) (section 2.5) are introduced in order to numerically satisfy the metric identities. The above mentioned test is done by applying the proposed model (BEF), the BEFCH model, the BEW1D model and the OBEF model.

Figure 28 shows the free surface elevation at t = 70s obtained by the proposed BEF model. The figure shows the ability of the model to represent the wave shoaling and the steep front of the breaking wave, without significant disturbances in the solution. Figure 29 shows the free surface elevation at t = 70s obtained by the BEFCH model in which the Christoffel symbols are present. From this figure it can be seen that, in the region where the calculation cells are distorted, the spurious oscillations of the same order of magnitude as the wave amplitude are produced in the solution; these spurious oscillations do not make it possible to adequately represent the wave form and the front of the breaking wave.

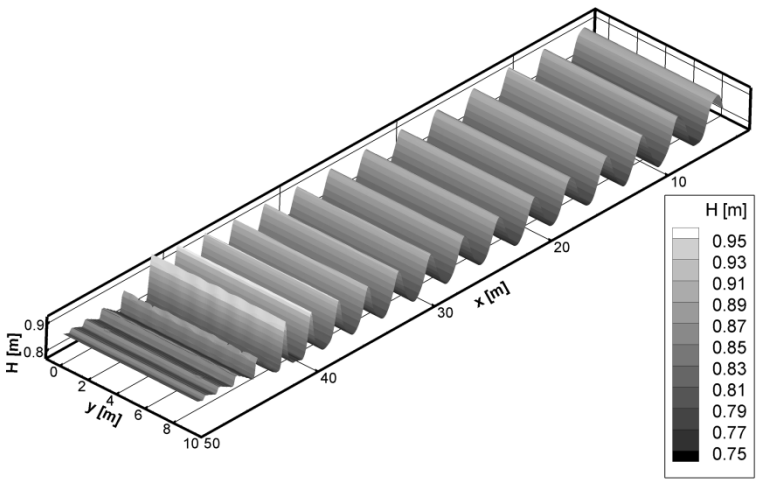

Figure 28 – Wave train propagation on varying depths. Instantaneous wave field. BEF model.

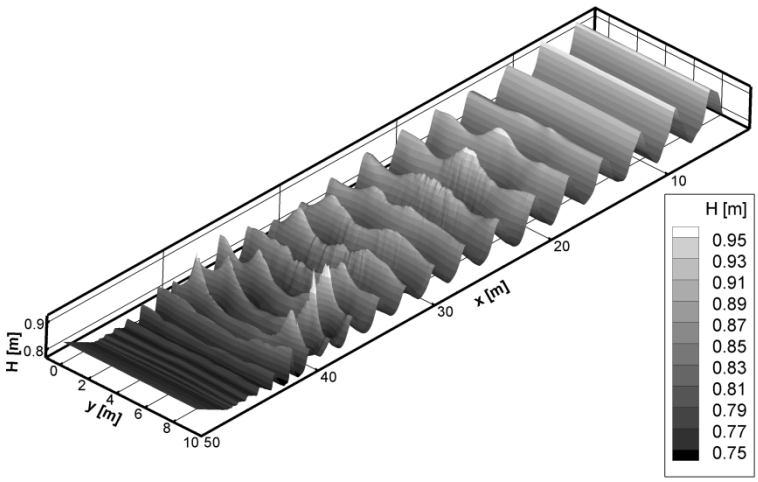

Figure 29 – Wave train propagation on varying depths. Instantaneous wave field. BEFCH model.

Figure 30a shows the comparison between the time averaged wave height obtained by the BEF, OBEF and BEFW1D models and the experimental values. Figure 30b shows the comparison between the time averaged free surface elevation obtained by the BEF, OBEF and BEFW1D models and the experimental values. Table 5 shows the root mean square, σ_w, of the difference between the values of the wave height obtained from the simulations and the corresponding experimental data, and the root mean square, σ_s, of the difference between the free surface elevation obtained by the simulations and the experimental data. In this table is also shown the root mean square, σ^3, of the difference between the values obtained by the simulations and the null values of the quantity U_y, which can be considered a measure of the error produced by the numerical simulation, since the direction of propagation of the wave train is parallel to the x axis.

From Figure 30a-b it can be seen that the OBEF model does not adequately represent the steepening of the wave front just before the breaking region, slightly overestimating the set-down and underestimating the set-up. From the same figures, and from Table 5 it can be seen that the results obtained by the BEFW1D model are more accurate than those obtained by the OBEF model. Compared to the OBEF model this improvement in the results is due to the absence of the dispersive term in the continuity equation.

Figure 30a-b shows that the wave height and the free surface elevation obtained by the proposed BEF model are in good agreement with the experimental data, in the deep water region as well as in the wave breaking region. From the comparison between the numerical results obtained by the proposed BEF model and those obtained by the BEFW1D model, we deduce that the genuinely 2D WENO reconstructions used in the proposed BEF model introduce lower numerical dissipation in the solution, allowing a better representation of the shoaling phenomena, wave height decay due to wave breaking, wave setup and setdown.

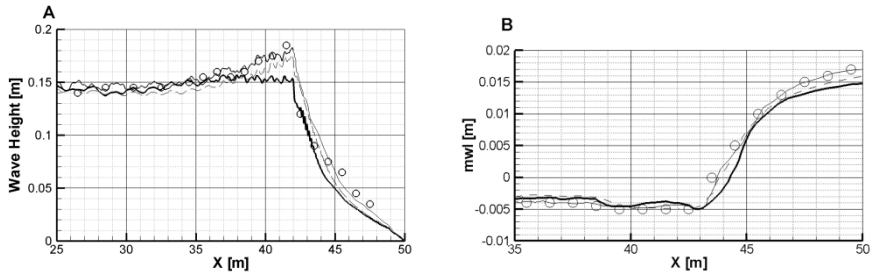

Figure 30 – Wave train propagation on varying depths. A) Average wave height. B) Free surface elevation related to still water level in time averaged. Circles: experimental data. Thick continuous line: OBEF model. Dotted line: BEFW1D model. Fine continuous line: BEF model.

	σ^3	σ_w	σ_s
OBEF	3.81 E-005	0.2090	0.2095
BEFW1D	3.53 E-005	0.2051	0.2054
BEF	3.35 E-005	0.1926	0.1948

Table 5 – Wave train propagation on varying depths. Root mean square of U_y velocity component (σ^3). Root mean square of average wave height (σ_w). Root mean square of free surface related to still water level (σ_s).

1.6.8. Simulation of wave train propagation on a highly distorted grid

The Fully Non-linear Boussinesq Equations (FNBE) proposed by Wei et al [1995] and Chen et al [2003] represent the evolution of the previous Boussinesq models because improved the dispersive characteristics of the equations retaining terms up to $O(\mu^2)$ in the depth averaged velocity and using as dependent variable of the equations the horizontal velocity from a certain depth. Furthermore the FNBE improve the non linear properties of the equation retaining terms up to $O(\varepsilon^3\mu^2)$, these terms represents the non linear effects in dispersion terms. Retaining these terms in the Boussinesq Equations let to improved the model capability on representing the steepening wave profile just seaward of the surf zone. Then Wei et al [1995] demonstrate that FNBE extend a lot the validity envelope of the equations about dispersion and nonlinearities.

From a theoretical point of view, Wei et al [1995] underline that Standard Boussinesq Equations (SBE) have a very strictly range of validity: the SBE are based on the assumption that $\varepsilon,\mu \ll 1$ and $\varepsilon/\mu=O(1)$, after which terms of $O(\mu^4, \varepsilon\mu^2, \varepsilon^2)$ are neglected. Assuming that the validity limit for the standard approximation corresponds approximately to $\varepsilon=\mu^2=0.2$, the value of $\varepsilon\mu^2$ is around 0.04 (as shown in Figure 1 of Wei et al [1995]); the fully non linear model extend the validity envelope of the Boussinesq model since the curve $\varepsilon\mu^4=0.04$.

In this thesis a conservative and contravariant form of Fully Non linear Boussinesq Equations, in which terms up to $O(\varepsilon^3\mu^2)$ and second order vertical vorticity terms are included, is presented.

In this section we demonstrate that the proposed conservative and contravariant form of FNBE, integrated with the proposed numerical scheme, is able to simulate waves with high non linearities ($\varepsilon=0.65$) also on curvilinear highly distorted grids.

In order to demonstrate the model capability to correctly simulate the propagation of strongly dispersive and highly nonlinear wave train on curvilinear highly distorted grid, we choose to simulate three wave train with different characteristics by using a calculation grid with the highly distorted zone shown in Fig 31. Two sponge zones are laterally situated to correctly dissipate the wave energy. In order to analyze if the wave profile shows any deformation during the simulation, a flat bottom, situate at 0.85m from the still water level, is used.

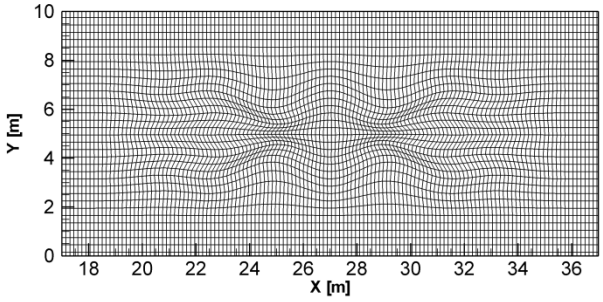

Figure 31. Simulation of wave train propagation on a highly distorted grid. Grid distortion.

The first wave train (A) has an amplitude of a=0.17m, a period of T=0.87s, a non linearity of ε=0.2 and a strong dispersion of μ^2=0.5. In Figure 32 is shown the wave profile after 50s of simulation. It is possible to notice how the proposed model can correctly represent the high dispersion of the wave train: the profile doesn't present any disturbs or modification of the wave characteristic and it is in good agreement with the data extrapolated from the analytical solution. In Figure 33 the free surface elevation of this wave train is shown. From this figure it can be seen that the wave form is preserved and is not affected by alterations that could disturb the wave profile.

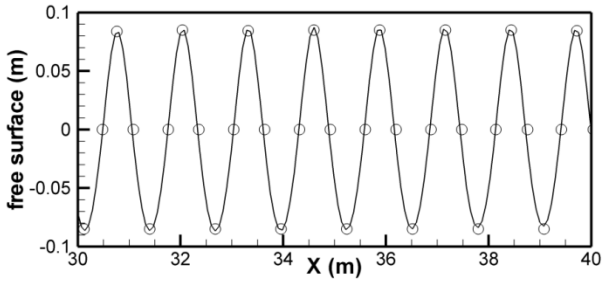

Figure 32. Wave profile. Wave train A: a=0.17m T=0.87s ε=0.2 and μ^2=0.5. continuous line: numerical solution; circle: data extrapolated from the analytical solution.

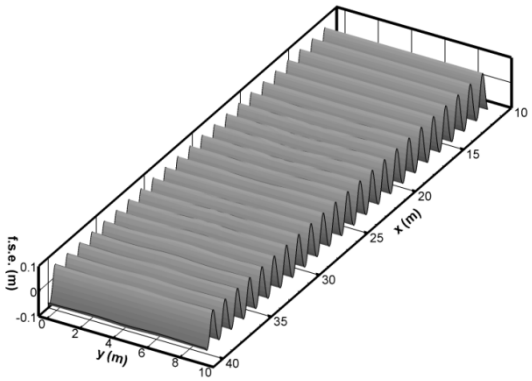

Figure 33 Instantaneous wave field . Wave train A: a=0.17m T=0.87s ε=0.2 and μ^2=0.5.

The second wave train (B) has an amplitude of a=0.34m, a period of T=1.048s, a good non linearity of ε=0.4 and a good dispersion of μ^2=0.25. In Figure 34 and 35 are shown the wave profile and the wave field after 50s of simulation. It can be seen (Figure 34) how the numerical results and analytical solution are in good agreement and the high distortion of the grid (Figure 35) doesn't affect the model capability to represent non linear and dispersive waves.

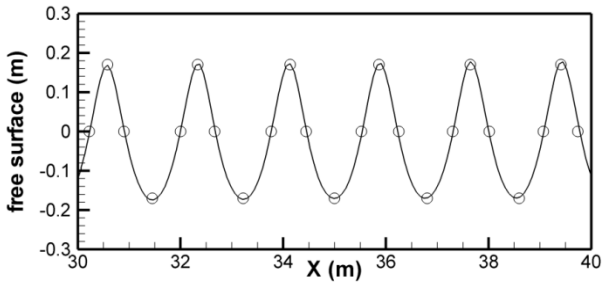

Figure 34. Wave profile. Wave train B: a=0.34m T=1.048s ε=0.4 and μ^2=0.25. continuous line: numerical solution; circle: data extrapolated from the analytical solution.

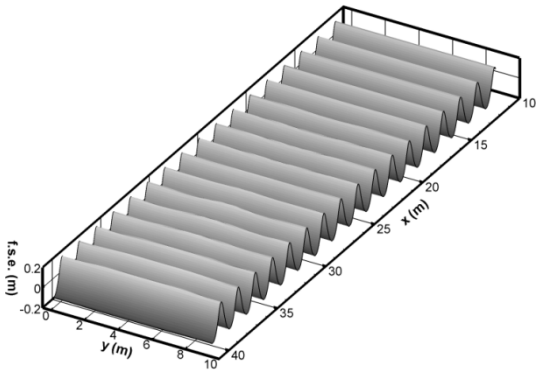

Figure 35. Instantaneous wave field . Wave train B: a=0.34m T=1.048s ε=0.4 and μ^2=0.25.

In Figure 36 is shown the wave profile related to train wave C with an amplitude of a=0.4525m, a period of T=1.106s, a highly non linearity of ε=0.65 and a good dispersion of μ^2=0.2. Is shown how the wave profile, after 50s of simulation, doesn't have any deformation and it is in good agreement with the analytical solution. In Figure 37 is shown how also the wave field doesn't have high alteration due to the grid distortion.

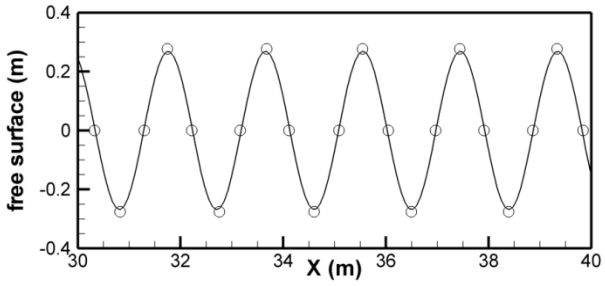

Figure 36. Wave profile. Wave train C: a=0.4525m T=1.106s ε=0.65 and μ^2=0.2. continuous line: numerical solution; circle: data extrapolated from the analytical solution.

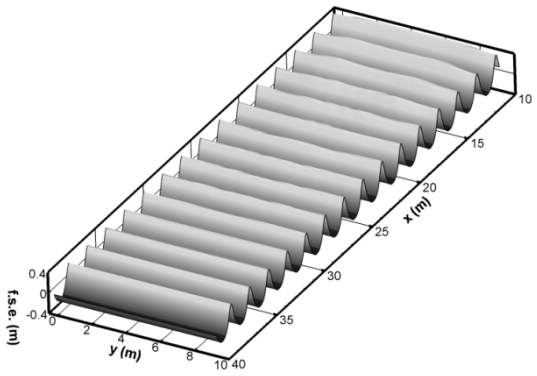

Figure 37. Instantaneous wave field . Wave train C: a=0.4525m T=1.106s ε=0.65 and μ^2=0.2.

2. A new 3D FV Non-hydrostatic Shock Capturing model for free surface flow

In this chapter a new Finite-Volume Non-Hydrostatic and Shock-Capturing three-Dimensional Model for the simulation of wave-structure interaction and hydrodynamic phenomena (wave refraction, diffraction, shoaling and breaking) is proposed. The model is based on an integral formulation of the Navier-Stokes Equations which are solved on a time dependent coordinate system: a coordinate transformation maps the varying coordinates in the physical domain to a uniform transformed space. The motion equations are discretized by means of a Finite Volume Shock-Capturing numerical procedure based on high order WENO reconstructions. The solution procedure for the motion equations uses a third order accurate Runge-Kutta (SSPRK) fractional-step method and applies a pressure corrector formulation in order to obtain a divergence-free velocity field at each stage. The proposed model is validated against several benchmark test cases.

2.1. Introduction on 3D model

Since 1960s several studies have been conducted to evaluate hydrodynamic phenomena related to wave motion. Since computational capabilities were exiguous, just a few models has been developed to make these simulations.

As the computational power advanced a few new approaches of modeling surface waves have been developed and became more popular. One was based on the depth-averaged equations, such as shallow water equation model or Boussinesq equation model (Abbot et al [1985], Liu et al [1994]). The depth-averaged models are computationally efficient with the trade-off of losing depth-related information.

The most recent Boussinesq models have very good dispersion and non-linearity properties (Madsen and Sørensen [1992]; Nwogu [1993]; Wei et al., [1995]) and some models even retain the second order vertical vorticity component (Chen et al [2003], Chen [2006]). These models so-called “depth averaged” are still very popular in coastal engineering for example to study coastal flooding due to tsunami (Fuhrman and Madsen [2003], Watts et al [2003]) or in sediment transport field (Rakha et al [1997], Briganti et al [2012]). These models are even used in all coastal simulation for whose it is not in which is not necessary the hydrodynamic quantities vertical distribution.

In order to solve three-dimensional engineering problems however is required models that take into account the three-dimensionality of the vorticity and turbulent phenomena. A different approach.

Commonly used in the past, is to solve the Navier Stokes Equations by the assumption of hydrostatic pressure. The pioneers in these studies were Johns and Jefferson [1980], Casulli and Cheng [1992]. Due to the employment of hydrostatic pressure assumption, such models are generally applied to shallow water flows. When the vertical acceleration of fluids is strong, i.e., wave impact on structures, the models may fail to provide accurate results (Lin and Li [2002]).

In several applications, the vertical acceleration might not be negligible compared to to the gravity acceleration, mostly to simulate highly dispersive and Non-linear phenomena in depth and intermediate water. For these reasons the most recent models take into account the dynamic pressure (Lai et al [2010], Bradford [2011], Ma et al [2012]).

The “free surface fully non-hydrostatic three-dimensional models” did not became popular before the XXI century, when the computational power greatly increased. In these models the total pressure was splitted in two parts: the dynamic pressure and the hydrostatic pressure. The governing equations were solved in two different steps: in the first step were discretized the convective terms, the hydrostatic pressure, the term related to the bottom slope and the stress term. In the second step was calculated the dynamic pressure by solving the so-called Poisson Equation.

The firsts “free surface fully non-hydrostatic models” were solved by using Cartesian coordinates (Harlow & Welch [1965], Thomas & Leslie [1992], Casulli&Stelling [1998]);by this way the vertical fluxes crossed calculus cell arbitrarily. This led to the difficulty to correctly assign pressure kinematic condition on free surface elevation. Furthermore Cartesian coordinates is not able to represent complex bottom topography.

This approach led to the presence of spurious oscillations in numerical solution and requested an high number of vertical layers (Ma et al [2012]). A direct simplification of the above-mentioned approach is to express the vertical coordinate as a function of quantities that depends only by horizontal coordinates. By this way the physical grid (Cartesian grid) is mapped by a computational grid (sigma-coordinate, Phillips [1957]) which has always a rectangular prism shape. By doing so, the free surface is always located at the upper computational boundary and the bottom is always located at the lower boundary of computational grid and they an be determined by applying the free surface and bottom boundary conditions.

Furthermore the pressure boundary condition at the free surface can be exactly assigned to zero without any approximation (Ma et al [2012]). The integral form of the motion equations, expressed in terms of conserved variables, guarantees that high-order shock-capturing numerical schemes converge to correct weak solutions and are then able to directly simulate wave breaking and the energy dissipation associated with it (Toro [2001]). These schemes are Shock-Capturing methods and are able to track the actual location of the wave breaking without requiring any criterion

(Bradford [2005]).

In this thesis, the numerical simulation of wave transformation relies on the resolution of the motion equations expressed in an integral formulation on a time dependent coordinate system: a coordinate transformation maps the varying coordinates in the physical domain to a uniform transformed space. The pressure boundary conditions are placed on the upper face of each computational cell. The solution procedure for motion equations uses a third order accurate Runge-Kutta (SSPRK) fractional-step method and applies a pressure corrector formulation in order to obtain a divergence free velocity field at each stage. In the prediction phase of the fractional-step proposed model, the motion equations are discretized by means of a shock-capturing numerical procedure based on high order WENO reconstructions (Cap 2.4.1). The numerical flux is given at each cell interface by the solution of an approximate HLL Riemann problem (Harten et al [1983]). In the corrector phase of the fractional-step proposed model, in order to solve the Poisson equation and reduce the computational costs related to it, an alternate Zebra four-colour Gauss-Siedel relaxation method with a V-cycle multigrid strategy is used (Trottenberg et al [2001]).

2.2. List of Symbols

ρ : density of the fluid

u^l : velocity of fluid particle

$\Delta A(t)$: surface of a material element of fluid

$\Delta V(t)$: volume of a material element of fluid

n_m : outward unit normal vector to the surface $\Delta A(t)$

v^m : Cartesian velocity vector with which the $\Delta A(t)$ surface moves

$\frac{D}{Dt}$: intrinsic derivative

T^{lm} : stress tensor

f^l : external body forces

p : total pressure

q : dynamic pressure

η : free surface displacement

h : still water depth

H : total water depth

2.3. An integral form of 3D sigma-coordinate equations

In order to express the integral formulation of the momentum equations in a time dependent coordinate system let us start from the intrinsic derivative of the momentum, that can be expressed as:

$$\frac{D}{Dt}\int_{\Delta V_1(t)} \rho\, u^l dV_1 = \int_{\Delta V_1(t)} \frac{\partial \rho u^l}{\partial t} dV_1 + \int_{\Delta A_1(t)} \rho\, u^l u^m n_m\, dA_1 \qquad (1)$$

where $\Delta A_1(t)$ and $\Delta V_1(t)$ are, respectively, the surface and the volume of a material element of fluid which moves with velocity u^l $(l = 1,3)$ defined in a reference system of coordinates x^l $(l = 1,3)$, n_m $(m = 1,3)$ is the outward unit normal vector to the surface $\Delta A_1(t)$ and ρ is the density of the fluid. (The superscripts notation indicate components and not powers).

The intrinsic derivative has two special requirements: it should reflect the total variation of a tensor vector along the curve due to infinitesimal change of *t* (correspondingly, in Cartesian coordinates, this derivative will reduce to the material derivative), and it should preserve tensor character so that it can be applied to any coordinate system (Luo and Bewley [2004]). In other words, in this case, the intrinsic derivative is a material derivative that takes into account the time variation of volume and surface control in which the rate of change of momentum is calculated.

The three dimensional Leibniz integral rule, for a time dependent case, can be written as:

$$\frac{d}{dt}\int_{\Delta V_2(t)} \rho\, u^l dV_2 = \int_{\Delta V_2(t)} \frac{\partial \rho u^l}{\partial t} dV_2 + \int_{\Delta A_2(t)} \rho\, u^l v^m n_m\, dA_2 \qquad (2)$$

where $\Delta V_2(t)$ is a time varying control volume which has not the same velocity as that of the fluid, whose surface is given by $\Delta A_2(t)$ and where v^m $(m = 1,3)$ is the velocity vector of the moving surface $\Delta A_2(t)$.

It is assumed that, at the instant $t, \Delta V_1(t) = \Delta V_2(t) = \Delta V(t)$. From Equations (1) and (2):

$$\frac{D}{Dt}\int_{\Delta V(t)} \rho\, u^l dV = \frac{d}{dt}\int_{\Delta V(t)} \rho\, u^l dV + \int_{\Delta A(t)} \rho u^l (u^m - v^m) n_m dA\,. \qquad (3)$$

By using the intrinsic derivative of the momentum (expressed by Equation (3)), the integral form of the momentum equations in a time dependent coordinate system can be deduced; this equation is

given by:

$$\frac{d}{dt}\int_{\Delta V(t)} \rho u^l dV + \int_{\Delta A(t)} \rho u^l (u^m - v^m) n_m dA = \int_{\Delta V(t)} \rho f^l dV + \int_{\Delta A(t)} T^{lm} n_m dA \quad (4)$$

where T^{lm} is the stress tensor and f^l $(l = 1,3)$ represents the external body forces per unit mass vector:

$$f^l = -\frac{1}{\rho} p_{,l} - g\delta_{l3} \quad (5)$$

in which δ_{l3} is the Kroneker symbol and p is the total pressure defined by the sum of the hydrostatic and the dynamic component:

$$p = \rho G(\eta - x^3) + q \quad (6)$$

where G is the constant of gravity, q is the dynamic pressure, η is the free surface displacement, the comma with an index in subscript denotes the derivative as $[\ ]_{,l} = \partial[\ ]/\partial x^l$ and (x^1, x^2, x^3, t) is a Cartesian coordinate system.

The first integral on the right hand side of the Equation (4) can be rewritten as:

$$\int_{\Delta V(t)} \rho f^l dV = -\int_{\Delta V(t)} [(\rho G\eta + q)_{,l}] dV \quad (7)$$

By applying Green's Theorem the right hand side of Equation (7) becomes:

$$-\int_{\Delta V(t)} [(\rho G\eta + q)_{,l}] dV = -\int_{\Delta A(t)} \rho G\eta n_m dA - \int_{\Delta V(t)} [q_{,l}] dV \quad (8)$$

By introducing Equation (8) in Equation (4), we get:

$$\frac{d}{dt}\int_{\Delta V(t)} \rho u^l dV = -\int_{\Delta A(t)} [\rho u^l (u^m - v^m) n_m + \rho G\eta n_m] dA - \int_{\Delta V(t)} [q_{,l}] dV + \int_{\Delta A(t)} T^{lm} n_m dA \quad (9)$$

In order to simulate the fully dispersive wave processes, Equation (9) can be transformed in the following way. Let $H(x^1, x^2, t) = h(x^1, x^2, t) + \eta(x^1, x^2, t)$, where h is the water depth and η is

the surface elevation. In order to accurately represent the bottom topography and the surface geometry and correctly assign pressure and kinematics conditions on the bottom and the free surface elevation, we consider a transformation from the Cartesian coordinate (x^1, x^2, x^3, t) to the sigma-coordinates (Phillips (1957)) $(\xi^1, \xi^2, \xi^3, \tau)$ where:

$$\xi^1 = x^1, \qquad \xi^2 = x^2, \qquad \xi^3 = \frac{x^3+h}{H}, \qquad \tau = t, \tag{10}$$

the following relation is valid:

$$v^3 = -\frac{\partial \xi^3}{\partial t} = \frac{\xi^3}{H}\frac{\partial H}{\partial \tau} \tag{11}$$

This coordinate transformation basically maps the varying vertical coordinates in the physical domain to a uniform transformed space where ξ^3 spans from 0 to 1.

We define the transformation matrix $C_m^l = \partial x^l / \partial \xi^m$ and its inverse $\bar{C}_m^l = \partial \xi^l / \partial x^m$ $(l, m = 1, 3)$. The metric tensor and its inverse are defined by $g_{lm} = C_l^k C_m^k$ and $g^{lm} = \bar{C}_l^k \bar{C}_m^k$, respectively. The Jacobian of the transformation is defined by $\sqrt{g} = det\,(C_m^l)$. It is not difficult to verify that, in the particular case of the above-mentioned transformation, $\sqrt{g} = H$.

We also define the volume element $\Delta V(t) = \Delta x^1 \Delta x^2 \Delta x^3 = \sqrt{g}\Delta\xi^1\Delta\xi^2\Delta\xi^3$ in the physical space, and the volume element in the transformed space $\Delta V^* = \Delta\xi^1\Delta\xi^2\Delta\xi^3$. It is possible to see that the first volume element is time dependent while the second one is not. In the same way we define the surface element in the physical space $\Delta A(t) = \Delta x^\alpha \Delta x^\beta = \sqrt{g}\Delta\xi^\alpha\Delta\xi^\beta$, and the surface element in the transformed space $\Delta A^* = \Delta\xi^\alpha\Delta\xi^\beta$ (in which α, β=1,2,3 are cyclic).

For an incompressible fluid, Equation (9) expressed in the time dependent coordinate system $(\xi^1, \xi^2, \xi^3, \tau)$, transformed from the Cartesian reference system of coordinates (x^1, x^2, x^3, t) by Equation (10), and with the external body forces given by the only gravitational force, becomes:

$$\frac{d}{d\tau}\int_{\Delta V(\tau)} u^l dV = -\int_{\Delta A(\tau)}[u^l(u^m - v^m)n_m + G\eta n_m]dA - \frac{1}{\rho}\int_{\Delta V(\tau)}[q_{,l}]dV + \frac{1}{\rho}\int_{\Delta A(\tau)} T^{lm} n_m dA \tag{12}$$

The time dependent coordinate system moves with velocity given by $v^m = \left\{0, 0, \frac{\xi^3}{H}\frac{\partial H}{\partial \tau}\right\}$. The first integral on the right hand side of Equation (12) is related to the convective term and the hydrostatic

pressure gradient; the second integral on the right hand side is related to the dynamic pressure gradient and the third term is related to the stress tensor.

Let us introduce a restrictive condition on the volume element $\Delta V(t)$: in the following $\Delta V(t)$ must be considered as a volume element that is bounded by curves lying on the coordinate lines.

We define the averaged cell value (in the transformed space) of primitive variables:

$$\bar{H} = \frac{1}{\Delta V^*}\int_{\Delta V} H d\xi^1 d\xi^2 d\xi^3; \qquad \bar{u}^l = \frac{1}{\Delta V^*}\int_{\Delta V} u^l d\xi^1 d\xi^2 d\xi^3 \tag{13}$$

and conserved variable:

$$\overline{Hu^l} = \frac{1}{\Delta V^*}\int_{\Delta V} u^l H \, d\xi^1 d\xi^2 d\xi^3 \tag{14}$$

By using Equations (13-14), Equation (12) is transformed in:

$$\begin{aligned}
\frac{\partial \overline{Hu^l}}{\partial \tau} = &-\frac{1}{\Delta V^*}\sum_{\alpha=1}^{3}\left\{\int_{\Delta A^{*\alpha+}}[Hu^l(u^\alpha - v^\alpha) + GH^2]d\xi^\beta d\xi^\gamma \right.\\
&\left. - \int_{\Delta A^{*\alpha-}}[Hu^l(u^\alpha - v^\alpha) + GH^2]d\xi^\beta d\xi^\gamma\right\}\\
&+\frac{1}{\Delta V^*}\sum_{\alpha=1}^{3}\left\{\int_{\Delta A^{*\alpha+}} GhH d\xi^\beta d\xi^\gamma - \int_{\Delta A^{*\alpha-}} GhH d\xi^\beta d\xi^\gamma\right\}\\
&-\frac{1}{\Delta V^*}\frac{1}{\rho}\int_{\Delta V^*} q_{,l} H \, d\xi^1 d\xi^2 d\xi^3\\
&+\frac{1}{\Delta V^*}\sum_{\alpha=1}^{3}\left\{\int_{\Delta A^{*\alpha+}} \frac{HT^{l\alpha}}{\rho} d\xi^\beta d\xi^\gamma - \int_{\Delta A^{*\alpha-}} \frac{HT^{l\alpha}}{\rho} d\xi^\beta d\xi^\gamma\right\}
\end{aligned} \tag{15}$$

where $\Delta A^{*\alpha+}$ and $\Delta A^{*\alpha-}$ indicate the contour surfaces of the volume element ΔV^* on which ξ^α is constant and which are located at the larger and at the smaller value of ξ^α respectively. Here the indexes α, β and γ are cyclic. The total time derivative on the left hand side of Equation (12) became a local time derivative (Equation (15)) because the integral is a simple function of $(\xi^1, \xi^2, \xi^3, \tau)$. It is possible to see that the advancing in time of the conserved variables is applied in the transformed space that is not time varying. The time varying of the geometric components is

expressed by the metric terms. Otherwise the mass conservation principle is given by:

$$\frac{D}{Dt}\int_{\Delta V(t)} \rho \, dV = 0 \tag{16}$$

By using the Equation (2) (as well as Equation (1)) we obtain the integral form of the continuity equation expressed in a time dependent coordinate system:

$$\frac{d}{d\tau}\int_{\Delta V(\tau)} \rho dV + \int_{\Delta A(\tau)} \rho \, (u^m - v^m) n_m dA = 0 \tag{17}$$

By considering ρ as a constant and uniform value, Equation (17) becomes:

$$\frac{d}{d\tau}\int_{\Delta V^*} H \, d\xi^1 d\xi^2 d\xi^3 + \sum_{\alpha=1}^{3} \left\{ \int_{\Delta A^{*\alpha+}} (u^\alpha - v^\alpha) H d\xi^\beta d\xi^\gamma - \int_{\Delta A^{*\alpha-}} (u^\alpha - v^\alpha) H d\xi^\beta d\xi^\gamma \right\} = 0 \tag{18}$$

By developing the sum of indexes α, β and γ:

$$\begin{aligned} \frac{d}{d\tau}\int_{\Delta V^*} H \, d\xi^1 d\xi^2 d\xi^3 &+ \left\{ \int_0^1 \left[\int_{\xi^{1+}} H u^1 d\xi^2 \right] d\xi^3 - \int_0^1 \left[\int_{\xi^{1-}} H u^1 d\xi^2 \right] d\xi^3 \right\} \\ &+ \left\{ \int_0^1 \left[\int_{\xi^{2+}} H u^2 d\xi^1 \right] d\xi^3 - \int_0^1 \left[\int_{\xi^{2-}} H u^2 d\xi^1 \right] d\xi^3 \right\} \\ &+ \left\{ \iint_{A^*_{xy}(\xi^3=1)} (u^3 - v^3) H d\xi^1 d\xi^2 - \iint_{A^*_{xy}(\xi^3=0)} (u^3 - v^3) H d\xi^1 d\xi^2 \right\} = 0 \end{aligned} \tag{19}$$

where $\Delta A^*_{xy} = \Delta\xi^1 \Delta\xi^2$ is the horizontal surface element in the transformed space. By considering the bottom and surface kinematics boundary conditions the last bracket of the Equation (19) is null. We also have that:

$$\frac{d}{d\tau}\int_{\Delta V^*} H \, d\xi^1 d\xi^2 d\xi^3 = \int_{A^*_{xy}} \frac{\partial H}{\partial \tau} \, d\xi^1 d\xi^2 \tag{20}$$

because H does not depend from ξ^3 and ΔV^* is not time dependent. We can also write:

$$\frac{\partial \bar{H}}{\partial \tau} = \frac{1}{A^*_{xy}} \int_{A^*_{xy}} \frac{\partial H}{\partial \tau} \, d\xi^1 d\xi^2 \tag{21}$$

By considering the bottom and surface kinematics boundary conditions, by using Equations (13-20-21) and by dividing Equation (19) by ΔA^*_{xy}, for $\Delta A^*_{xy} \to 0$, we obtain:

$$\frac{\partial \bar{H}}{\partial \tau} + \frac{1}{\Delta A_{xy}} \int_0^1 \sum_{\alpha=1}^{2} \left[\int_{\Delta A^{\alpha+}} H u^\alpha d\xi^\beta - \int_{\Delta A^{\alpha-}} H u^\alpha d\xi^\beta \right] = 0 \tag{22}$$

Equation (22) represents the governing equation for the surface movements. Equations (15) and (22) represent the expressions of the three dimensional motion equations as a function of the $\overline{Hu^l}$ and $\bar{H}$ variables in the time dependent coordinate system $(\xi^1, \xi^2, \xi^3, \tau)$. The numerical integration of the above mentioned Equations (15) and (22) makes it possible to simulate the fully dispersive wave processes simulation. The turbulent kinematic viscosity in the stress tensor is estimated by a Smagorisky sub grid model.

2.4. Numerical Scheme

A combined finite-volume and finite-difference scheme with a Godunov-type method was applied in order to discretize Equations (15) and (22). By following the strategy described by Stelling and Zijlema [2003] a particular kind of staggered grid framework is introduced, in which the velocities are placed at the cell centers and the pressure is defined at the horizontal cell faces. The state of the system is known at the centre of the calculation cells and it is defined by the cell-averaged values of $\overline{Hu^l}$ and $\bar{H}$. $\tau^{(n)}$ is the time level of the known variables while $\tau^{(n+1)}$ is the time level of the unknown variables.

The solution procedure uses three-stage third-order nonlinear Strong Stability-Preserving (SSP) Runge–Kutta scheme (Gottlieb et al [2001]) for Equations (15) and (22). A pressure correction formulation is applied in order to obtain a divergence free velocity field at each time level. With $\overline{Hu^l}^{(n)}$ known, $\overline{Hu^l}^{(n+1)}$ is calculated with the following three stage iteration procedure.

Let:

$$\overline{Hu^l}^{(0)} = \overline{Hu^l}^{(n)} \tag{23}$$

At each stage p (where $p = 1,2,3$) an auxiliary field $\overline{Hu^l}_*^{(p)}$ is obtained directly from Equation (15) by using values from the previous stage:

$$\overline{Hu^l}_*^{(p)} = \sum_{q=0}^{p-1} \left\{ \Omega_{pq} \overline{Hu^l}^{(q)} + \Delta\tau\, \varphi_{pq} D\left[Hu^{l(q)}, \tau^{(n)} + d_q \Delta\tau \right] \right\} \tag{24}$$

where $D(H, u^l, \tau)$ indicates the right hand side of Equation (15), in which the term related to the dynamic pressure gradient is omitted. See Spiteri and Ruuth [2001], for the values of coefficients Ω_{pq}, φ_{pq} and d_q. The auxiliary velocity field $\bar{u}^{l(p)}_*$ (associated to the auxiliary variable $\overline{Hu^l}_*^{(p)}$ calculated by Equation (24) by using $\bar{H}_*^{(p-1)}$) does not satisfy the continuity equation. As a result, the velocity and the pressure fields are corrected, at each intermediate step p, by introducing a scalar potential Ψ which is calculated by the well-known Poisson pressure equation given by:

$$\nabla^2\Psi^{(p)} = -\frac{\rho}{\Delta t} div\left(\bar{u}_*^{l(p)}\right) \tag{25}$$

Equation (25) expressed in the time dependent coordinate system, is given by:

$$\begin{aligned}\frac{\partial\hat{}2\Psi(\mathrm{p})}{\partial\xi^{1}\hat{}2} + \frac{\partial\hat{}2\Psi(\mathrm{p})}{\partial\xi^{2}\hat{}2} + \left[\left(\frac{\partial\xi^3}{\partial x}\right)\hat{}2 + \left(\frac{\partial\xi^3}{\partial y}\right)\hat{}2 + \left(\frac{\partial\xi^3}{\partial z}\right)\hat{}2\right]\frac{\partial\hat{}2\Psi(\mathrm{p})}{\partial\xi^{3}\hat{}2} \\ + 2\left(\frac{\partial\xi^3}{\partial x}\frac{\partial\hat{}2\Psi(\mathrm{p})}{\partial\xi^1\partial\xi^3} + \frac{\partial\xi^3}{\partial y}\frac{\partial\hat{}2\Psi(\mathrm{p})}{\partial\xi^2\partial\xi^3}\right) + \left(\frac{\partial\hat{}2\xi^3}{\partial x\partial\xi^1} + \frac{\partial\hat{}2\xi^3}{\partial y\partial\xi^2}\right)\frac{\partial\Psi(\mathrm{p})}{\partial\xi^3} \\ = \frac{\rho}{\Delta t}\left(\frac{\partial\bar{\mathrm{u}}^{1(\mathrm{p})}_*}{\partial\xi^1} + \frac{\partial\bar{\mathrm{u}}^{1(\mathrm{p})}_*}{\partial\xi^3}\frac{\partial\xi^3}{\partial x} + \frac{\partial\bar{\mathrm{u}}^{2(\mathrm{p})}_*}{\partial\xi^2} + \frac{\partial\bar{\mathrm{u}}^{2(\mathrm{p})}_*}{\partial\xi^3}\frac{\partial\xi^3}{\partial y} + \frac{\partial\bar{\mathrm{u}}^{3(\mathrm{p})}_*}{\partial\xi^3}\frac{\partial\xi^3}{\partial z}\right)\end{aligned} \tag{26}$$

Equation (26) is defined at the horizontal cell center and it is discretized by a second order cell centered finite-difference scheme, the right hand side of the Equation (26) is also discretized by the same scheme where the values at the horizontal cell center of the variable $\bar{u}_*^{l(p)}$ is interpolated. By this way Equation (26) can be reduced to an algebraic linear system like $Aq = b$, where A is the coefficient matrix (with 19 non-zero diagonal coefficient), q is the scalar potential vector and b is the source vector. This algebraic linear system is solved by using an implicit scheme based on a Zebra four color Gauss-Seidel Alternate method (Rosenfeld et al [1991]) and a Multigrid V-Cycle accelerator as described in Trottenberg et al [2001].

The corrector irrotational velocity field is calculated by the following expression:

$$\bar{u}^{1}{}_c^{(p)} = -\frac{\Delta t}{\rho}\left(\frac{\partial\Psi^{(p)}}{\partial\xi^1} + \frac{\partial\Psi^{(p)}}{\partial\xi^3}\frac{\partial\xi^3}{\partial x}\right) \tag{27}$$

$$\bar{u}^{2}{}_c^{(p)} = -\frac{\Delta t}{\rho}\left(\frac{\partial\Psi^{(p)}}{\partial\xi^2} + \frac{\partial\Psi^{(p)}}{\partial\xi^3}\frac{\partial\xi^3}{\partial y}\right) \tag{28}$$

$$\bar{u}^{3}{}_c^{(p)} = -\frac{\Delta t}{\rho}\left(\frac{\partial\Psi^{(p)}}{\partial\xi^3}\frac{\partial\xi^3}{\partial z}\right) \tag{29}$$

in order to obtain a divergence-free velocity field at each stage and a non-hydrostatic velocity field, the velocity field must be corrected as:

$$\bar{u}^{l(p)} = \bar{u}^{l}{}_*^{(p)} + \bar{u}^{l}{}_c^{(p)} \tag{30}$$

Let us indicate with $L(H,\ u^l, \tau)$ the right hand side of Equation (22). The advancing at the p stage of the depth $\overline{H}^{(p)}$ is obtained by:

$$\overline{H}^{(p)} = \overline{H}^{(p-1)} + L(H^{(p-1)}, u^{l\,(p-1)}, \tau^n + \Delta\tau) \tag{31}$$

The value of $\overline{Hu^l}^{(n+1)}$ is given by:

$$\overline{Hu^l}^{(n+1)} = \overline{Hu^l}^{(3)} \tag{32}$$

For the calculation of the $D(H, u^l, \tau)$ and $L(H, u^l, \tau)$ terms the numerical approximations of the integrals on the right hand side of Equations (15) and (22) is required.

The aforementioned calculation is based on the following sequence.

1. High order WENO reconstructions, from cell averaged values, of the point values of the unknown variables at the centre of the contour face which define the calculation cells. At the centre of the contour face which is common with two adjacent cells, two point values of the unknown variables are reconstructed by means of two WENO reconstruction defined on two adjacent cells (section 2.4.1).
2. Advancing in time of the point values of the unknown variables at the centre of the contour face by means of the so-called solution of the HLL Riemann problem (Harten et al [1983]), with initial data given by the pair of point-values computed by two WENO reconstructions defined on the two adjacent cells.
3. Calculation of the spatial integrals which define $D(H, u^l, \tau)$ the $L(H, u^l, \tau)$.
4. Solving the Poisson pressure equation by using a Zebra four color Gauss-Seidel Alternate method and a Multigrid V-Cycle.
5. Correcting the hydrostatic velocity field by using a scalar potential Ψ.
6. Advancing in time of the total local depth (Equations (22)) by using the Non-Hydrostatic velocity field.

2.5. Results

2.5.1. Wave transformation over a submerged bar

The ability of the proposed model to simulate the wave decomposition and the spectrum evolution over a submerged bar is verified: the numerical results are compared against the experimental results from the test case presented by Beji and Batties [1993]. The experimental channel has a length of 30m and the still water depth is 0.4m which is reduced to 0.1m over the submerged breakwater. The offshore slope of the breakwater is 1/20 and the onshore slope is 1/10. The wave train is incident from the left boundary of the channel and is characterized by a period of 2.02s and amplitude 1.0cm. The computational domain reproduces the experimental channel and it is shown in Figure 1. The periodic wave is generated on the left boundary and a sloped beach is placed on the right boundary in order to dissipate the wave motion. The time discretization is 0.001s; the spatial discretization is Δx=0.01m. In the numerical simulation three vertical layers are used the dispersive and non linear phenomena related to this test.

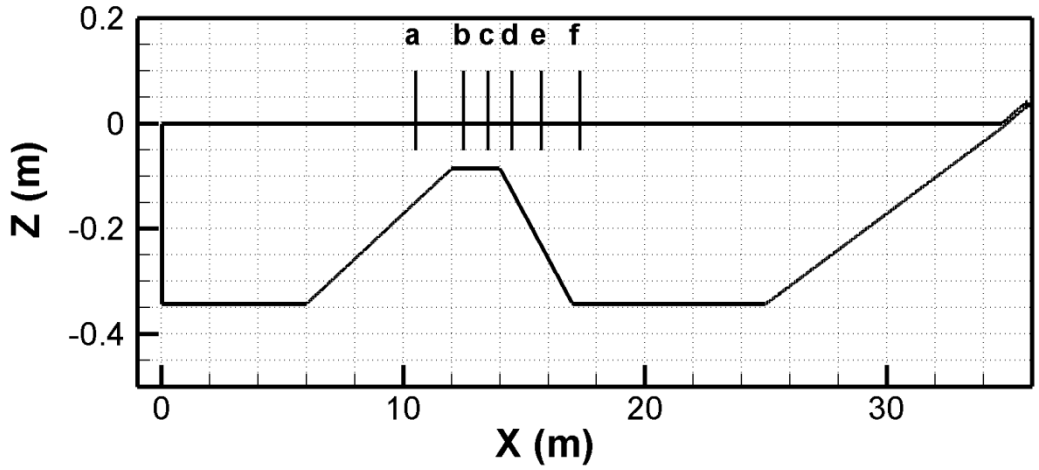

Figure 1. Wave transformation over a submerged bar. Bottom topography with station measurement: a) x=10.5m; b) x=12.5m; c) x=13.5m; d) x=14.5m; e) x=15.7m; f) x=17.3m.

In Figure 2 the comparison between the numerical results and the experimental data for the wave transformation in the stations, which are indicated in Figure 1, is shown. At the station *a* the wave train is still almost sinusoidal and the numerical result are in very good agreement with the experimental data. In the next stations (stations *b, c, d*) the waves become progressively steepened by the interaction between the wave motion and the submerged bar, and then lose the vertical

symmetry. In the last stations (stations *e* and *f*) it is possible to notice the wave breaking and how the proposed model is able to simulate the wave transformation due to the wave-bar interaction in terms of both phases and amplitudes by using only three vertical layers.

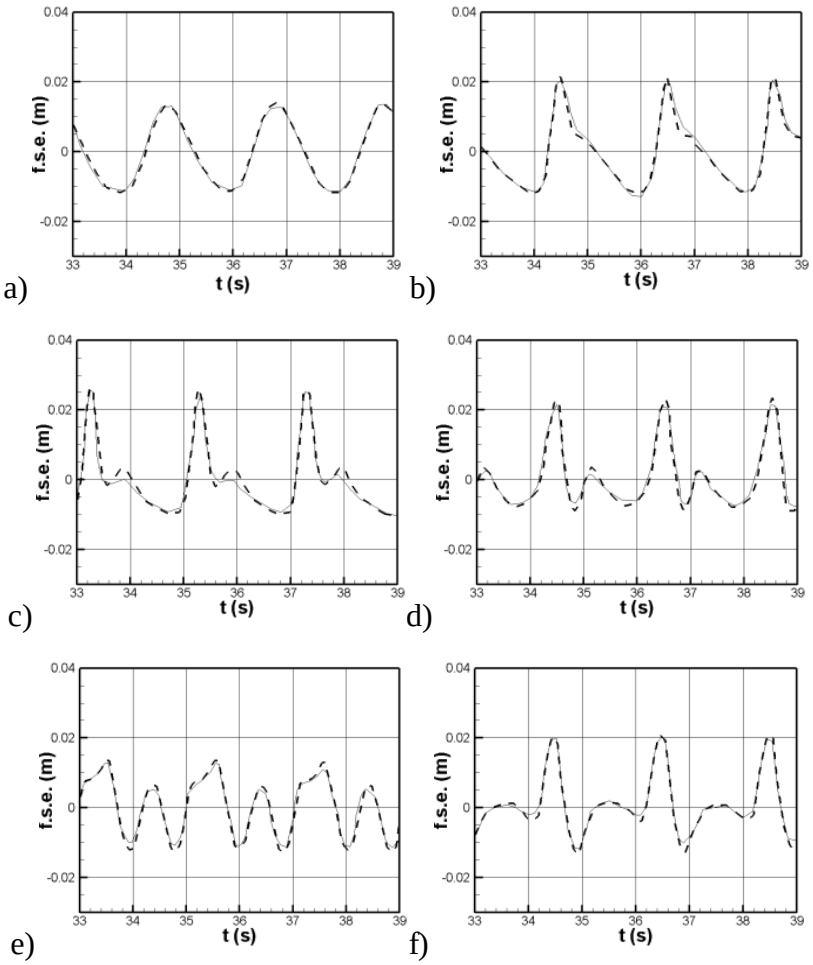

Figure 2. Wave transformation over a submerged bar. Comparison between numerical results (solid line) and experimental data (dashed line) of the surface elevation at a) x=10.5m; b) x=12.5m; c) x=13.5m; d) x=14.5m; e) x=15.7m; f) x=17.3m.

2.5.2. Wave deformation by an elliptic shoal.

This experiment is carried out in order to verify the ability of the proposed hydrodynamic model to simulate the physical processes of the wave propagation and the wave deformation (refraction and diffraction) due to a shoal. To this aim we numerically reproduce an experiment extracted from the "Report W. 154-VIII" of the Delft Hydraulics Laboratory, proposed by Berkhoff et al [1982].
The bottom of the physical domain has a slope of 1/50. Let (*x*,*y*) be the Cartesian axis and (*x'*,*y'*) be the auxiliary axis related to the Cartesian axis by a rotation of -20°. The bottom equations are given by:

$$H = 0.45 \qquad y' \leq -5.484 \tag{33}$$

$$H = \max(0.1; 0.45 - 0.02(5.484 + y')) \qquad y' \geq -5.484 \tag{34}$$

It has to be notice that the minimum depth is 10 cm: only non breaking-waves are considered.
The obstacle boundary and thickness equations are given by:

$$\left(\frac{x'}{4}\right)^2 + \left(\frac{y'}{3}\right)^2 = 1 \tag{35}$$

$$d = -0.3 + 0.5\sqrt{1 - \left(\frac{x'}{5}\right)^2 - \left(\frac{y'}{3.75}\right)^2} \tag{36}$$

In Figure 3 the bottom topography of the computational domain is shown. The spatial discretization step is $\Delta x = \Delta y = 0.05m$, whereas the time discretization step is $\Delta t = 0.005s$. The wave motion is generated on the eastern boundary of the computational domain and a sponge zone is placed on the western side of the computational domain in order to absorb the wave motion energy. The wave train has an amplitude of 0.0464m and a period of 1s. In the numerical simulation four vertical layers are used in the vertical direction. Reflective conditions are set for the lateral boundaries.

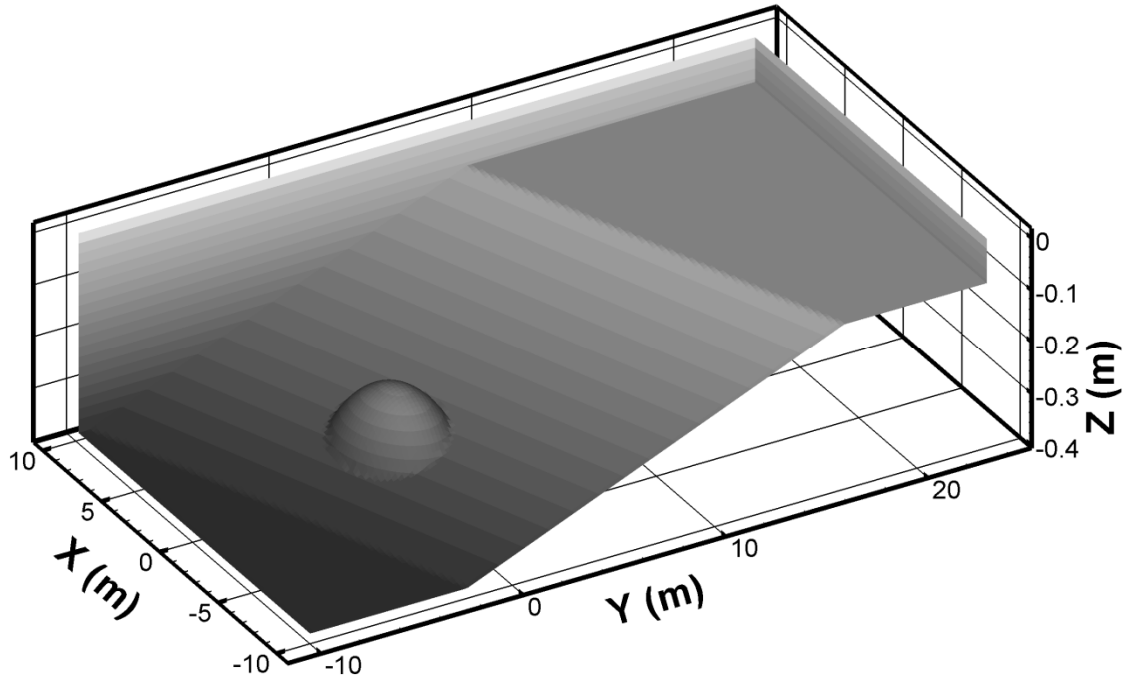

Figure 3. Wave deformation by an elliptic shoal. Bottom topography of the computational domain.

In Figure 4.a-d the comparison between the numerical results and the measured data from Berkhoff et al [1982] of the wave heights related to section x =2 m, x =0 m, y =3 m and y=9 m are respectively shown. The computed wave height is obtained by taking the difference between the maximum and the minimum free surface elevation considered over a time interval in which the wave form is permanent. From Figure 4a-b it is possible to see how the bottom elliptic obstacle modifies the wave motion: the boundary of the obstacle (Figure 4a) causes a diffraction phenomenon that reduces the wave height whereas the top of the obstacle (Figure 4b) increases the wave height (shoaling). Figure 4c-d show how the diffraction and the refraction phenomena cause the loss of symmetry and periodicity behind the obstacle.

In Figure 5 an instantaneous wave field is shown. In this Figure the shoaling on the top of the obstacle, the diffraction behind the obstacle and the refraction phenomena dues by bottom slope can be noticed.

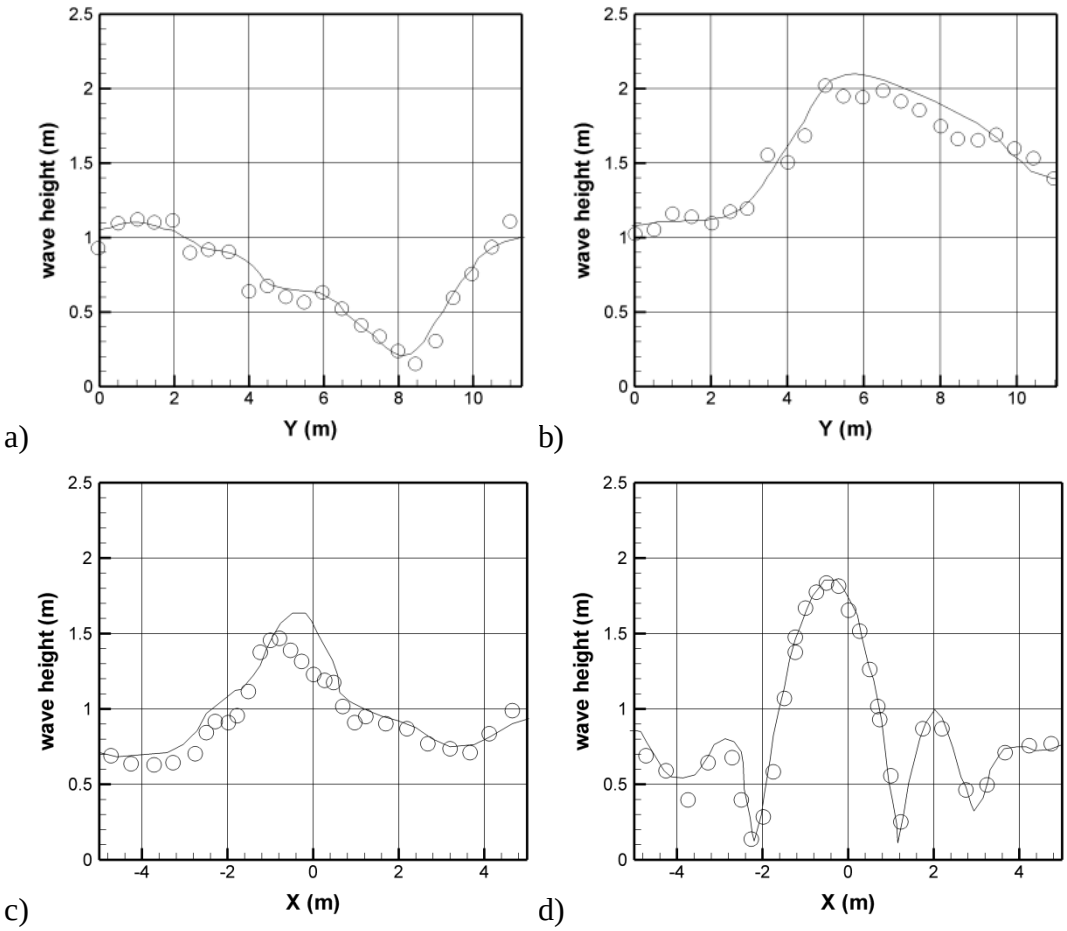

Figure 4. Wave deformation by an elliptic shoal. Comparison between numerical results (solid line) and experimental data (circles) of the wave heights along sections (a) $x = 2\,m$; (b) $x = 0\,m$; (c) $y = 3\,m$ and (d) $y = 9\,m$.

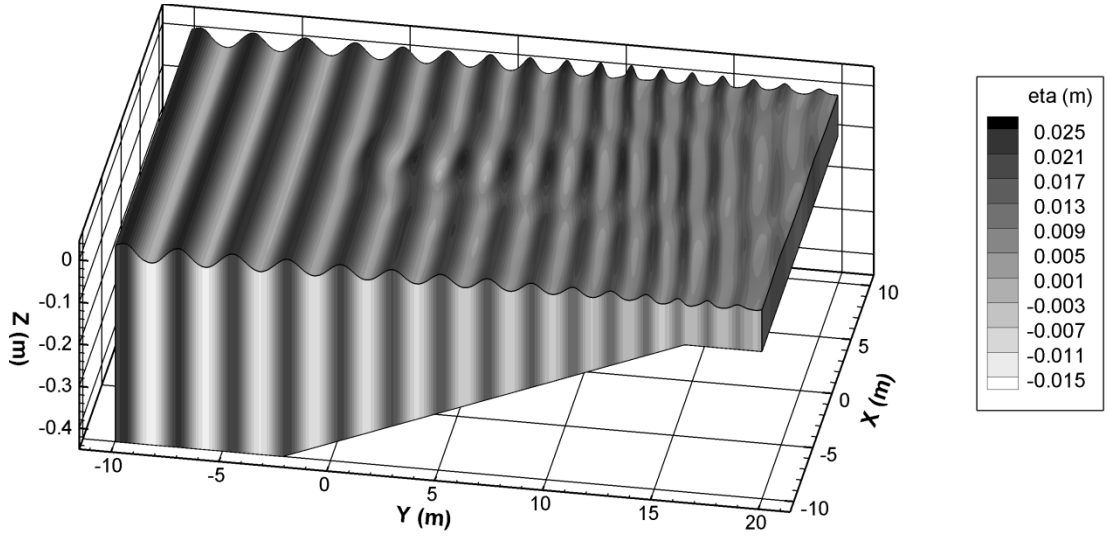

Figure 5. Wave deformation by an elliptic shoal. Three-dimensional instantaneous wave field.

2.5.3. Solitary wave on a slope beach (Synolakis 1987).

In this section the ability of the proposed hydrodynamic model to adequately represent a solitary wave in a channel with a slope beach is verified. The numerical results are compared with the experimental results obtained by Synolakis [1987]. The experimental test consists in the propagation of a solitary wave in a one-dimensional channel with a slope beach and it is for this able to verify the capacity of the numerical model to correctly represent the breaking, the runup and the wetting-drying phenomena. The numerical test is made by using a spatial discretization step of 0.05m and a time step of 0.005s. 475 horizontal calculus cell and only four vertical layer are used. The beach slope is 1/20 and the waves are generated on left boundary. The left boundary is 3m far from the toe of the beach. The still water depth is 0.29m while the wave amplitude is 0.0812m; the solitary wave is generated by using Equations (76-77) (sec 2.6.2).

In Figure 6 the comparison between numerical and experimental results of the free surface elevation is shown. The free surface elevation (normalized by still water dept *d*) obtained with the numerical model is compared with the free surface elevation at different time ((a)t = 5.93 s, (b) t = 8.89s, (c) t = 11.86s, (d) t = 14.82s, (e) t = 11.78s, (f) t = 29.64s).

From Figures 6.a-b it is possible to notice how the wave profile is modified by the bottom slope interaction: the wave front becomes steeper and the breaking starts (Figure 6.c), afterward the wave profile becomes strongly asymmetric and the wave height gradually decreases (Figure 6.d). From Figures (6.e-f) it is possible to see the maximum level of the runup and rundown. The numerical results are in good agreement with the experimental results.

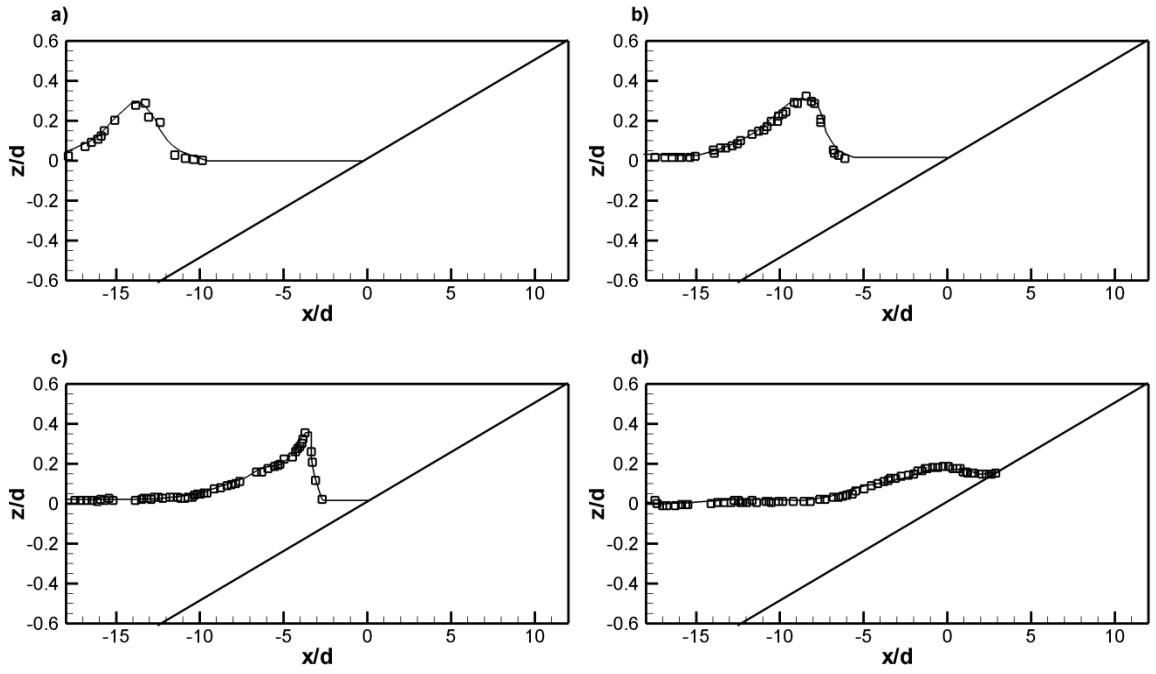

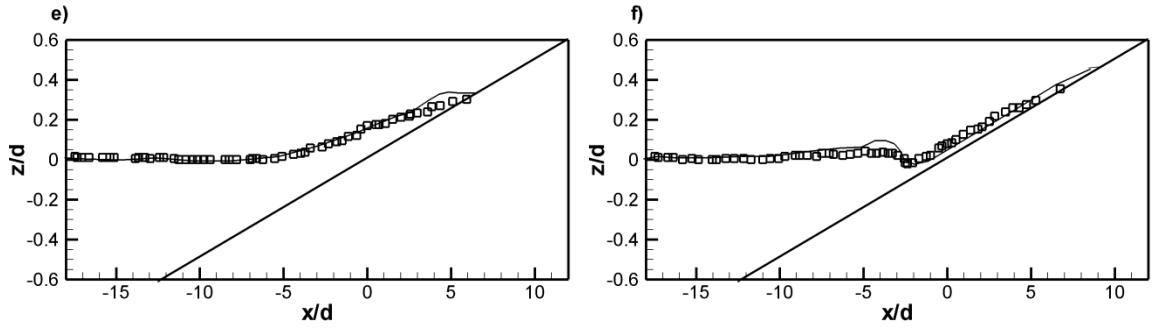

Figure 6. Solitary wave on a slope beach (Synolakis [1987]). Free surface elevation at different time step ((a)t = 5.93 s, (b) t = 8.89s, (c) t = 11.86s, (d) t = 14.82s, (e) t = 11.78s, (f) t = 29.64s). Comparison between numerical results (solid line) and experimental result (square).

2.5.4. Vortices formation dues to wave-structure interaction.

In this section the results related to the non-linear wave-submerged structure interaction simulation are shown. The computational domain is a rectangular channel of 5m length and the still water depth is 0.228m. In the middle of the rectangular channel a submerged rigid square obstacle is placed: the length of the vertical side of the square is 0.114m while the horizontal side of the square is 0.29m. The spatial discretization step is 0.0025m and 100 vertical layers are used. The time discretization step is 0.001s. The submerged obstacle is modeled by following the Lin [2006] strategy. A Smagorinsky sub grid sub scale model is used in order to evaluate the energy dissipation related to the wave structure interaction. The solitary wave is generated on left boundary by using Equations (76-77) (Sec 2.6.2), where A=0.05m and T=1.0s. In Figure 7-13 the velocity field and the free surface elevation related to the wave-structure interaction are shown at different time steps.

As is known, the interaction between the wave motion and the submerged obstacle can generate vortex structure (Lin [2006]). In Figure 7 the free surface elevation and the velocity field are shown when the solitary wave has not yet reached the obstacle and the velocity value is small. When the wave comes near the obstacle (Figure 8) the velocity value on the left side of the obstacle increases. Subsequently, (Figure 9) when the solitary wave has reached the left side of the obstacle, a little vortex on the left should of the obstacle is formed, while on the right side of the obstacle the velocity continue to increase. When the peak of the wave is on the left arris of the obstacle (Figure 10) the vortex on the same arris is completely developed. The vortex behind the right arris starts to form when the peak of the wave reaches the right arris of the obstacle (Figure 11), while the vortex on the left side is increasing his dimension. From Figure 12-13 it is possible to notice how the wave crossing strongly modifies the vortices structures. In particular, the left vortex becomes sheeted and longer, while the right vortex becomes strengthen.

At last, from Figures 14-15 it is possible to see how the vortex on the right side of the obstacle increases and persists for quite some time even when the solitary wave is now far, as shown in Lin [2006].

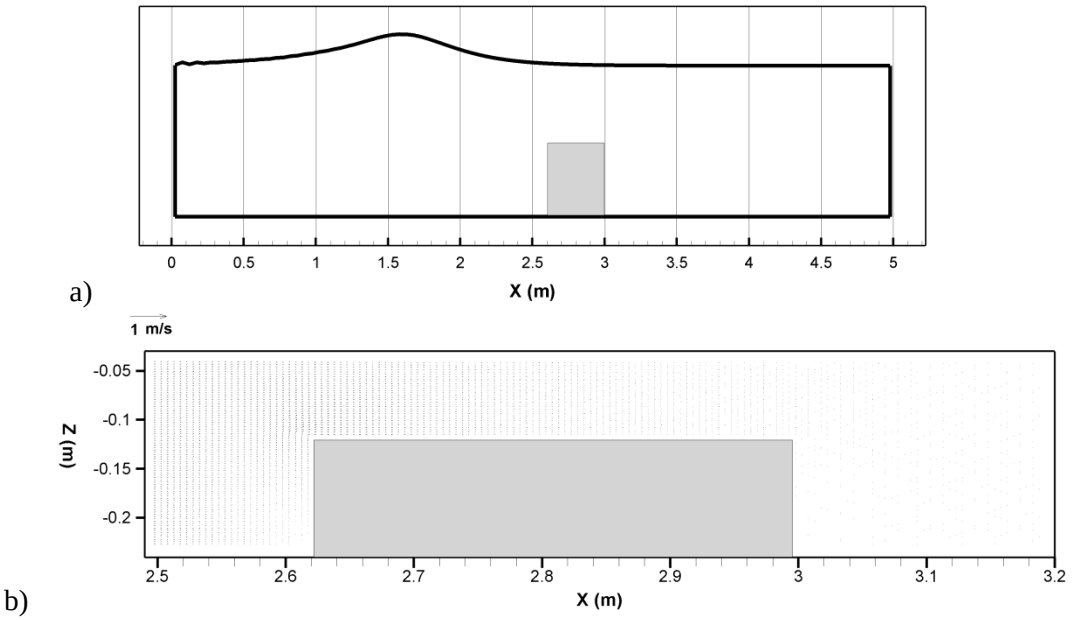

Figure 7. Vortices formation dues to wave-structure interaction. Free surface elevation (a) and velocity field (b) at time t=1.872 s $\left(t\sqrt{g/h} = 12.28\right)$.

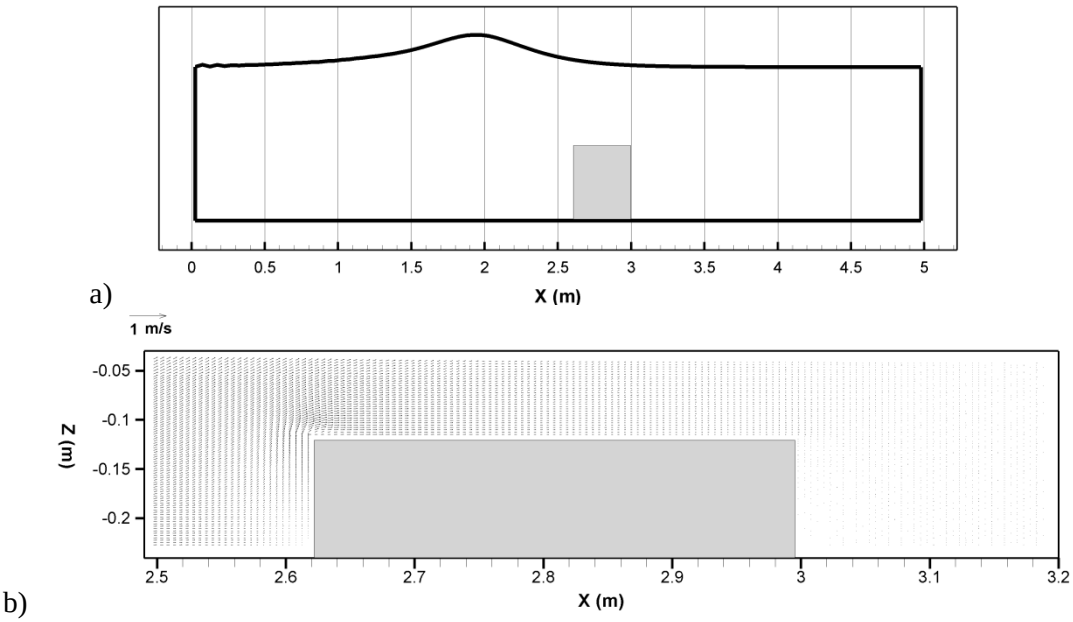

Figure 8. Vortices formation dues to wave-structure interaction. Free surface elevation (a) and velocity field (b) at time t=2.093s $\left(t\sqrt{g/h} = 13.73\right)$.

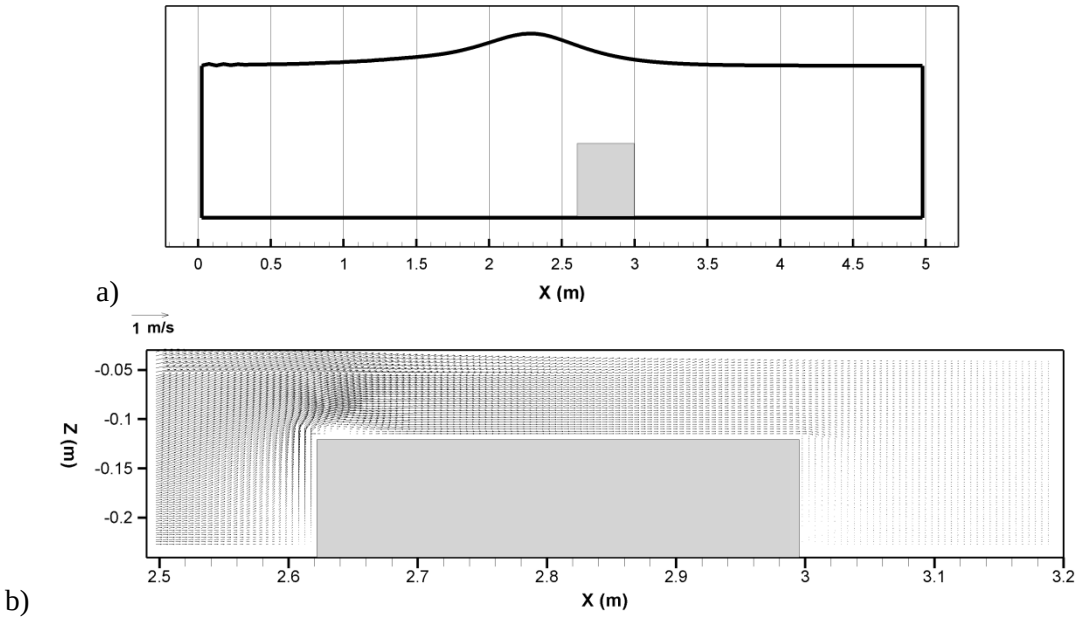

Figure 9. Vortices formation dues to wave-structure interaction. Free surface elevation (a) and velocity field (b) at time t=2.315s $\left(t\sqrt{g/h} = 15.19\right)$.

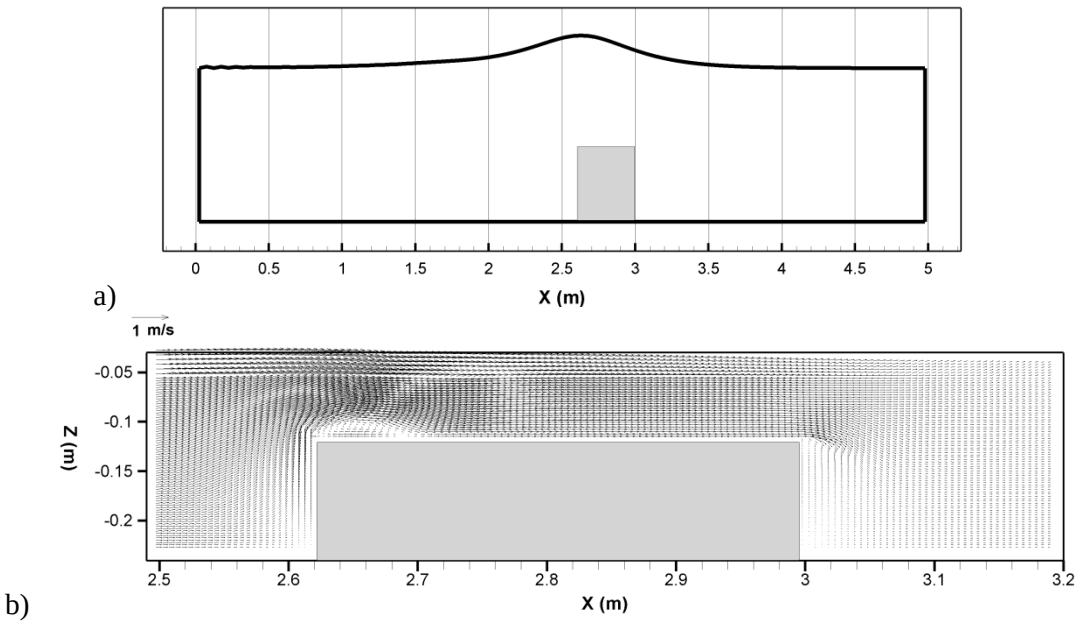

Figure 10. Vortices formation dues to wave-structure interaction. Free surface elevation (a) and velocity field (b) at time t=2.523s $\left(t\sqrt{g/h} = 16.55\right)$.

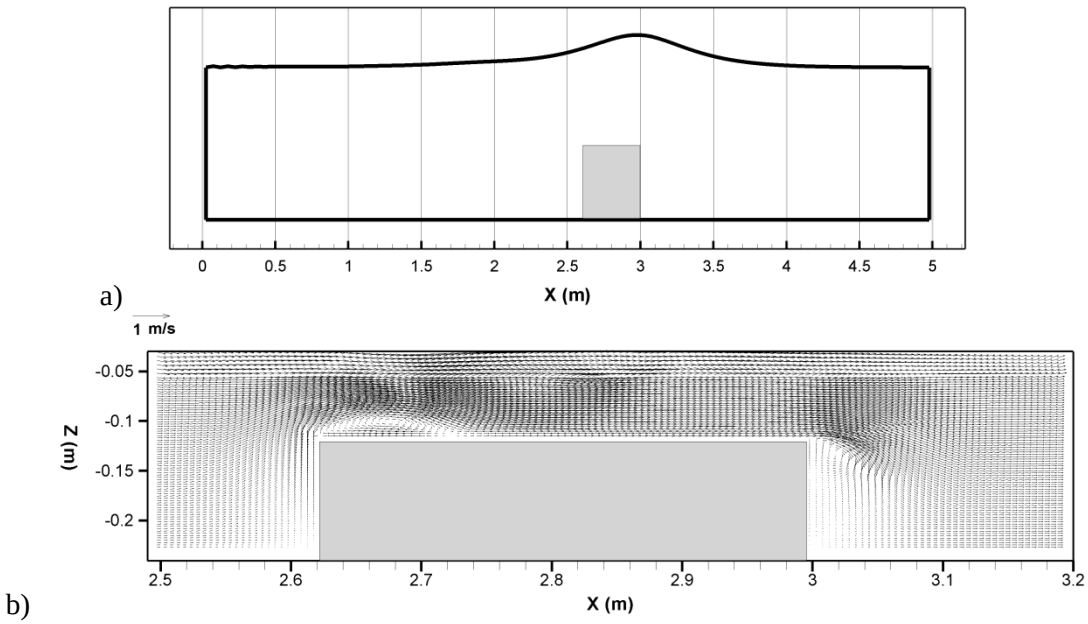

Figure 11. Vortices formation dues to wave-structure interaction. Free surface elevation (a) and velocity field (b) at time t=2.709s $\left(t\sqrt{g/h} = 17.77\right)$.

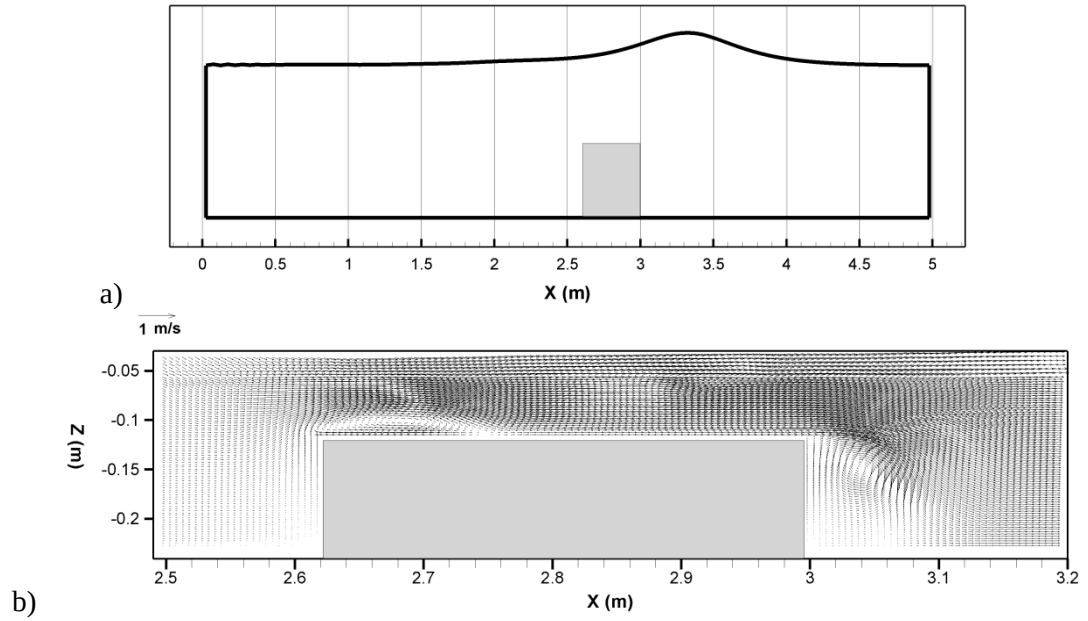

Figure 12. Vortices formation dues to wave-structure interaction. Free surface elevation (a) and velocity field (b) at time t=2.889s $\left(t\sqrt{g/h} = 18.95\right)$.

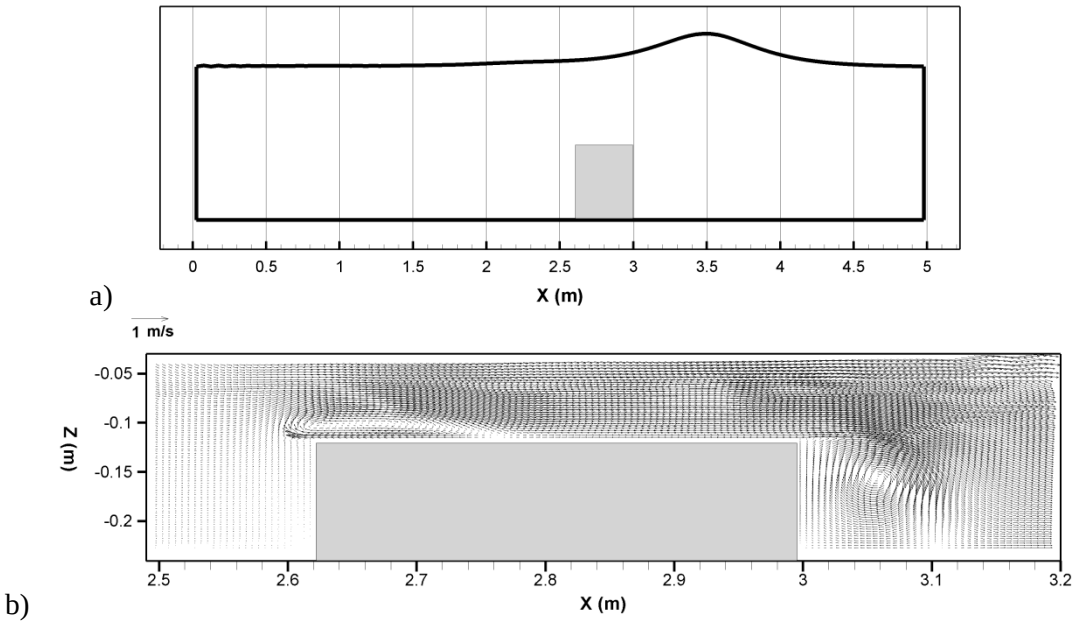

Figure 13. Vortices formation dues to wave-structure interaction. Free surface elevation (a) and velocity field (b) at time t=3.048s $\left(t\sqrt{g/h} = 19.99\right)$.

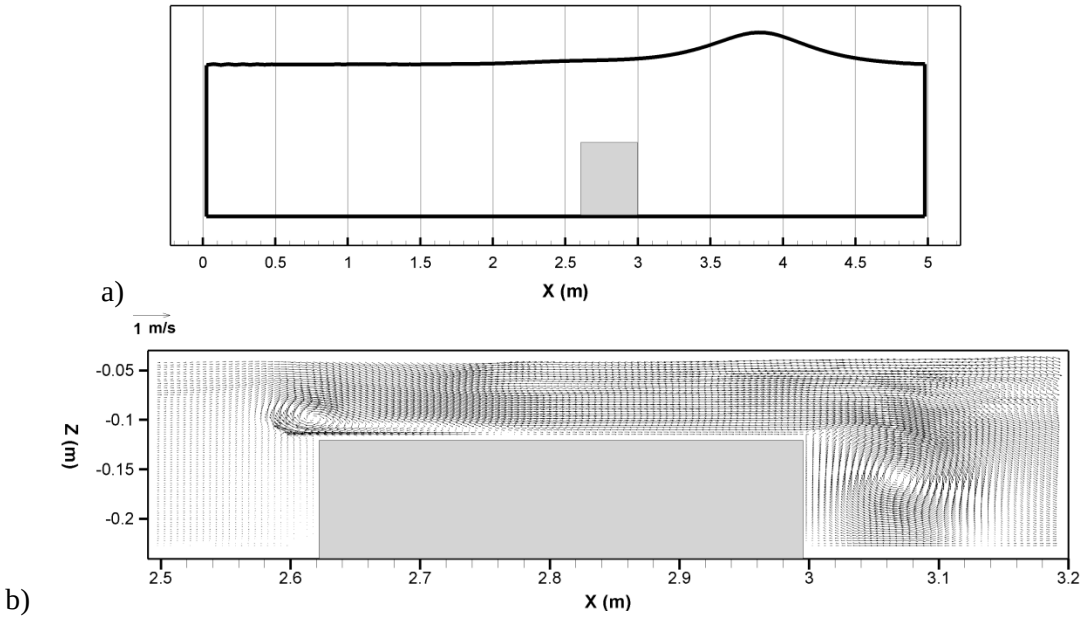

Figure 14. Vortices formation dues to wave-structure interaction. Free surface elevation (a) and velocity field (b) at time t=3.219s $\left(t\sqrt{g/h} = 21.11\right)$.

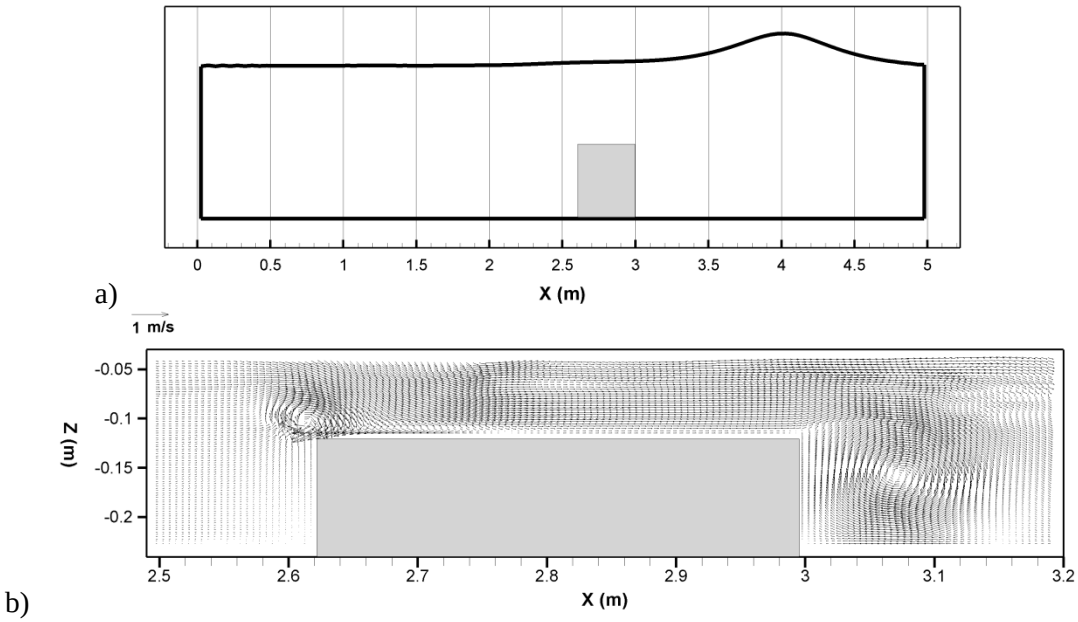

Figure 15. Vortices formation dues to wave-structure interaction. Free surface elevation (a) and velocity field (b) at time t=3.303s $\left(t\sqrt{g/h} = 21.77\right)$.

2.5.5. Three-dimensional simulation of flow-structure interaction.

In this section the results related to a three-dimensional flow-structure interaction test are shown. The test consists in simulating a uniform flow field in an open channel in which a rigid cube is situated on the channel bottom. Similar tests have been conducted by Li and Zhu [2002]. The channel is 3.5m wide and 5m length and the still water depth is 1m. The height of the cube is half of the depth flow and the boundaries of the domain are set at 1.5m and 3m respectively upstream and downstream the cube and 1.5m on both lateral side of the cube. Closed and reflective boundary condition are imposed on the lateral boundary of the channel and stillness initial condition are imposed. At the inflow an uniform and horizontal velocity field is imposed:

$$\begin{cases} u(1,j,k) = t/2\ ;\ t \le 1\ s\ , \\ u(1,j,k) = 0.5\ ;\ t > 1\ s\ , \end{cases} \quad (1 \le j \le Ny; 1 \le k \le Nz) \tag{37}$$

where *Ny* is the number of the calculation cells in the *j* direction, *Nz* is the number of the calculation cells in the *k* direction. The spatial discretization step is $\Delta x = \Delta y = 0.025$, the time discretization step is 0.001s and forty vertical layers are used for this test. A Smagorinsky sub grid sub scale model is used in order to evaluate the energy dissipation related to the flow-structure interaction.

In Figure 16-17-18 the velocity field at three different time steps is shown.

Figure 16 the hydrodynamic flow field after 5s is shown where unsteady condition are still in progress: from Figure 16.A it is possible to see how a small vortex is forming downstream the upper arris and in Figure 16.B two circulations with vertical axis are shown.

In Figure 17 the hydrodynamic flow field after 10s of simulation is shown: from Figure 17.A it can be noticed that the main vortex increases its size while from Figure 17.B the axes of the horizontal vortices move in the downstream direction.

The value of the velocity field becomes steady after 15s of simulation (Figure 18): the main vortex behind the obstacle is completely developed (Figure 18.A) and the vortices with the horizontal axes have completely change their attitude. The reattachment of the main vortex (Figure 18.A) is at 1.47h (where h is the size of the obstacle).

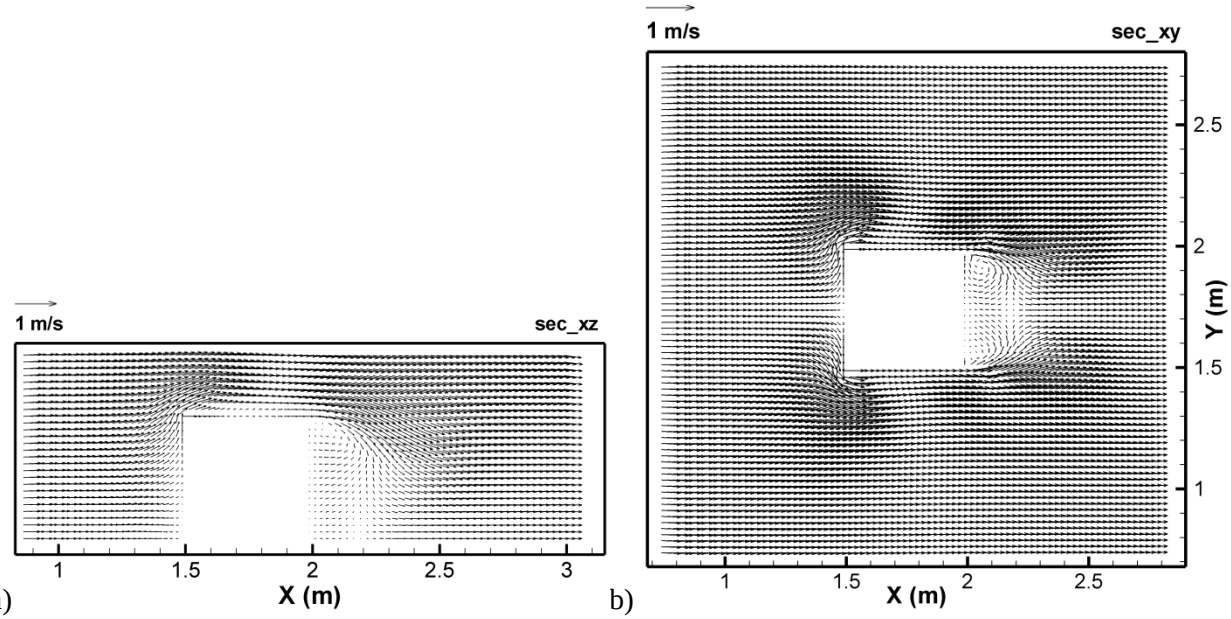

Figure 16. Three-dimensional simulation of flow-structure interaction. Velocity field at time t=5.0s A) Section Y=1.75m. B) Section Z=0.25m.

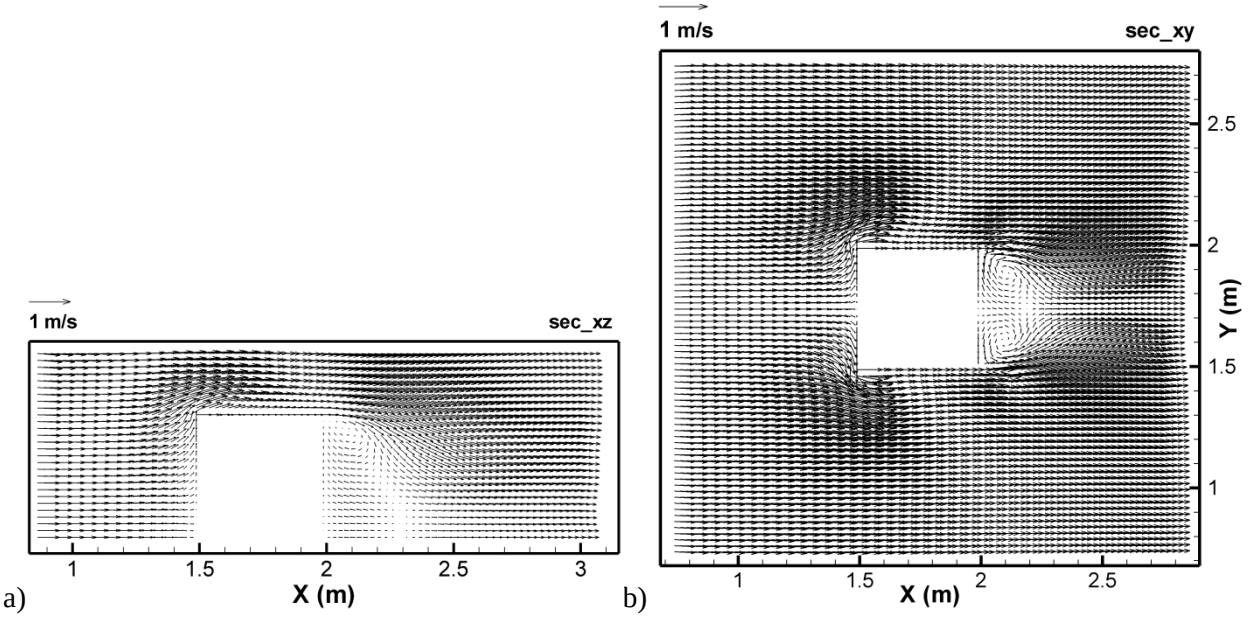

Figure 17. Three-dimensional simulation of flow-structure interaction. Velocity field at time t=10.0s A) Section Y=1.75m. B) Section Z=0.25m.

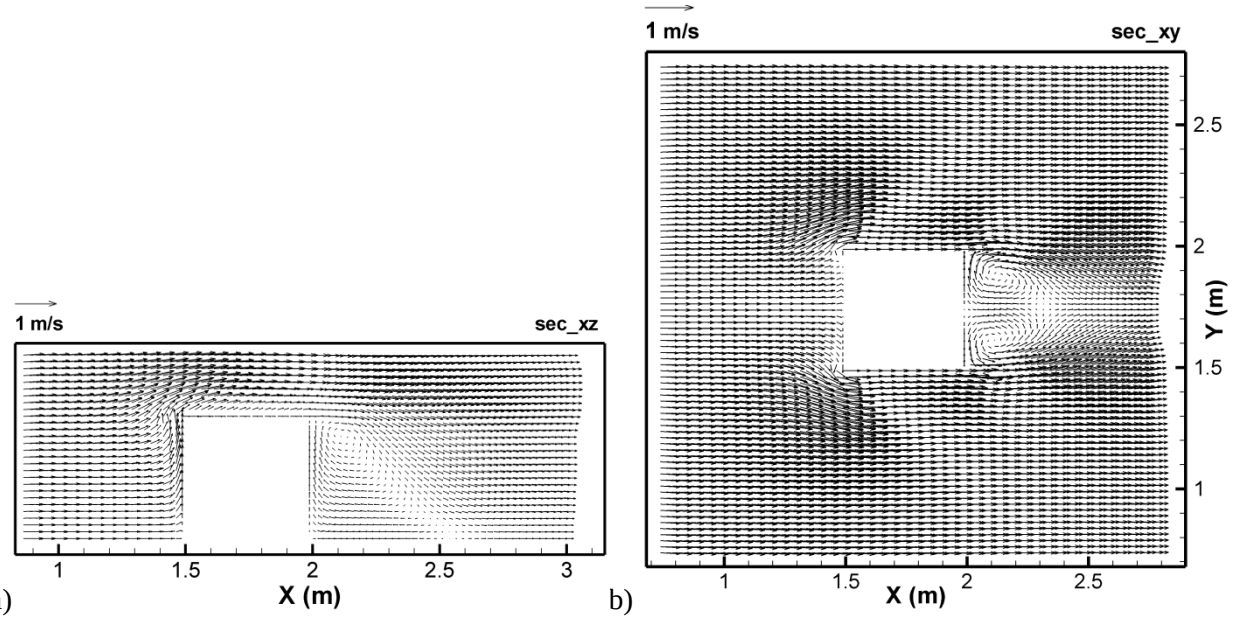

Figure 18. Three-dimensional simulation of flow-structure interaction. Velocity field at time t=15.0s A) Section Y=1.75m. B) Section Z=0.25m.

3. Conclusions

Two original model has been proposed in this thesis. The first one is based on an numerical integration of a new integral contravariant form of the Fully Non-linear Boussinesq Equations. The Boussinesq equation system is numerically solved by a hybrid finite volume-finite difference scheme; the conservative part of the equations is discretized by an original high-order upwind WENO shock-capturing finite volume scheme, based on an exact Riemann solver. The integral form of the continuity equation described in this thesis does not contain dispersive terms and is entirely discretized by the above-mentioned shock capturing finite volume scheme. In this way the errors due to the low order discretization of such dispersive term are not introduced into the solution. A procedure is developed in order to correct errors related to the difficulties of numerically satisfying the metric identities in the numerical integration of the FNBE on generalized boundary-conforming grids. The proposed high-order upwind WENO finite volume scheme is based on a genuinely two dimensional reconstruction procedure which uses a convex combination of biquadratic polynomials. Furthermore an original procedure for the treatment of the wet/dry front is presented. As previously demonstrated this model makes it possible to accurately simulate wave transformation phenomena, breaking longshore current, run up and wetting drying phenomena, the non-linear interaction between wave motion and submerged bar and strongly non linear and dispersive wave propagation on an highly distorted grid.

The second model is based on an original integral form of the Navier-Stokes Equations in a time-dependent coordinate system. The motion equations are discretized by means of a Finite Volume Shock-Capturing numerical procedure based on high order WENO reconstructions. The solution procedure for the motion equations uses a third order accurate Runge-Kutta fractional-step method and applies a pressure corrector formulation in order to obtain a divergence free velocity field at each stage. In the prediction phase of the fractional-step proposed model, the motion equations are discretized by means of a shock-capturing numerical procedure based on high order WENO reconstructions. The numerical flux is given at each cell interface by the solution of an approximate HLL Riemann problem. In the corrector phase of the fractional-step proposed model, in order to solve the Poisson equation and to reduce the computational costs related to it, an alternate Zebra four-colour Gauss-Siedel relaxation method with a V-cycle multigrid strategy is used. As previously demonstrated the new Finite-Volume Non-Hydrostatic and Shock-Capturing three-Dimensional Model is able to simulate wave refraction, diffraction, shoaling, breaking and wave-structure interaction.

4. References

1) Abbott MB. McCowan AD. Warren IR. Accuracy of short-wave numerical models. *Journal of Hydraulics Engineering* 1985; **110 (10)**:1287–1301.
2) Aris R. Vectors, tensors, and the basic equations of fluid mechanics. New York, NY, USA: Dover. 1989.
3) Beji S, Batties JA. Experimental investigation of wave propagation over a bar. *Coastal Eng* 1993; **19**: 151-162.
4) Berkhoff JCW, Booy N, Radder AC Verification of numerical wave propagation models for simple harmonic linear water waves. *Coastal Eng* 1982; **6**: 255-279.
5) Bradford SF. Gudonov-basded model for non-hydrostatic wave dynamics. *J of Waterway, Port, Coastal, and Ocean Engineering* 2005; **131**: 226-238.
6) Bradford SF, Nonhydrostatic model for surf zone simulation. *J of Waterway, Port, Coastal, and Ocean Engineering* 2011; **137(4)**: 163-174.
7) Briganti R, Dodd N, Kelly D, Pokrajac D, An efficient and flexible solver for the simulation of the morphodynamics of fast evolving flows on coarse sediment beaches. *Int J for Num Meth in Fluids* 2012; **69** : 859-877
8) Caleffi V, Valiani A, Bernini A. Fourth-order balanced source term treatment in central WENO schemes for shallow water equations. *Journal of Computational Physics* 2006; **218(1)**:245–282.
9) Caleffi V, Valiani A. Well-Balanced Bottom Discontinuities Treatment for High-Order Shallow Water Equations WENO Scheme. *Journal of Engineering Mechanics* 2009; **137(5)**: 684–696.
10) Casulli V, Cheng RT, Semi-implicit finite difference methods for three-dimensional shallow flow. *Int J for Num Meth in Fluids* 1992; **15** : 629-648.
11) Casulli V, Stelling GS Numerical simulation of 3D quasi-hydrostatic free-surface flows. *J Hydrol Eng* 1998; **124**: 678-686.
12) Chen Q, Kirby JT, Dalrympe RA, Shi F, Thornton EB. Boussinesq modeling of longshore currents. *J of Geophysical Research* 2003; **108(c11)**: 3362.
13) Chen Q, Fully Nonlinear Boussinesq-Type Equations for Waves and Currents over Porous Beds. *J of Engineering Mechanics* 2006; **132(2)**. 220-230.
14) Erduran KS, Illic S, Kutija V, Hybrid finite-volume finite-difference scheme for the solution of Boussinesq equations. *Int J for Num Meth in Fluids* 2005; **49(11)**: 1213-1232.
15) Furman DR, Madsen PA, Tsunami generation, propagation, and run-up with a high-order Boussinesq model. *Coastal Engineering* 2009; **56**: 747-758.
16) Gallerano F, Cannata G. Central WENO scheme for the integral form of contravariant shallow-water equations. *Int J for Num Meth in Fluids* 2011; **67(8)**: 939-959.
17) Gallerano F, Cannata G, Tamburrino M. Upwind WENO scheme for Shallow Water Equations in contravariant formulation. *Computers & Fluids* 2012; **62** : 1-12.
18) Gallerano F, Cannata G, Villani M, An integral contravariant formulation of the fully non-linear Boussinesq equations. *Coastal Engineering* 2014; **83** : 119-136.
19) Gottlieb S, Ketcheson DI, Shu CW. High order strong stability preserving time discretizations. *J Sci Comput* 2009: **38** : 251-289.

20) Haller MC. Experimental study of nearshore dynamics on a barred beach with rip channel. *J of Geophysical Research* 2002; **107(c6)** : 1-21.
21) Harlow FH, Welch JE. Numerical calculation of time dependent viscous incompressible flow. *Physics of fluids* 1965; **8**: 2182-2189.
22) Harten A, Lax P, Van Leer B. On upstream differencing and Godonov-type schemes for hyperbolic conservation laws. *SIAM Rev* 1983; 25-35
23) Jiang GS, Shu CW, Efficient Implementation of Weighted ENO Schemes. *J of Computational Physics* 1996; **126(1)**: 202-228.
24) Johns B, Jefferson J. The numerical modeling of surface wave propagation in the surf zone. *America Meteorological Society* 1980; **22** 1061-1069.
25) Karambas TV, Koutitas C. A breaking wave propagation model based on the Boussinesq equations.*Coastal Engineering* 1992; **18(1-2)**: 1-19.
26) Kennedy AB, Chen Q, Kirby JT, Dalrymple RA. Boussinesq modeling of wave transformation, breaking and runup. I: 1D. *J of Waterway, Port, Coastal, and Ocean Engineering* 2000; **126(1)**: 39-47.
27) Lai Z, Chen C, Cowles G, Beardsley RC. A non-hydrostatic version of FVCOM: 1. Validation experiment. *J of Geophysical Research* 2010; **115**: 1-23.
28) Levy D, Puppo G, Russo G. A Fourth-Order Central WENO Scheme for Multidimensional Hyperbolic Systems of Conservation Laws. *SIAM J Sci Comput* 2002; **24(2)** : 480-506.
29) Li CW, Zhu B. A σ-coordinate 3D k-ε model for turbulent free surface flow over a submerged structure. *Applied Mathematical modeling* 2002; **26** : 1139-1150.
30) Lin P, Li CW, A σ-coordinate three-dimensional numerical model for surface wave propagation *Int J for Num Meth in Fluids* 2002; **38** : 1045-1068.
31) Lin P. A multiple layer σ-coordinate model for simulation of wave-structure interaction. *Computer & Fluids* 2006 : **35** : 147-167.
32) Liu PLF. Cho YS Briggs MJ. Kanoglu U. Synolakis CE. Runup of solitary waves on a circular island. J Fluid Mech, 1995; 302 : 259-285.
33) Liu PLF. Yoon SB. Seo SN. Cho Y-S. *Numerical simulation of tsunami inundation at Hilo, Hawaii. Recent Development in Tsunami Research (ed. El-Sabh, M. I.).* Kluwer Academic Publishers: New York, 1994.
34) Luo H, Bewley TR. On the contravariant form of the Navier–Stokes equations in time-dependent curvilinear coordinate systems. *J of Computational Physics* 2004; **199(1)**: 355-375.
35) Ma G, Shi F, Kirby JT. Shock-capturing non-hydrostatic model for fully dispersive surface wave processes. *Ocean Modelling* 2012; **43-44** : 22-35.
36) Madsen PA, Sørensen OR. A new form of the Boussinesq equations with improved linear dispersion characteristics. Part 2. A slowly-varying bathymetry. *Coastal Engineering* 1992; **18(3-4)**: 183-204.
37) Nikolos IK, Delis AI. An unstructured node-centered finite volume scheme for shallow water flows with wet/dry fronts over complex topography. *Comput. Methods Appl. Mech. Engrg.* 2009; **198**: 3723-2750.
38) Nwogu O. Alternative Form of Boussinesq Equations for Nearshore Wave Propagation. *J of Waterway, Port, Coastal, and Ocean Engineering*1993; **119(6)**: 618-638.

39) Nonomura T, Iizuka N, Fujii K. Freestream and vortex preservation properties of high-order WENO and WCNS on curvilinear grids. *Computer & Fluids* 2010; **39(2)** : 197-214.
40) Peregrine DH, Long waves on a beach, *J of Fluid Mechanics* 1967; **27(4)** : 815-827.
41) Phillips NA, A coordinate system having some special advantages for numerical forecasting. *J Meteor* 1957; **14** : 184-185.
42) Rakha KA, Deigaard R, Brøker I. A phase-resolving cross shore sediment transport model for beach profile evolution. *Coastal Engineering* 1997; **31**: 231-261.
43) Roeber V, Cheung KF, Kobayashi MH. Shock-capturing Boussinesq-type model for nearshore wave processes. *Coastal Engineering* 2010; **57(4)**: 407-423.
44) Roeber V, Cheung KF. Boussinesq-type model for energetic breaking waves in fringing reef environments. *Coastal Engineering* 2012; **70** : 1-20.
45) Rosenfeld M, Kwak D, Vinokur M, A fractional steo solution method for the unsteady incompressible Navier-Stokes Equations in generalized coordinate systems. *J of Computational Physics* 1991; **94** : 102-137.
46) Rossmanith JA, Bale DS, Le Veque RJ, A wave propagation algorithm for hyperbolic systems on curved manifolds. *J of Computational Physics* 2004; **199(2)** : 631-662.
47) Segal A, Wesseling P, Van Kan J, Oosterlee CW, Kassels K. Invariant discretization of the incompressible Navier-Stokes equations in boundary fitted co-ordinates. *Int J for Num Meth in Fluids* 1992; **15(4)**: 411-426.
48) Shi F, Kirby JT, Harris JC, Geiman JD, Grilli ST. A high-order adaptive time-stepping TVD solver for Boussinesq modeling of breaking waves and coastal inundation. *Coastal Engineering* 2012; **43-44** : 36-51.
49) Spiteri RJ, Ruuth SJ, A new class of optimal high-order strong-stability- preserving time discretization methods. *SIAM J Numer Anal* 2002; **40(2)** : 469-491.
50) Stelling G, Zijlema M. An accurate and efficient finite-difference algorithm for non-hydrostatic free-surface flow with application to wave propagation. *Int J for Num Meth in Fluids* 2003; **43** : 1-23.
51) Stoker JJ, *Water Waves*. New York: Interscience, 1957.
52) Svendsen IA, Yu K, Veeramony. A Boussinesq breaking wave model with vorticity. *Proc., 25th Int. Conf. Coastal Engrg. ASCE,* New York; 1996: 1192–1204.
53) Stive MJF. Velocity and pressure field of spilling breakers. Proc. 17th Int. Conf. *Coastal Engineering* 1980; **1** : 547-566.
54) Synolakis CE. The Runup of solitary waves. *J Fluid Mech.* 1987; **185** : 523-545.
55) Thomas TG, Leslie DC. Development of a conservative 3D free surface code. *Journal of Hydraulics Research.* 1992; **30**: 107-115.
56) Tonelli M, Petti M. Hybrid finite volume – finite difference scheme for 2DH improved Boussinesq equations. *Coastal Engineering* 2009; **56** : 609-620.
57) Tonelli M, Petti M. Shock-capturing Boussinesq model for irregular wave propagation. *Coastal Engineering* 2012; **61** : 8-19.
58) Toro E, *Shock-Capturing Methods for Free-Surface Shallow Flows.* John Wiley and Sons, Manchester. 2001.
59) Trottemberg U, Oosterlee CW, Schuller A, *Multigrid.* Academic press, 2001.

60) Vázquez-Cendón ME. Improved treatment of source terms in upwind schemes for the shallow water equations in channels with irregular geometry. *Journal of Computational Physics* 1999; **148(2)**:497–526.
61) Vinokur M. An analysis of finite-difference and finite-volume formulations of conservation laws. *J of Computational Physics* 1989; **81(1)** : 1-52.
62) Visbal MR, Gaitonde DV. On the Use of Higher-Order Finite-Difference Schemes on Curvilinear and Deforming Meshes. *J of Computational Physics* 2002; **181(1)**: 155-185.
63) Visser PJ. Laboratory measuraments of uniform longshore currents. *Coastal Engineering* 1991; **15(5-6)** : 563-593.
64) Warsi ZUA, *Fluid Dynamics Theoretical and Computational Approaches*. Dep of Aerospace Engineering Mississippi State university. CRC Press. 1992.
65) Watts P, Grilli ST, Kirby JT, Fryer GJ, Tappin DR. Landslide tsunami case studies using a Boussinesq model and a fully nonlinear tsunami generation model. Natural Hazards and Earth System Science. *Copernicus Publications on behalf of the European Geosciences Union* 2003; **3(5)** : 391-402.
66) Wei G, Kirby JT. Time-Dependent Numerical Code for Extended Boussinesq Equations. *J of Waterway, Port, Coastal, and Ocean Engineering* 1995; **121(5)**: 251-261.
67) Wei G, Kirby JT, Grilli ST, Subramanya R. A fully non-linear Boussinesq model for surface waves. Part 1. Highly non-linear un steady waves. *J Fluid Mech* 1995; **294** : 71-92.
68) Wei G, Kirby JT, Sinha A. Generation of waves in Boussinesq models using a source function method. *Coastal Engineering* 1999; **36** : 271-299.
69) Wesseling P, Segal A, Kassels GM. Computing Flows on General Three-Dimensional Nonsmooth Staggered Grids. *J of Computational Physics* 1999; **149(2)**: 333-362.
70) Xing Y, Shu CW, High order well-balanced finite volume WENO schemes and discontinuous Galerkin methods for a class of hyperbolic systems with source terms. *J of Computational Physics* 2006; **214(2)** : 567-598.
71) Xing Y, Shu CW. High-order finite volume WENO schemes for the shallow water equations with dry states. *Advances in Water Resources* 2011; **34(8)** : 1026-1038.
72) Yang HQ, Habchi SD, Przekwas AJ. General strong conservation formulation of Navier–Stokes equations in non-orthogonal curvilinear coordinates. *AIAA J* 1994; **32(5)** : 936-941.
73) Zhou JG, Causon DM, Mingham CG, Ingram DM. The surface gradient method for the treatment of source terms in the shallow water equations. *Journal of Computational Physics*2001;**168(1)**: 1–25.
74) Zijlema M, Segal A, Wesseling P. Invariant discretization of the *k*-ϵ model in general co-ordinates for prediction of turbulent flow in complicated geometries. *Computers & Fluids*1995; **24(3)**: 209-225.